ANALYSIS OF SURFACE WATER DYNAMICS ALONG THE TANANA RIVER, AK USING IN SITU OBSERVATIONS, AIRSWOT MEASUREMENTS, AND HYDRODYNAMIC MODELING

Elizabeth Humphries Altenau

A dissertation submitted to the faculty of the University of North Carolina at Chapel Hill in partial fulfillment of the requirements for the degree of Doctor of Philosophy in the Department of Geological Sciences.

Chapel Hill
2018

Approved by:

Tamlin M. Pavelsky

Paul D. Bates

Jonathan M. Lees

Benjamin B. Mirus

Laura J. Moore

ABSTRACT

Elizabeth Humphries Altenau: Analysis of surface water dynamics along the Tanana River, AK using in situ observations, AirSWOT measurements, and hydrodynamic modeling
(Under the direction of Tamlin M. Pavelsky)

Fluctuations in water surface elevations (WSEs) along rivers have important implications for water resources, flood hazards, and biogeochemical cycling. However, current hydrodynamic modeling and remote sensing methods exhibit key limitations in characterizing spatiotemporal hydraulics in many of the world's river systems, particularly multichannel rivers. This dissertation investigates the capabilities of state of the art hydrodynamic models and new remote sensing observations to characterize surface water dynamics across a large-scale, anabranching river. In Chapter 1, I build and compare six different hydrodynamic models along the Tanana River, AK to investigate (1) how well a simple, raster-based model can simulate 2D channel hydraulics, and (2) how degrading the physical representation of a multichannel river system affects spatial and temporal errors in model outputs. I show that simple, raster-based models can accurately simulate 2D, in-channel hydraulics in a complex multichannel river, and that inclusion of the anabranching network is essential for simulating proper hydraulics at regional-scales. In Chapter 2, I validate new radar measurements of WSE and slope from AirSWOT, an airborne analogue to the Surface Water and Ocean Topography (SWOT) mission. I find that AirSWOT accuracies are at least as good as what we expect from SWOT, and in some cases, substantially better, with RMSEs of 9.0 cm for river WSEs when averaged over 1 km^2 areas, and 1.0 cm/km for slopes along 10 km reaches. In Chapter 3, I investigate AirSWOT's ability to capture multi-temporal fluctuations in WSE and slope. I demonstrate that AirSWOT can provide a

comprehensive picture of river dynamics by observing decimeter-level WSE changes when averaged over 1 km^2 areas and centimeter-per-kilometer-level slope changes for reaches ≥5 km with RMSEs of 10.4 cm, and 1.0 cm/km respectively. Additionally, AirSWOT measurements add marginal differences when estimating discharge with an RMSE of 15.3% compared to *in situ* discharge estimates and 42% of AirSWOT discharge estimates falling within the *in situ* discharge uncertainty. In the future, AirSWOT measurements can be used to study detailed passages of flood waves, understand how features of riverbeds and banks affect patterns of flow, and integrate into local and regional-scale hydrodynamic models to improve flood predictions.

to Dan
for his remarkable love and patience

to my parents
for their incredible support and reassurance

and to my pup, Humphrey
for his endless joy

ACKNOWLEDGEMENTS

I thank my advisor Dr. Tamlin Pavelsky for his encouragement and unwavering support throughout my PhD. This work would not have been possible without his fantastic, enthusiastic guidance. I thank my dissertation committee members Dr. Paul Bates, Dr. Jonathan Lees, Dr. Benjamin Mirus, and Dr. Laura Moore for their advice on my research and the revision of this work. Additionally, the work presented here benefited greatly from field work and collaborations with my coauthors Dr. George Allen, Dr. Paul Bates, Dr. Stéphane Calmant, Dr. Michael Durand, Dr. Christine Lion, Dr. Delwyn Moller, Dr. Jeffrey Neal, Lincoln Pitcher, and Dr. Laurence Smith, as well as many other colleagues from the Department of Geological Sciences at University of North Carolina at Chapel Hill. I thank Curtis Chen, Craig Stringham, Albert Chen, Xiaaoqing Wu, Gregory Sadowy, and the JPL and AFRC AirSWOT teams for collection and processing of the AirSWOT data, as well as John Arvesen from Cirrus Digital Systems for processing the CIR imagery. Additionally, I thank our boat driver Sam Demientieff for his navigational expertise on the Tanana River, which allowed for safe and timely data collection. This work was funded by NASA Terrestrial Hydrology Program grant #NNX13AD05G, the UNC Geological Sciences Martin Research Endowment, and the UNC Dissertation Completion Fellowship. Field locations and observations of water surface elevation were based on equipment services provided by the UNAVCO Facility with support from the National Science Foundation (NSF) and National Aeronautics and Space Administration (NASA) under NSF Cooperative Agreement EAR-0735156. I thank my parents and grandparents, for their constant care and

support throughout my educational journey. Last but not least, I thank my husband Dan who pushed me to take on this challenge and gave me strength along the way.

TABLE OF CONTENTS

LIST OF TABLES

LIST OF FIGURES

CHAPTER 1: THE EFFECTS OF SPATIAL RESOLUTION AND DIMENSIONALITY ON MODELING REGIONAL-SCALE HYDRAULICS IN A MULTICHANNEL RIVER[1]

1.1. Introduction

Hydrodynamic modeling is a useful tool for predicting the spatially distributed water surface elevations (WSEs) needed for estimating flood magnitude, extent, and timing, especially in areas where field data are sparse and river morphologies are complex [*Bates and De Roo*, 2000; *Horritt and Bates*, 2001; *Hunter et al.*, 2007; *Beighley et al.*, 2009; *Bates et al.*, 2010; *Neal et al.*, 2012a, 2012b; *Nguyen et al.*, 2015]. Research over the past few decades has shown that models with simplified approximations of flow perform well and produce accurate estimates of WSE and inundation extent compared to more complex solutions of the full shallow water equations [*Bates and De Roo*, 2000; *Bradbrook et al.*, 2004; *Neal et al.*, 2012b; *de Almeida and Bates*, 2013]. Additionally, advances in remote sensing observations of key hydraulic variables have allowed substantial developments in implementing hydrodynamic models at regional to global scales [*Paiva et al.*, 2011, 2013; *Yamazaki et al.*, 2011; *Sampson et al.*, 2015, *Schumann et al.,* 2016]. Despite recent progress, the need to balance spatiotemporal resolution, computational efficiency, and data availability limits regional-scale flood models spanning river lengths ≥100 km to using downscaling techniques, subgrid representations, and 1D routing schemes to simulate channel flows [*Cloke and Pappenberger*, 2009; *Bierkens et al.*, 2015; *Sampson et al.*,

[1] This chapter previously appeared as an article in Water Resources Research. The original citation is as follows: Altenau, E. H., Pavelsky, T. M., Bates, P. D., Neal, J. C. (2017). The effects of spatial resolution and dimensionality on modeling regional-scale hydraulics in a multichannel river. *Water Resources Research*, 53(2), doi:10.1002/2016WR019396.

2015]. This requisite level of simplicity may limit the accuracy of model outputs, especially in rivers that are not well represented in 1D, such as multichannel systems. Such environments are quite common. *Allen and Pavelsky*, [2015] observe that for the North American continent multichannel river systems make up approximately 26% of Landsat-observable rivers above 60 degrees north, and *Latrubesse et al.* [2008] demonstrate that many of the world's largest river systems display anabranching morphologies.

To date, the most common approaches to regional-scale hydrodynamic modeling have not been rigorously tested in multichannel systems due to these rivers' challenging dynamics. There is extensive research using detailed 2D and 3D models at scales of 1-30 km to simulate the hydraulics and morphodynamics of multichannel rivers [*Bridge*, 1993; *Lane and Richards*, 1998; *Lane et al.*, 1999; *Nicholas and Sambrook Smith*, 1999; *Nicholas et al.*, 2012; *Williams et al.*, 2013; *Ziliani et al.*, 2013]. However, practical application of these models across hundreds of kilometers, much less globally, is computationally infeasible due to the need for fine grid scales and full solutions to the Saint Venant or Navier-Stokes equations [*Bates et al.*, 2005]. Decision-makers need efficient models of multichannel rivers at regional scales in order to predict flood patterns, which threaten people and valuable infrastructure within these highly complex river environments.

An important question that arises is one of appropriate complexity: How simple can we make a regional-scale model of a multichannel system and still produce useful information for science or management? Simpler model formulations reduce computational burden, increase viable domain sizes, and improve the feasibility of ensemble modeling. Previous research has explored the effects of spatial resolution and model dimensionality independent of one another on both single-thread and multichannel rivers [*Lane et al.*, 1999; *Horritt and Bates*, 2001, 2002;

Horritt et al., 2006; *Nicholas et al.*, 2012; *Schubert et al.*, 2015; *Javernick et al.*, 2016]. To the best of our knowledge, however, no previous work has explored the effects of both model resolution and dimensionality on a multichannel river at the scale of ~100 km or more. Fortunately, advances in algorithms, data availability, and computational resources now allow us to address this question, as we can build fine-resolution (≤ 25 m) models of 100 km+ reaches that can resolve all river channels explicitly [*Schubert et al.*, 2015]. These fine-resolution models can act as benchmarks against which we assess how simplifications to the bifurcating and converging channel network affect modeling flood wave propagation, water level, and inundation extent in multichannel systems at regional to global scales.

In order to address these questions, we compare six different LISFLOOD-FP models along a ~90 km, multichannel reach of the Tanana River, Alaska. For the first time in a highly complex, anabranching river, we test how well a simple, raster-based model can simulate 2D channel flows by assessing temporal and spatial outputs of WSE and inundation extent at the ~100 km reach scale. We then compare the 2D models to several models of lower dimensionality and coarser resolution. Simulations range from a 10 m resolution, 2D model that fully captures the river's complexity to a 500 m resolution 1D model that substantially simplifies the overall river structure. We focus on addressing (1) how well a simple, raster-based model can simulate 2D channel hydraulics, and (2) how degrading the physical representation of a multichannel river system affects spatial and temporal errors in model outputs.

1.2. Hydrodynamic Model

For this study we use the raster-based, hydrodynamic model LISFLOOD-FP [*Bates and De Roo,* 2000; *Bates et al.,* 2010; *de Almedia et al.,* 2012, *Neal et al.,* 2012a]. LISFLOOD-FP uses an explicit finite difference scheme to simulate shallow water waves over a

staggered grid using a local inertial approximation of the 1D Saint-Venant or shallow water equations [*Cunge et al.,* 1980]:

$$\frac{\partial A}{\partial t} + \frac{\partial Q}{\partial x} = 0, \tag{1.1}$$

$$\underbrace{\frac{\partial Q}{\partial t}}_{\text{acceleration}} + \underbrace{\frac{\partial}{\partial x}\left(\frac{Q^2}{A}\right)}_{\text{advection}} + \underbrace{\frac{gA\partial(h+z)}{\partial x}}_{\text{water slope}} + \underbrace{\frac{gn^2Q^2}{R^{\frac{4}{3}}A}}_{\text{friction slope}} = 0, \tag{1.2}$$

where equation 1.1 describes the continuity of mass and equation 1.2 the continuity of momentum such that Q[L^3T^{-1}] is the discharge, A[L^2] is the flow cross section, g[LT^{-2}] is the acceleration due to gravity, R[L] is the hydraulic radius, h[L] is the water depth, z[L] is the bed elevation, n[$TL^{-1/3}$] is the Manning friction coefficient, x[L] is the longitudinal coordinate, and t[T] is the time. The local inertial formulation incorporates the friction slope, water slope and local acceleration terms from the momentum equation of the shallow water equations above but neglects advection because bed friction tends to dominate over advective processes for large length scales [*Hunter et al.*, 2007]. Inclusion of local acceleration allows for faster computations with increased stability compared to simpler diffusive wave models [*Bates et al.*, 2010; *de Almeida et al.*, 2012; *Neal et al.*, 2012a].

For model resolutions ≤100 m we represent the channel bathymetry directly in the model grid and compute the time evolution of flow over this complex surface in 2D (Figure 1.1a,d). This study tests LISFLOOD-FP's ability to simulate 2D channel flows in a multichannel river environment for the first time. To do so, LISFLOOD-FP simultaneously solves the continuity of mass and momentum equations. The continuity equation for a raster cell over a time step Δt is:

$$h_{i,j}^{t+\Delta t} = h_{i,j} + \Delta t \frac{Q_{x\,i-1/2,j}^{t+\Delta t} - Q_{x\,i-1/2,j}^{t+\Delta t} + Q_{y\,i-1/2,j}^{t+\Delta t} - Q_{y\,i-1/2,j}^{t+\Delta t}}{A_{i,j}}, \tag{1.3}$$

where Q is the flow between cells, h is the cell water depth, A is the cell area, and the subscripts i and j are cell indices in the x and y directions [*Neal et al.*, 2012a]. For the momentum equation, flows in the x and y directions are decoupled and solved using the same calculation. The momentum equation for flow Q between raster cells in the x direction is:

$$Q_{i+1/2}^{t+\Delta t} = \frac{q_{i+1/2}^{t} - gh_{flow}^{t}\Delta t S_{i+1/2}^{t}}{\left[1 + g\Delta t n^2 \left|q_{i+1/2}^{t}\right| / (h_{flow}^{t})^{7/3}\right]} \Delta x, \tag{1.4}$$

where Δx is the cell width, g is acceleration due to gravity, q^t is flow from the previous time step Q^t divided by cell width Δx, S is water slope between cells, n is the Manning friction coefficient, and h_{flow} is the depth between cells which water can flow [*Neal et al.*, 2012a]. To maintain stability, the model uses a time-stepping equation based on the Courant-Friedrichs-Lewy condition [*Courant et al.,* 1928] and is limited to:

$$\Delta t = \alpha \frac{x}{\sqrt{\max(h^t)\, g}}, \tag{1.5}$$

where $\max(h^t)$ is the maximum water depth in the model domain and α is a stability coefficient that ranges from 0.2 to 0.7 for most floodplains. As the grid size decreases, the time step scales with 1/Δx [*Bates et al.,* 2010; *Neal et al.*, 2012a].

As the model spatial resolutions increase to ≥100 m, the grid scale imposes an increasingly severe restriction on the simulation of channelized flows, and we therefore treat channels as subgrid-scale features using the approach of *Neal et al.* [2012a]. Here, flow in channels narrower than the grid resolution are simulated using a 1D interpretation of the same local inertial formulation used for the 2D scheme with two additional variables that represent the channel bed elevations (z_c) and channel widths (w) (Figure 1.1b,c,e) [*Neal et al.*, 2012a; *Schumann et al.*, 2014a; *Sampson et al.*, 2015]. This approach is adopted because an explicit

representation of channels is known to be important for connectivity and water partitioning in floodplain dynamics [*Neal et al.*, 2012a; *Sampson et al.*, 2015].

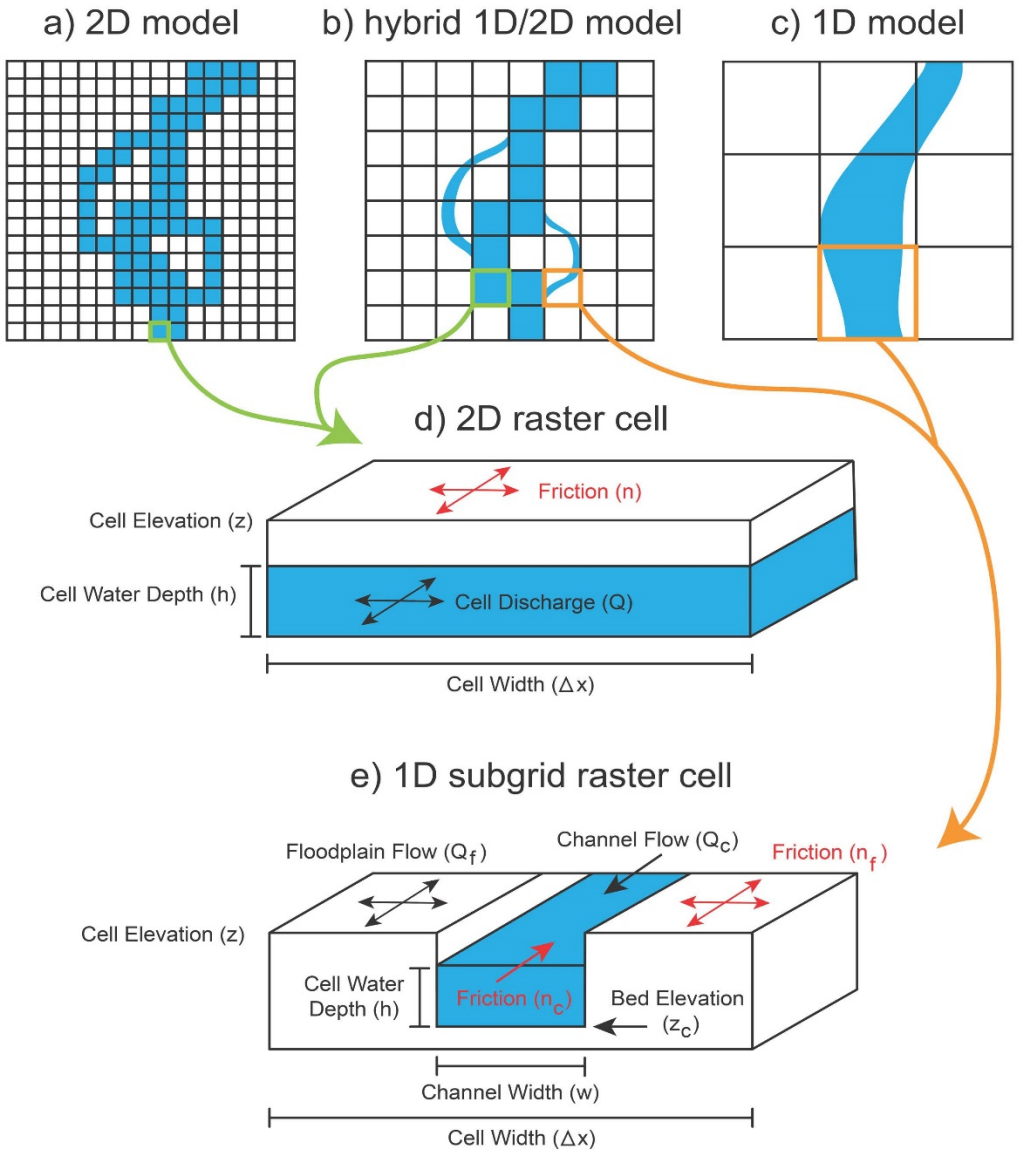

Figure 1.1: Conceptual schematic of (a) 2D channel flow model, (b) hybrid 1D/2D channel flow model, (c) 1D channel flow model, (d) 2D raster cell with relevant variables, and (e) 1D subgrid raster cell with relevant variables.

The primary inputs for the models are floodplain topography, bathymetry, roughness parameters, discharge, and stage information. LISFLOOD-FP is suitable for gradually-varied flow and can become unstable at low Manning's n values (less than 0.01) or under supercritical

flow conditions [*Bates et al.*, 2010; *Neal et al.*, 2012b; *de Almeida and Bates*, 2013], however, these conditions do not arise in our study reach for the model resolutions that we use. We chose LISFLOOD-FP as an appropriate model for this study because it is computationally efficient, can simulate flows in multiple dimensions, and is widely used within the hydrodynamic modeling community.

1.3. Study Site

We chose a ~90 km reach of the Tanana River in Alaska between the towns of Fairbanks and Nenana to assess the effects of model resolution and dimensionality on multichannel river hydraulics (Figure 1.2). The Tanana drains a large swath of the eastern Alaska Range and central Alaskan highlands, flowing northwest until it joins with the Yukon River. The shape of the annual hydrograph is largely determined by melt of snowpack and glaciers during the spring and summer. Low flows in the winter lead to a rapid increase of flow during the springtime and peak flows during the summer. Mean discharge during the open water season (May to October) for the Tanana is ~1299 m^3/s according to records from the USGS station at Nenana (Station Number: 15515500) from 1962 to 2013. Field calculations and modeling performed by *Toniolo et al.*, [2010], indicate flows along the Tanana are gradually varied and subcritical with an average Froude number of 0.30 along the Thalweg and are therefore suitable for modeling with LISFLOOD-FP.

The Tanana's glacial origin results in a high sediment load, which interacts with local topography to produce a complex morphology that ranges from highly braided to a single meandering channel. The suspended sediment load in the Tanana is extremely high (an estimated 33 metric tons per year) and consists primarily of silt and clay. For comparison, the farthest downstream station on the Yukon River recorded an estimated 68 metric tons of suspended

sediment per year with a mean annual discharge of ~6428 m^3/s [*Brabets et al.*, 2000; *Dornblaser and Striegl*, 2009]. The bed of the Tanana, composed of sand and gravel, is quite mobile, which results in comparatively rapid changes in channel planform. Physiographic characteristics of the region include alluvial deposits and discontinuous permafrost [*Brabets et al.*, 2000].

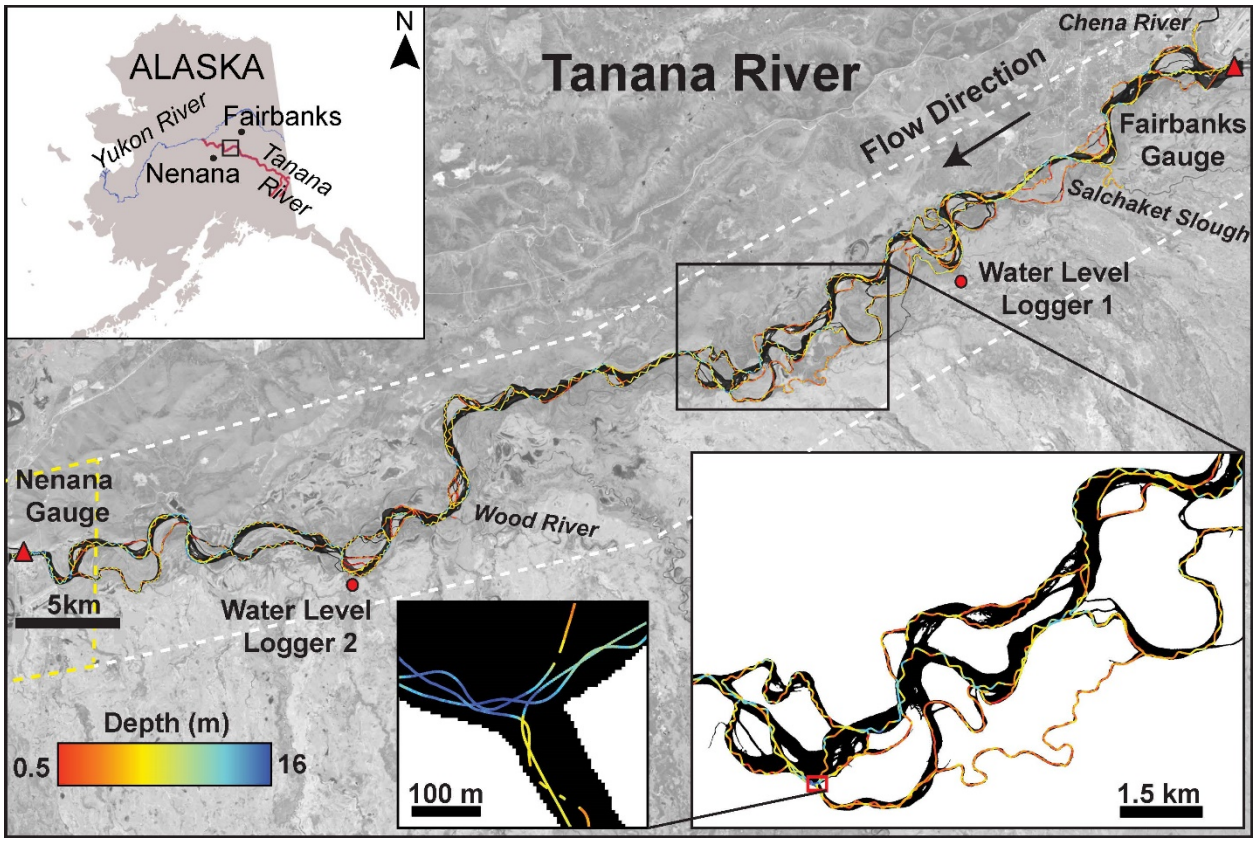

Figure 1.2: Location of the Tanana River shown using a Landsat 8 satellite image acquired on 06/18/2013. Bathymetric observations collected using a single-beam echo sounder during a field campaign between 07/01/2013 and 07/08/2013 are color coded along the river with close-up insets for detail. Locations of the USGS gauge stations (red triangles), internal water level loggers (red circles), and major tributaries are shown. RapidEye imagery extents used to create the river mask for the custom interpolation are shown for 07/12/13 in the white dashed lines and 05/28/13 in the yellow dashed lines.

The study reach contains multiple morphologies ranging from a single channel to as many as eight different channels in a cross section. It is an ideal site for this research because of its diverse morphology and because it is bounded by two USGS gauge stations needed for model boundary conditions (Figure 1.2). We define several subreaches based on changes in river

morphology (Figure 1.3). The first 16 km of the reach contains a primary main channel with an average width of ~450 m and smaller sloughs no wider than 100 m. Most of the flow is carried by the large main channel (Figure 1.3.1). In the next 27 km of the river, flow is partitioned into many anabranching channels ranging from 20 – 240 m wide that divert more of the flow around the main channel (Figure 1.3.2). About halfway through the study reach the anabranching channels converge into a single channel due to bedrock bluffs to the north. This reach continues for 15 km and only contains two small sloughs in addition to the main stem. Therefore, we expect this portion of the reach to behave hydraulically much like a single channel (Figure 1.3.3). The final 35 km subreach returns to a planform with several channels but remains more confined and less complex than the upstream anabranching subreach (Figure 1.3.4).

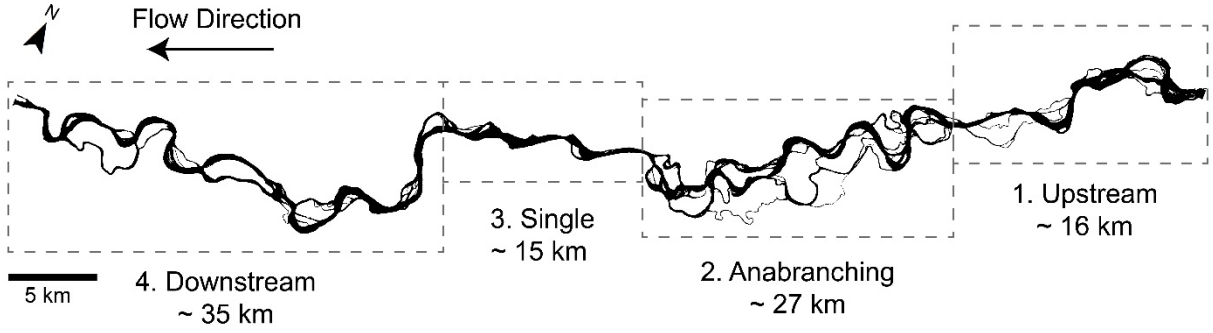

Figure 1.3: Extent of predefined subreaches used to calculate error statistics in the profile analysis.

1.4. Model Setup

1.4.1 Existing Datasets

Datasets needed to build the models tested here include a fine-resolution digital elevation model (DEM), bathymetry, and hydrometric information including river discharge and stage. We use an Alaska interferometric synthetic aperture radar (IfSAR) DEM

[*http://ifsar.gina.alaska.edu/*] with five-meter resolution for the floodplain topography. Mean vertical accuracy of the Alaska IfSAR products is three meters, and the horizontal accuracy is 12.2 meters. Errors in the floodplain topography are a low concern since the primary focus of this study is on in-channel hydraulics, and very little of the floodplain topography is inundated in our simulations. Discharge and stage records at 15-minute intervals from USGS gauge stations in Fairbanks and Nenana, Alaska provide model boundary conditions. The upstream boundary consists of time-varying discharge information, and the downstream boundary is a time series of stage. We add point-source discharge to the model at two locations to represent the Chena River and Salchaket Slough, which are inflowing tributaries. Salchaket Slough is a ~50 km long sub-channel of the Tanana River that splits from the main channel upstream of the Fairbanks gauge station and reenters below it. For the Chena River, we use USGS discharge records from a gauge station ~15 km upstream of the confluence with the Tanana. The distance between the Chena gauge station and the Tanana River confluence is unlikely to affect the model simulations because there are no inflowing point sources along the Chena between the gauge and the Tanana. Additionally, the Chena River flood wave's transit time is relatively small compared to the dynamics of the Tanana River flood wave. Salchaket Slough does not have a gauge station, so we estimate discharge based on *in situ* measurements acquired with a Sontek M9 acoustic doppler current profiling (ADCP) system [*http://www.sontek.com/productsdetail.php?RiverSurveyor-S5-M9-14*] during a separate field campaign on 8 June 2015. To measure discharge, we set up a cableway across Salchaket Slough just upstream of its confluence with the Tanana River. Six discharge measurements acquired between 3:15 and 3:30 PM ranged from 90.29 to 94.01 m^3/s, with an average discharge of 91.48 m^3/s. On this date, Salchaket Slough was contributing 14% of the downstream discharge

observed at the Nenana gauge station, and we assume that this percentage is constant in time. Adding discharge inputs from the Chena River and Salchaket Slough result in an average difference of 1% between the discharge records at the Fairbanks and Nenana model boundaries, thereby effectively closing the reach mass balance. We assume the discharge measurements are error-free, but in reality they are likely to have errors ranging between ± 6% and ± 19% [*Harmel et al.*, 2006; *Di Baldassarre and Montanari*, 2009; *Bates et al.*, 2013]. Reported channel conditions from USGS field measurements at the upstream boundary of our study site during the duration of our model simulations (July – September 2013) are described as follows: *Channel Stability* - Firm, *Channel Material* - Sand and Gravel, *Channel Evenness* - Even [*http://waterdata.usgs.gov/nwis/measurements*]. Based on these USGS reports and the increased likelihood that the Tanana River is subject to morphological changes, we estimate the discharge uncertainty in our model ranges between ± 10% and ± 20% [*Harmel et al.*, 2006]. Therefore, the actual uncertainty in discharge is probably considerably larger than the 1% discrepancy between the two gauges resulting from our analysis. Remaining discrepancies can likely be attributed to groundwater interactions with the river and other much smaller tributary inputs.

1.4.2 Field Measurements

Detailed bathymetric information is necessary to implement the 2D models. We collected measurements of channel bathymetry and WSE during a two-week field campaign from 29 June 2013 through 13 July 2013. In total, we collected depth and WSE at ~220,000 points using a single-beam SonarMite Echo Sounder v.3.0 and Trimble R9 survey-grade GPS system (Figure 1.2). Using a side-scanning sonar system was unfeasible due to high costs and risk of damage to the equipment in the harsh conditions of the Tanana River. We mounted the echo sounder and GPS unit on the right stern of a 28-foot aluminum-hulled riverboat. The

transducer was placed perpendicular to the water surface and submerged 0.18 m below the surface. Reported accuracy for the SonarMite Echo Sounder is ± 0.025 m [*http://www.ohmex.com/sonarmite.html*]. We were unable to compensate for roll or heave motion from the boat because the GPS antennas we had access to did not have National Marine Electronics Association (NMEA) capabilities. We took precautions to minimize roll and heave motions by traveling at a low speed of ~15 mph, though vessel motion likely increases uncertainty in the depth measurements.

We set the echo sounder and GPS to record every 0.5 seconds and matched bathymetric point observations to associated GPS locations using the recorded time stamps. To estimate error in the depth and WSE measurements, we identified 914 crossover point pairs in the observations within a 0.10 m radius of each other and calculated root mean square error (RMSE) for depth and WSE. RMSE for depth observations is 0.267 m and RMSE for WSE observations is 0.162 m. Bias is very small for both the depths and WSEs at -0.017 m and 0.016 m respectively. In addition to the bathymetry collection, we installed two Solinst pressure transducer water level loggers [*solinst.com*] at ~23 and ~70 km downstream of Fairbanks (Figure 1.2). We used differential GPS and WSE surveys to achieve elevation accuracy of ± 4 cm at the water logger sites. The water loggers recorded stage information at five-minute intervals from the start of our field campaign on 29 June 2013 through early September. We converted stage values to WSE by using an optical survey level and stadia rod to measure the difference between the water surface at the logger sites and GPS survey benchmarks on the banks of the river near the water loggers.

1.4.3 2D Channel Topography

We develop a custom interpolation method to transform the irregularly spaced bathymetric point data into a raster grid (Figure 1.4). Isotropic interpolation methods available

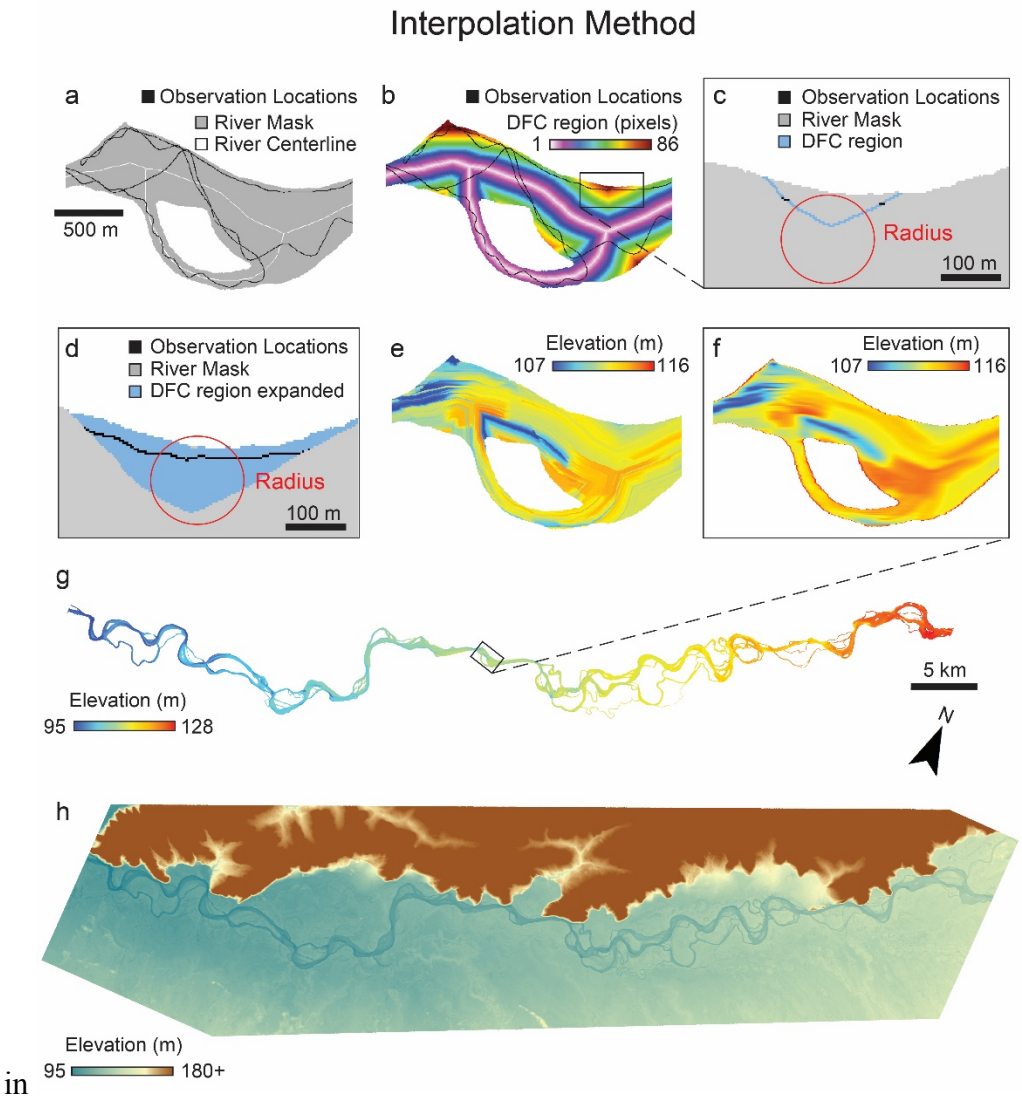

Figure 1.4: Schematic of the custom interpolation method. (a) Input needed for the interpolation. (b) Distance-from-centerline (DFC) image used to interpolate in the general flow orientation. (c) For each pixel, the DFC region is identified and all observation points are isolated to those falling within the DFC region and a specified radius. (d) The code expands into adjacent DFC regions to identify a minimum number of observations. (e) Inverse distance weighting (IDW) is performed on the observations. (f) A Gaussian smoothing filter is applied to the entire image. (g) Final interpolated output for the ~ 90 km river reach. (h) Final seamless DEM of the combined interpolated bathymetry and existing floodplain DEM (Alaska IfSAR).

ArcGIS and similar software do not produce hydrologically intuitive bathymetric patterns due to the anisotropic flow direction characteristic of rivers. We considered using other river-based interpolation methods that account for flow direction. The most common methods involve tailored search radii that utilize the anisotropic shape of a river cross-section [*Osting*, 2004], or channel-based coordinate systems guided by a channel centerline [*Smith and McLean*, 1984; *Goff and Nordfjord*, 2004; *Merwade et al.*, 2005, 2006, 2008; *Legleiter and Kyriakidis*, 2006, 2008; *Merwade*, 2009]. These methods are suitable for sinuous, single-channel systems where one centerline is applicable [*Smith and McLean*, 1984]. Extreme sinuosity, significant changes in direction, and braided channels are problematic for interpolation methods using channel-based coordinate systems [*Goff and Nordfjord*, 2004; *Legleiter and Kyriakidis*, 2008; *Merwade et al.*, 2008]. Implementing a standard channel transformation in a river like the Tanana that contains multiple flow centerlines and directions within a cross-section would require extensive manual work or multiple coordinate transformations and were thus discarded. The custom interpolation used for this study combines image processing techniques with similar concepts used in traditional channel transformations to adapt the search radius to interpolate points in the general flow directions of a multichannel river with little manual input.

Inputs needed for the interpolation are a set of channel centerlines calculated using the RivWidth software package [*Pavelsky and Smith*, 2008], a river mask, and the bathymetric point observations in TIFF format (Figure 1.4a). First, we create the river mask using five-meter resolution RapidEye imagery [*http://www.satimagingcorp.com/satellite-sensors/other-satellite-sensors/rapideye/*] acquired during the week of the field campaign on 12 July 2013 (Figure 1.2). The only exception is the image used for the westernmost seven kilometers of the study reach, which was acquired three months earlier in May of 2013 (Figure 1.2). This portion of the river

covered by the older RapidEye image is constrained by tall bedrock bluffs, so the planform of the river is unlikely to have changed substantially between May and our field campaign in July. We extract river inundation extent by thresholding a normalized difference water index (NDWI) transformation of the imagery [*McFeeters*, 1996]. To correct for areas near the riverbanks that are identified as river in the floodplain DEM and not in the imagery, we add these areas to the river mask. This correction is necessary to prevent interpolation artifacts in the DEM river surface from creating large errors in the model outputs, and the additional area accounts for a very small percentage (4.2%) of the total river surface area. We apply RivWidth to the river mask in order to create the channel centerline image needed for the interpolation, which consists of centerlines for every channel along the reach (Figure 1.4a). The interpolation code uses the centerline image to create regions parallel to the centerlines that represent the river's general flow orientation. These areas are defined by the distance from the centerline and are used to identify the optimal observations needed for interpolation (Figure 1.4b). We refer to these divisions as the distance-from-centerline (DFC) regions. The code identifies bathymetric point observations that fall within a defined radius of each river mask pixel and the DFC region of the pixel (Figure 1.4c). If a minimum number of observational points are not found within the DFC region and the specified radius, the search algorithm expands to include observations in adjacent DFC regions (Figure 1.4d). For this interpolation, we choose a search radius of 500 m and a minimum number of eight bathymetric observations. Once the minimum number of points is identified, the algorithm uses an inverse distance weighting (IDW) interpolation method (Figure 1.4e). The IDW formula to predict the bathymetric elevation for a given pixel location of unknown value is:

$$\hat{Z}(l_0) = \sum_{i=1}^{n} w_i Z(l_i) \tag{1.6}$$

where $\hat{Z}(l_0)$ is the predicted elevation for a given location (l_0), n is the number of observed sample points surrounding the prediction location, $Z(l_i)$ is the observed elevation value at location (l_i), and w_i are the weights assigned to each observed elevation point determined by the following formula:

$$w_i = d_{i0}^{-p} / \sum_{i=1}^{n} d_{i0}^{-p} \tag{1.7}$$

For greater distances, the weight is reduced by a factor of p, which we assign a value of five, and d_{i0} is the distance between the predicted location and each of the observed locations. This process is repeated for all river pixels. When the entire river is interpolated, we apply a Gaussian smoothing filter to remove high-frequency variability associated with data-sparse areas (Figure 1.4f,g).

The depth range for the echo sounder is 0.30-75 m [*http://www.ohmex.com/sonarmite.html*]. As a result, our survey includes few observations in very shallow portions of the river reach (≤0.30 m), and interpolated values are likely too deep in these areas. Without additional modifications, diagnostic model runs produce unrealistically low width variations. To diminish this problem, we apply corrections to the interpolation in shallow areas around submerged bars (Figure 1.5). First, we create a second river mask identifying areas of exposed bars at low summertime flows (1185.4 m^3/s) using RapidEye imagery acquired on 14 August 2012, and we use the river mask from the initial interpolation to define the high-water bar extents at higher flows (1449.3 m^3/s). This comparison allows us to convert stage differences between imagery dates to elevation values using field observations of WSE. Next, we create a bar mask from differences in the two river masks to isolate areas of exposed bars at

low water levels (Figure 1.5a). We use USGS gauge records to calculate stage differences between high and low water levels and to create stage contours that represent high and low bar extents (Figure 1.5b). To estimate the stage differences between these contours, we use the same IDW formula from the original interpolation (Figure 1.5c). Finally, we convert the stage differences to elevation changes using the field survey of spatially distributed WSEs (Figure 1.5d). This correction results in more realistic bar extents in areas that are not captured in the field data. We combine the final bathymetry with the floodplain DEM to create the topographic input for the model simulations (Figure 1.4h). Over time, the sand bars are likely to shift and change morphology due to the mobility of the Tanana riverbed. However, the timescale of the simulation and the moderate discharges observed in this study make it unlikely that there would be significant changes in the bars that would affect the model outputs. Once the DEM is finalized, we resample the 5 m DEM to 10 m, 25 m, 100 m, and 500 m resolutions using bilinear interpolation in ArcGIS.

We perform a bootstrapping error estimation for the bathymetry by randomly removing 20% of the observational points before implementing the interpolation and using the removed points to calculate RMSE. This bootstrapping method is common in other riverbed interpolation studies [*Osting*, 2004; *Merwade et al.*, 2006; *Merwade*, 2009]. To test the effects of the percentage of points removed, and random sample generation on the calculated errors, we perform a sensitivity analysis on the interpolation. Four different random samples removing 20% of the points are tested, as well as a single random sample removing 1%, 5%, 10%, and 20% of the points. We find the interpolation to be insensitive to the percentage of points and random sampling techniques used with a maximum difference in RMSE of 0.07 m. Final RMSE for the interpolated DEM is 0.890 m. Since the points we use to calculate errors in the

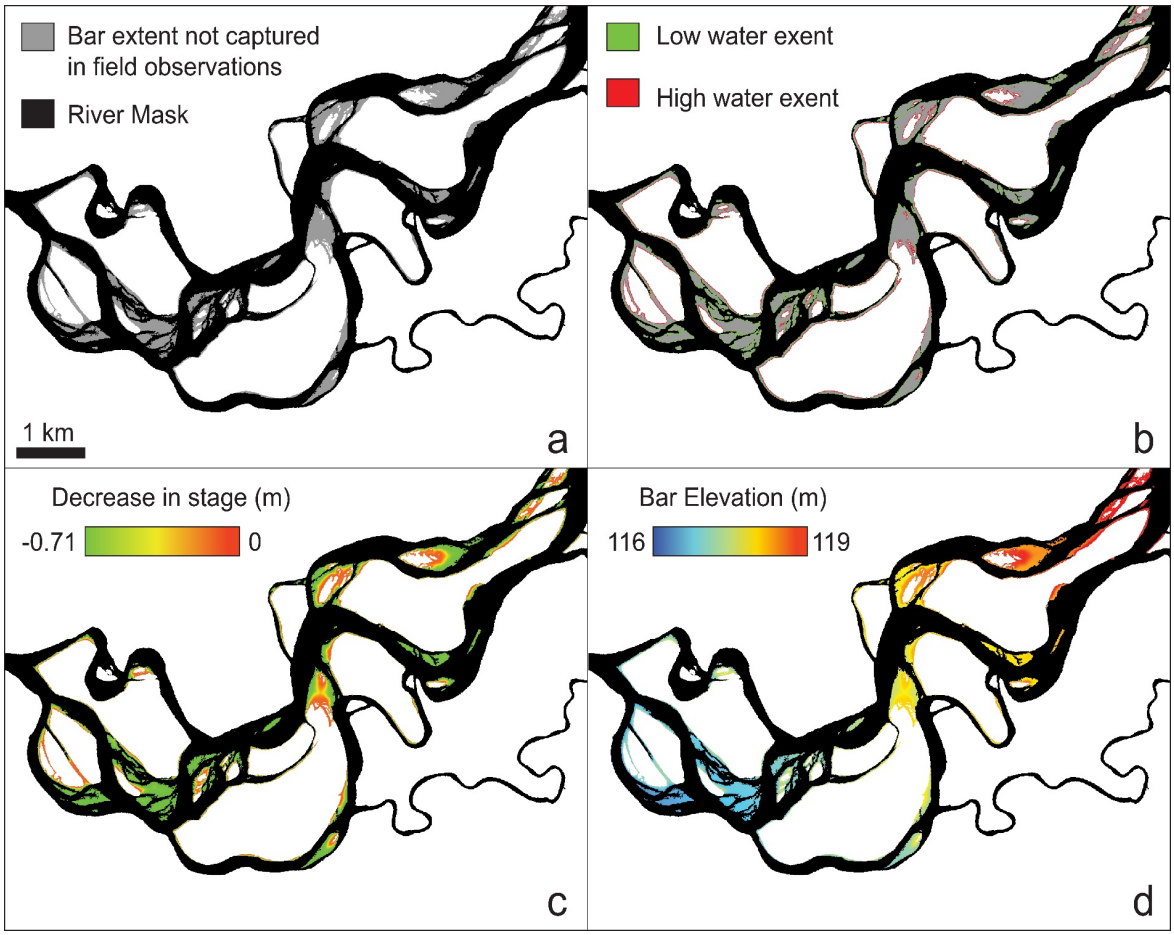

Figure 1.5: Schematic of the process used to correct submerged bar elevations in the interpolated bathymetry (Figure 1.4). (a) Submerged bar areas identified using RapidEye imagery at low water levels. (b) Contours of low and high water extents created using the bar areas. High water contours (red) were given a value of zero and low water contours (green) were assigned a negative stage value calculated using USGS gauge records. (c) Interpolated stage values for the identified bar areas. Inverse distance weighting (IDW) was used for interpolation. (d) Converted elevation values. Interpolated stage values were subtracted from linearly interpolated water surface elevation observations collected in the field.

bathymetry are extracted from the original depth observations, the estimated error is representative of areas in the bathymetry with higher observational density. In areas where we have limited observations, errors may be much greater than the calculated RMSE and could be a substantial contributor to model errors, especially in the 2D models where small variations in bathymetry are likely to have larger effects on WSE.

1.4.4 Model Structures

To test the effects of spatial resolution and dimensionality on model output, we build six different models (Table 1.1). The fundamental architecture of LISFLOOD-FP consists of a 2D floodplain component and a 1D channel component. In our study, discharge volumes throughout the simulations do not reach water levels high enough for overbank flow. Therefore, when referring to 1D/2D model structures we are solely referring to channelized flow dimensionalities and do not consider the 2D floodplain component as part of our model descriptions.

Model Acronym	Model Description	Simulation Time (mins)
10 m 2D	2D flow simulation of the river channels at 10 m resolution.	25,992
25 m 2D	2D flow simulation of the river channels at 25 m resolution.	2,588
100 m 2D	2D flow simulation of the river channels at 100 m resolution.	19.6
100 m SGC	Hybrid 1D/2D model: 2D flow simulation of the main river channel. 1D flow simulation of 32 channels with average widths narrower than the model resolution of 100 m using the subgrid solver.	9.8
500 m 1D-VAR	1D flow simulation of the entire river using the subgrid solver. Bathymetry varies in each grid cell and is estimated by averaging observational depths falling within a channel grid cell.	0.2
500 m 1D-AVG	1D flow simulation of the entire river using the subgrid solver. Bathymetric slope is estimated from an average depth value calculated from the observations.	0.2

Table 1.1: Model descriptions.

The most detailed model is a 2D, 10 m resolution model (10 m 2D) with 9,996,801 grid cells. We also run 2D simulations at 25 m (25 m 2D) and 100 m (100 m 2D) resolutions with 1,600,518 and 99,998 grid cells, respectively. In addition to the 2D simulations (Figure 1.1a,d), we build a hybrid 1D/2D model at 100 m resolution in which the main channel is represented in 2D and 32 smaller channels are represented as subgrid features in 1D (100 m SGC) (Figure 1.1b,e). This model contains the same number of grid cells as the 100 m 2D model but has additional representation of the 32 subgrid channels. Finally, we run two simulations at 500 m

resolution, in which a 1D main channel centerline represents the entire study reach (Figure 1.1c,e) and is treated as a subgrid channel so these models are effectively 1D with no 2D channel component. One of the 500 m simulations contains variable bed elevations along the reach (500 m 1D-VAR), and the other simulation contains a smooth bed slope created using an average water depth value for the entire reach (500 m 1D-AVG). Both 500 m models have 4,010 grid cells.

The models that include subgrid representations require specification of width and bed elevation values for each subgrid channel. We manually assign each subgrid channel in the 100 m SGC model an average width measured from the river mask and an average bed elevation calculated from the surveyed field observations. For each cell along the channel centerlines in the 500 m 1D models, we assign individual width and bed elevation values. We calculate width values from the five-meter resolution river mask using RivWidth and average the width values at 500 m resolution. For the 500 m 1D-VAR model, we average bed elevation observations within each grid cell, while for the 500 m 1D-AVG model we subtract the average water depth value from the observed WSE slope along the study reach.

1.5. Model Calibrations and Simulations

The main parameter needed for calibration in each model is the roughness coefficient, in this case Manning's *n*. We calibrate uniform roughness values for the river channel in each model using the spatially distributed observations of WSE and depth collected by boat from 1 July 2013 to 8 July 2013. We choose to use a uniform roughness value because this parameter compensates for many factors affecting the simulated flow, including the hydraulic resistance from bed formations, model dimensionality, grid resolution, model process representation, and errors in the boundary conditions [*Bates et al.*, 2013]. In a river as large as the Tanana, errors in

the inflow boundary conditions and bathymetry are likely to dominate model errors compared to small-scale variations in sediment composition. Additionally, the complex planform makes it difficult to identify obvious zones of different roughness values within the study reach. For the floodplain roughness, we assign a standard uniform value of 0.06. We do not calibrate the floodplain roughness value since there is no overbank flow occurring in our simulations.

Before running the calibrations, we correct the WSE variations between dates of the boat observations to July 1st using the temporally varying observations of WSE recorded by the water loggers. We test roughness values between 0.008 and 0.06 completing a total of 55 calibration runs per model. Model calibrations begin on 29 June 2013 and end on 2 July 2013. The first day of the simulations is model spin-up time. Once the calibrations are complete, we run 63-day dynamic simulations for each model from 29 June 2013 to 31 August 2013 using the optimal roughness value for each model. The simulations span the entire period measured by the two water loggers. Final computation times per simulation range from 0.2 minutes to 18 days on a 2.40 GHz Intel Xeon 6 core processor with 40 GB of RAM (Table 1.1). The LISFLOOD-FP code is parallelized to use all cores available on a machine.

1.6. Model Validation

We evaluate each model's ability to simulate inundation extent, temporally varying WSE, and spatial patterns in WSE and depth. To validate inundation extent, we compare model spatial outputs to a five-meter resolution river mask created with RapidEye imagery from 1 August 2013. The maximum variation in discharge at the Nenana gauge station on August 1st is 48 m^3/s. This range in flow comprises 2.5% of the average discharge of 1895 m^3/s on that date and is unlikely to result in changes to the channel extent within the observed river mask. We re-sample model outputs to five-meter resolution for direct comparison to the observed river mask and

classify both the observed and modeled outputs as inundated or dry pixels. Errors of commission are considered areas where the model produces inundated pixels and the observations show dry pixels, while errors of omission are areas where the model produces dry pixels and the observations show inundated pixels. We count inundated pixels in both the models and observations as correctly modeled areas. Lastly, we calculate a measure of fit statistic (also known as the Critical Success Index (CSI) in the meteorological forecast literature) to further assess the models' capabilities for simulating river inundation extent:

$$Fit\ (\%) = \frac{IA_{obs} \cap IA_{mod}}{IA_{obs} \cup IA_{mod}} \times 100 \tag{1.8}$$

The CSI compares the observed inundation (IA_{obs}) to the modeled inundation (IA_{mod}) and penalizes model over- and under- predictions [*Bates et al.*, 2010; *Sampson et al.*, 2015], but is not biased by the large and easy to predict areas observed and correctly simulated as dry.

To estimate spatial errors in model outputs, we use the 20% of survey points we removed before the bathymetric interpolation to calculate RMSE, mean bias, and absolute errors between model outputs and spatially distributed observations of WSE and depth. Additionally, we analyze WSE errors along 1D river profiles. We create the 1D profiles by deriving a centerline vector along the main channel of the river using RivWidth and compare the *in situ* WSE observations along the centerline to model-derived WSE. Since the spatial observations were collected from 1 July 2013 to 8 July 2013, we average the model spatial outputs from this timespan before comparing them to the observations. We then calculate RMSE and Nash-Sutcliffe Efficiency (NS) values [*McCuen et al.*, 2006] for the river profile and for each of the subreaches. Finally, we validate temporal fluctuations in modeled WSE by calculating NS values against observations at the two water logger locations. To assess the effects of discharge

uncertainty on model outputs, we perform a sensitivity analysis on the 25 m 2D model by running simulations with ± 10% and ± 20% differences in the upstream discharge.

1.7. Results

Model errors in spatially distributed WSE significantly increase and the CSI substantially worsens as model resolution coarsens and dimensionality decreases. The 10 m and 25 m 2D models are best at capturing spatially distributed WSE and inundation extent within the main channel and sub-channels (Figure 1.6). Absolute errors in spatially distributed WSE are lowest and evenly spread along the reach in the 25 m 2D and 10 m 2D models (Figure 1.6b). The primary area of over-predicted WSEs in these simulations occurs where the anabranching subreach converges into the single channel subreach. Improved RMSE from the 25 m to the 10 m 2D model is minimal for spatially distributed WSE but more substantial for depths, with a ~10 cm improvement in RMSE (Table 1.2). Along the observed profile, both models show similar patterns in WSE variations, but the 10 m 2D model slightly outperforms the 25 m 2D model at the downstream end of the study reach (Figure 1.7a,b, Table 1.3). The CSI for inundated area is strongest in the 10 m 2D (90.3%) and 25 m 2D (88.5%) models (Table 1.4). Both the 25 m and 10 m model resolutions are fine enough to capture proper channel morphology and sub-channel connectivity in 2D (Figure 1.6a). Primary errors of commission for the 10 m and 25 m 2D models result from bathymetric uncertainties in areas with little observational data, especially around bar formations. These shallow, erroneously inundated areas affect the CSI but do not substantially affect simulation of discharge. Roughness coefficients in the 10 m 2D and 25 m 2D model simulations are most consistent with the literature (Table 1.2). Roughness values can range from 0.026 to 0.08 in channels with morphological characteristics and sediment types similar to the Tanana River [*Chow*, 1959; *Arcement and Schneider*, 1989; *Toniolo*, 2013].

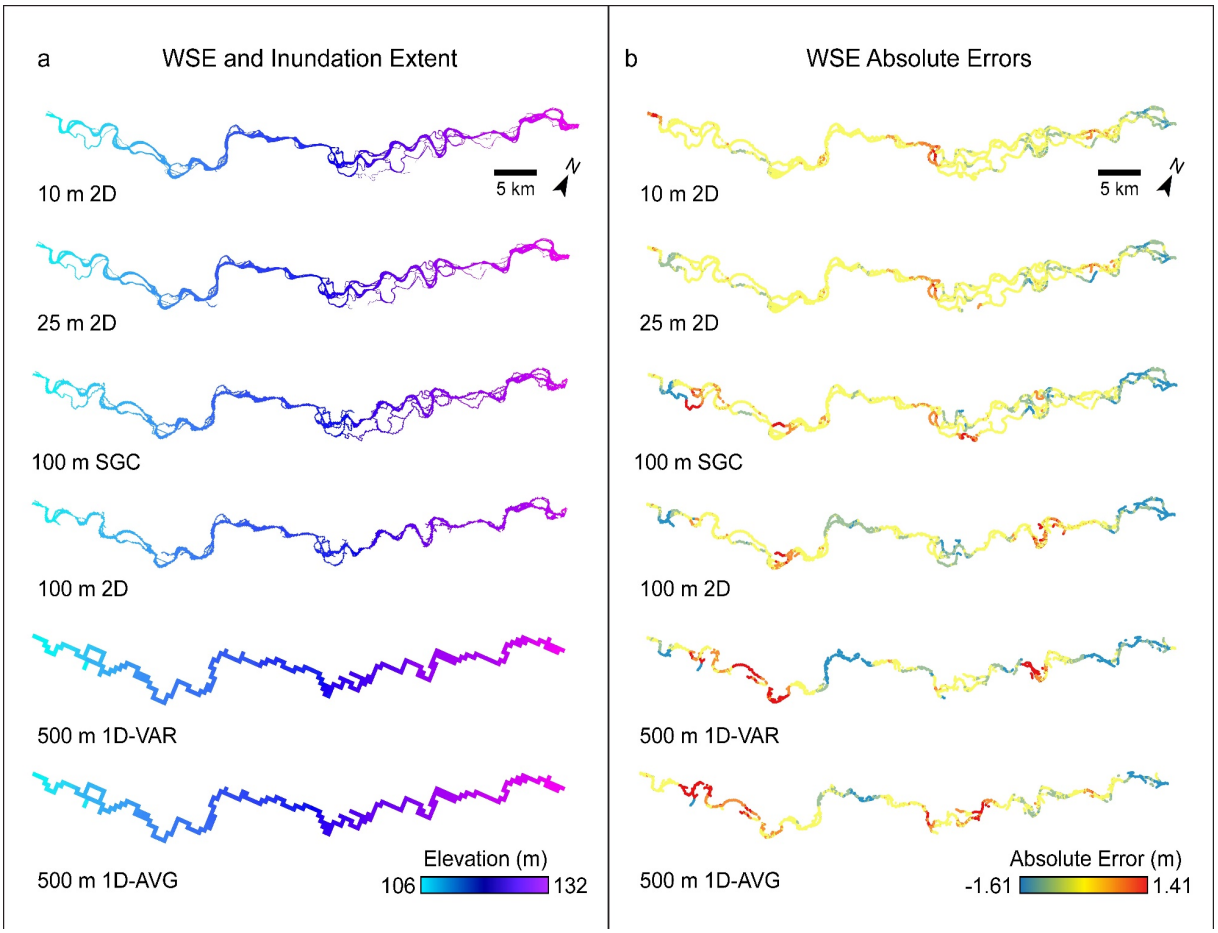

Figure 1.6: Spatial output of (a) WSE and inundation extent and (b) absolute errors between the modeled and observed WSE on 1 July 2013.

More prominent patterns in the errors of spatially distributed WSE become apparent in the 100 m model simulations (Figure 1.6b). The 100 m SGC model outperforms the 100 m 2D model by preserving channel connectivity with the inclusion of the 1D subgrid channels, which increases channel capacity and reduces overall errors in the anabranching subreach, in particular. In contrast, the 100 m 2D model tends to over-predict WSEs in the anabranching subreach. These over-predictions are likely a result of a decrease in channel capacity from the loss of the bifurcating channels at the coarser resolution (Figure 1.6b, Figure 1.7c,d). Additionally, incorporating the channel connectivity using the subgrid channels decreases RMSE by ~16% for spatially distributed WSE and ~7% for depths in the 100 m SGC model compared to the 100 m

MODEL	RMSE WSE (m)	RMSE Depth (m)	Bias WSE (m)	Bias Depth (m)	NSE Upstream	NSE Upstream (-Bias)	NSE Down-stream	NSE Down-stream (-Bias)	Roughness Coefficient
10 m 2D	0.226	0.712	-0.011	-0.075	0.341	0.945	0.844	0.881	0.023
25 m 2D	0.259	0.794	-0.014	-0.019	0.747	0.943	0.742	0.859	0.021
100 m SGC	0.318	1.51	-0.053	0.241	0.783	0.873	0.317	0.758	0.014
100 m 2D	0.379	1.62	0.0019	0.301	-2.258	0.903	0.633	0.756	0.011
500 m 1D-VAR	0.564	2.54	0.070	0.646	-5.199	0.709	-5.539	0.734	0.010
500 m 1D-AVG	0.352	1.88	0.028	0.321	-0.634	0.977	0.495	0.970	0.017

Table 1.2: Error statistics for spatial and temporal model outputs.

2D model (Table 1.2). The coarser resolution of the 100 m models approaches the limit for representing the Tanana River morphology in 2D by averaging out the small anabranching channels whilst preserving the larger main channels. Therefore, the CSIs for inundation extent in the 100 m models are lower than the 10 m and 25 m 2D models at 72.6% for the 100 m SGC model and 72.2% for the 100 m 2D model (Table 1.4).

The anabranching channel network is not simulated at 500 m resolution, and distinct alternating patterns emerge in the absolute errors of spatially distributed WSE (Figure 1.6). Absolute errors in both 500 m models alternate between under-predicting WSE by as much as 1.61 m and over-predicting WSE by 1.41 m (Figure 1.7e,f). These alternating patterns result in low mean biases for spatially distributed WSE in the 500 m models even though the models do not accurately represent the spatial dynamics. The 500 m 1D-AVG model shows 38% improvement in RMSE for spatial patterns of WSE compared to the 500 m 1D-VAR model, and a slightly better RMSE compared to the 100 m 2D model, though the alternating patterns in absolute errors are still present along the reach (Table 1.2, Figures 1.6b and 1.7f). In addition to

high errors in spatially distributed WSE, the 500 m models poorly predict inundated area, with CSIs

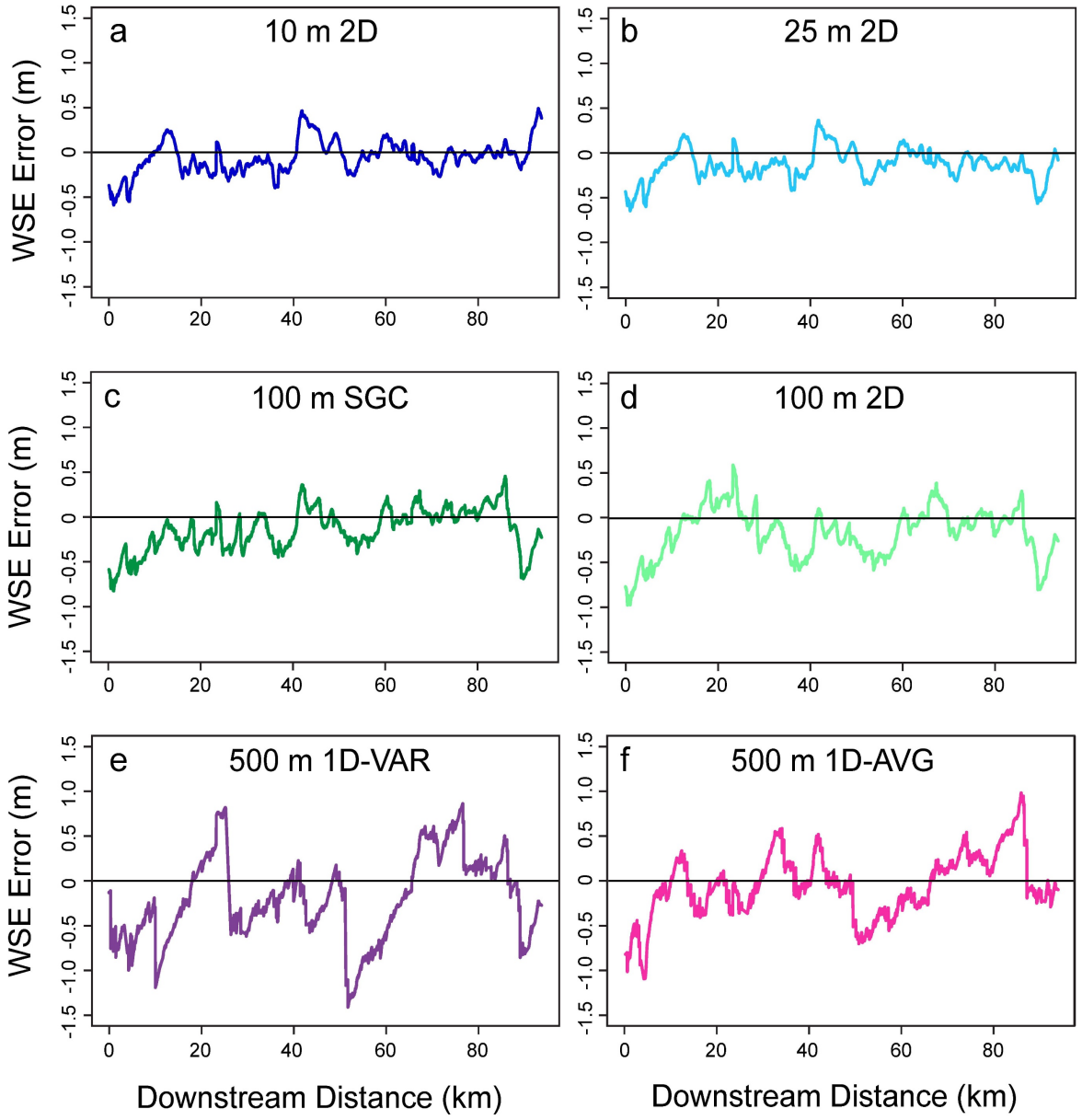

Figure 1.7: Plots of modeled WSE errors along the main channel profile.

around 41% (Table 1.4). These low CSIs are due to large over-predictions in inundated area as a result of the coarse grid size, which averages the main channel and sub-channels into a single

raster cell (Figure 1.6a). Roughness coefficients decrease as model process representation simplifies from the 2D models to the 500 m 1D-VAR model, with the exception of the 500 m

	Entire Reach		1. Upstream		2. Anabranching		3. Single		4. Downstream	
MODEL	RMSE	NS	RMSE	NS	RMSE	NS	RMSE	NS	RMSE	NS
10 m 2D	0.194	0.9990	0.282	0.9595	0.207	0.9889	0.160	0.9708	0.137	0.9952
25 m 2D	0.217	0.9988	0.309	0.9514	0.207	0.9889	0.174	0.9652	0.187	0.9911
100 m SGC	0.276	0.998	0.437	0.9029	0.256	0.983	0.194	0.9571	0.216	0.9881
100 m 2D	0.322	0.9973	0.475	0.8854	0.285	0.9789	0.329	0.8761	0.245	0.9846
500 m 1D-VAR	0.517	0.993	0.627	0.8073	0.359	0.9672	0.745	0.3664	0.415	0.956
500 m 1D-AVG	0.351	0.9968	0.452	0.8996	0.259	0.9829	0.396	0.8210	0.332	0.9719

Table 1.3: Error statistics of WSE along the main channel profile. Column numbers and headings coincide with the subreaches defined in Figure 1.3.

1D-AVG model, which displays a roughness value higher than both the 100 m models and 500 m 1D-VAR model (Table 1.2). The increase in model roughness value in the 500 m 1D-AVG model is likely a result of its smoother bathymetric slope. The variations in the bed topography in the 100 m and 500 m 1D-VAR models have higher friction effects compared to the smooth bed slope of the 500 m 1D-AVG model. This increase in friction from the bed topography in the 100 m and 500 m 1D-VAR models requires a lower roughness coefficient compared to the 500 m 1D-AVG model to balance the higher bathymetric roughness.

Temporal variations in WSE from all models at both water logger locations show good agreement with observations in predicting WSE fluctuations, but large biases from the observed WSEs occur depending on the model structure. Time series of WSE outputs and errors for each model are shown in Figure 1.8, and associated NS values are in Table 1.2. Upstream water

logger results show consistent over-predictions in the 500 m 1D-VAR and 100 m 2D models, and consistent under-predictions in the 500 m 1D-AVG model. These poor model performances are reflected in the NS values, which are well below zero. The large deviations are likely caused by spatial biases stemming from bathymetric uncertainties and reduced channel connectivity that result in over-predictions in WSE levels at the upstream water logger location in the 500 m 1D-VAR and 100 m 2D models. By comparison, the 100 m SGC and 25 m 2D models produce more accurate temporal dynamics with NS values of 0.783 and 0.747, respectively. The 25 m 2D model follows the observations most closely during low water intervals, while the 10 m 2D model under-predicts WSE, reducing the upstream NS value to 0.341. During high stage intervals the 100 m SGC, 25 m 2D, and 10 m 2D models all under-predict WSE (Figure 1.8a,c).

MODEL	Correctly Modeled Area (%)	Errors of Commission (%)	Errors of Omission (%)	Critical Success Index (%)
10 m 2D	96.42	6.69	3.58	90.37
25 m 2D	95.41	7.80	4.59	88.51
100 m SGC	88.66	22.17	11.34	72.57
100 m 2D	80.04	10.84	19.96	72.21
500 m 1D-VAR	70.51	72.74	29.49	40.82
500 m 1D-AVG	71.20	73.17	28.80	41.12

Table 1.4: Percentage statistics and measure of fit for modeled river inundation extent.

WSE dynamics at the downstream water logger show reverse patterns for most of the models. The 500 m 1D-VAR model continues to over-predict WSE by about half a meter. However, the 500 m 1D-AVG model switches from consistently under-predicting WSE at the upstream location to being much closer to the observations at the downstream location with an improved NS value of 0.495. The other four models tend to over-predict WSE at low water intervals and come closer to the observations at high water intervals (Figure 1.8b,d). Performances between the 100 m SGC and 100 m 2D models switch at the downstream location with the 100 m SGC model's NS value dropping to 0.317 and the 100 m 2D model's NS value

increasing to 0.633. The 25 m 2D model performance stays consistent downstream with an NS value of 0.742, while the 10 m 2D model performance improves with an NS value of 0.844 (Table 1.2).

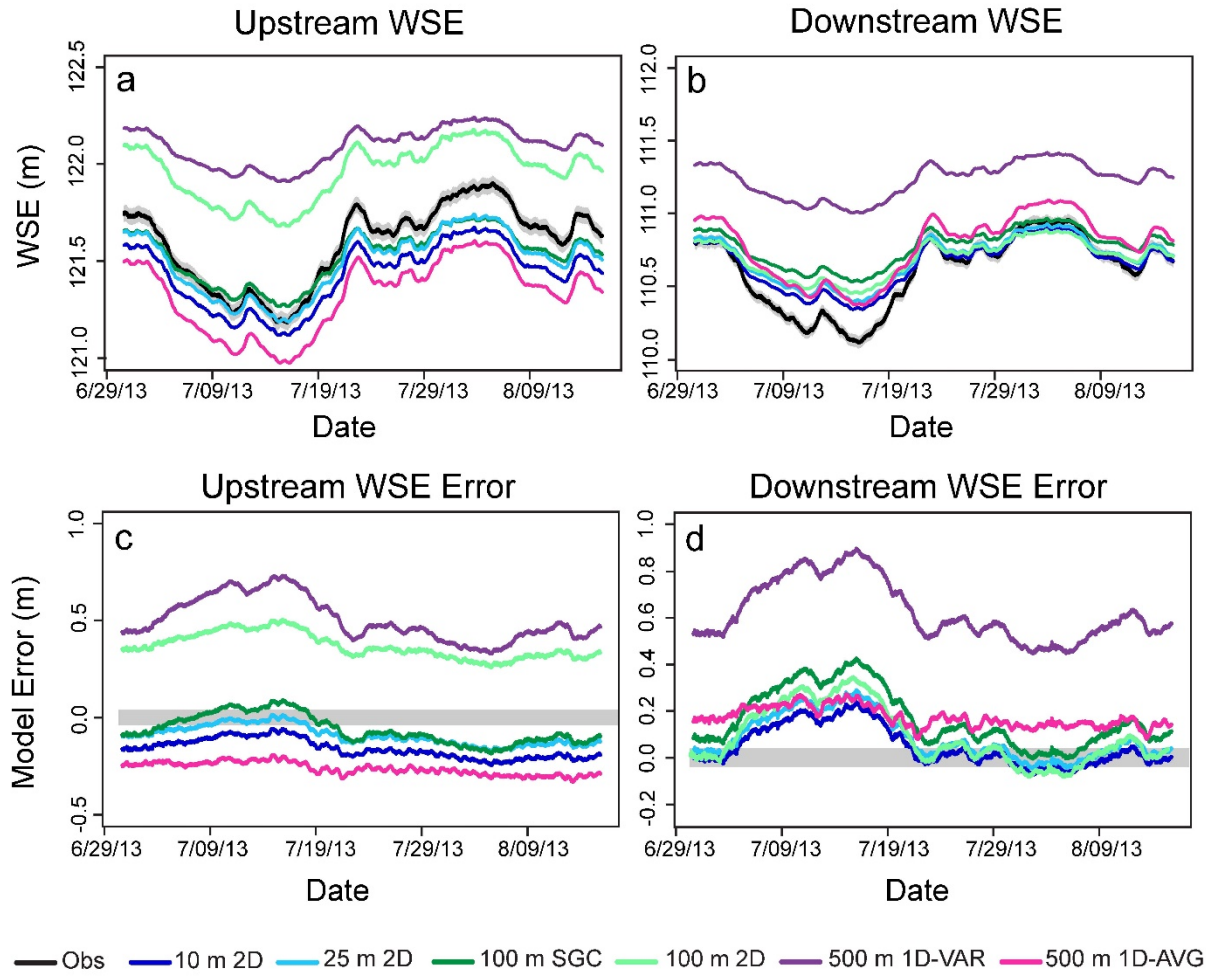

Figure 1.8: Temporal variations and absolute errors in modeled WSE. The (a,c) upstream and (b,d) downstream water logger locations are ~23 and ~70 km downstream of Fairbanks, respectively (Figure 1.2). Panels (a) and (b) display the modeled WSEs versus observations over time, while panels (c) and (d) display model WSE errors. Grey shaded areas represent observational errors.

To determine the effects of spatial errors on temporal outputs, we subtracted the mean bias for each model at the upstream and downstream water logger locations and re-calculated NS values (Table 1.2). Variances in model performances decrease and NS values for all models

greatly increase when subtracting out the biases. However, model performances gradually diminish as the resolution coarsens and dimensionality decreases. The one exception is the 500 m 1D-AVG model, which shows the best and most consistent performance after subtracting out the mean bias with NS values of 0.977 upstream and 0.970 downstream.

Observational errors for the water loggers are small at ± 0.04 m and do not significantly affect the temporal results. However, errors in discharge associated with the model boundary conditions could have a substantial effect on model outputs. Results of the sensitivity analysis show a 14-62% increase in spatial RMSE for a ± 10% to ± 20% change in discharge. Additionally, depending on spatial location of the observations, NS values for temporal model outputs drop well below zero for a ± 20% change in discharge and display a large range in NS values of -0.005 to 0.873 for a ± 10% change in discharge.

1.8. Discussion & Conclusion

This study is the first to test a simple, raster-based model's ability to simulate 2D, in-channel flows along a ~100 km reach of a multichannel river. We find that given proper parameterization and input information, raster-based models like LISFLOOD-FP can produce accurate 2D simulations of spatial patterns in WSE and inundation extent. Both the 10 m 2D and 25 m 2D models produce RMSE values less than 0.26 m for spatially distributed WSE and have a CSI for inundation extent of at least 89% (Table 1.2, Table 1.4). These CSIs approach the maximum performance achieved when using hydraulic models, even when built using detailed LiDAR data [*Bates et al.*, 2006; *Neal et al.*, 2009]. RMSE for the spatially distributed observations of WSE and depth are 0.162 m and 0.267 m, suggesting that observational error likely accounts for a significant portion of the model errors, in addition to discharge uncertainties and model structural errors.

Bathymetric uncertainties likely exert a dominant control on patterns in spatially distributed WSE errors in both the 10 m and 25 m 2D models. Certain areas of the Tanana were inaccessible by boat due to shallow sub-channels, log jams, or submerged bars. This inaccessibility results in little to no observational data in these areas and larger uncertainties in the interpolated bathymetry. Based on the interpolation results, errors in the bathymetry that are father away from our observations could be greater than 0.890 m. These bathymetric uncertainties likely manifest as higher localized errors in modeled WSE in the small sub-channels and in areas of significant change in planform along the reach (Figure 1.6b). For example, the 2D models tend to over-predict WSE in areas where multiple channels collapse into a single channel. The larger WSE errors in areas of morphological change could also be a result of model structural errors from the exclusion of advection in the momentum equation. Additionally, the uniform roughness coefficient used here likely fails to capture spatial variations present in an environment as complex as the Tanana. It is possible that errors occurring at significant morphological transitions, as well as some of the errors caused by bathymetric uncertainties, could be lowered using spatially varying roughness coefficients along the reach. More research is needed to investigate the controlling factors on roughness values in multichannel rivers at reach-scales ≥100 km.

Analysis of temporal dynamics in WSE highlights larger differences between the 10 m and 25 m 2D models. At the downstream water logger location, both models produce reasonable NS values, though they slightly over-predict WSE at low water intervals. However, at the upstream water logger location, the 10 m 2D model's performance drops substantially in comparison to the 25 m 2D model due to consistent under-predictions of WSE throughout the span of the simulation (Table 1.2, Figure 1.8). Differences in temporal WSE variations between

the 10 m and 25 m 2D models are likely caused by spatial biases due to bathymetric uncertainties and differences in channel connectivity due to model resolution. The finer spatial resolution of the 10 m model allows better connectivity in some of the anabranching sub-channels compared to the 25 m model (Figure 1.6a). This increase in channel connectivity, combined with bathymetric errors, likely distributes more flow to the sub-channels upstream of the water logger location, which decreases the flow and lowers WSE in the main channel where the observations are recorded. The effect of spatial biases in the temporal results is demonstrated when subtracting out the mean bias in the model outputs. Without spatial biases, the 10 m 2D and 25 m 2D models have negligible differences in NS values at the upstream and downstream water logger locations (Table 1.2). In the future, access to a larger observational network of water loggers measuring temporally varying WSE would provide more insight into model limitations and spatiotemporal controls on WSE throughout the study reach.

Despite limitations, results from the 2D model analysis demonstrate the practical application of a simple, raster-based model in simulating 2D channel hydraulics in multichannel river environments across 100 km reach scales. These efficient 2D models are important for future analysis of new remote sensing observations from sensors such as the Surface Water and Ocean Topography Mission (SWOT), which is scheduled to launch in 2021 [*Biancamaria et al., 2016*]. SWOT aims to record spatially-continuous, 2D observations of WSE and slope for the world's rivers 50-100 m in width and greater [*http://swot.jpl.nasa.gov/*]. However, it is not clear how effectively SWOT will observe multichannel systems. Fine-resolution, 2D model outputs of in-channel WSE are needed for pre-launch simulation and post-launch data assimilation of SWOT observations [*Durand et al.*, 2008; *Biancamaria et al.*, 2011, 2016; *Bates et al.*, 2014].

Additionally, scientists and managers can use efficient 2D models like those tested here to help identify areas that are vulnerable to flooding in these complex environments [*Surian*, 2015].

Comparisons between the detailed 2D models and models of lower dimensionality and coarser resolution reveal that bathymetry is a predominant control on WSE in the finer resolution 2D models, while simplifications to the multichannel network exert a larger control on WSE in the coarser resolution, 1D models. The 10 m and 25 m 2D models provide the highest level of process representation along the study reach. In these models, spatial and temporal errors in WSE are primarily influenced by spatial biases from bathymetric errors (Figures 1.6 and 1.8). As model resolution coarsens to 100 m, a combination of bathymetric uncertainties and improper channel connectivity dominate model errors. Many of the small sub-channels are lost in the anabranching subreach due to the coarser grid size in the 100 m 2D model. As a result, larger over-predictions in WSE occur in this subreach due to a decrease in channel capacity. Representing the smaller sub-channels using subgrid representations, as in the 100 m SGC model, results in more evenly spaced WSE errors and a ~16% decrease in RMSE. Additionally, including channel connectivity using the subgrid channels in the 100 m SGC model improves temporal WSE dynamics compared to the 100 m 2D model (Table 1.2, Figure 1.8).

The elimination of the anabranching morphology is the prominent factor influencing spatial and temporal hydraulics in the 500 m 1D models when compared to the finer resolution models. This is demonstrated through the differing bathymetric conditions in the 500 m models. The 500 m 1D-VAR model's bed slope contains larger variations along the reach compared to the smooth bed slope in the 500 m 1D-AVG model. While the smoother bed slope of the 500 m 1D-AVG model reduces the average spatial error in WSE compared to the 500 m 1D-VAR model, both models produce notable alternating patterns in spatially distributed WSE errors

(Figure 1.6b, Figure 1.7). These alternating errors are likely a result of unrealistic decreases or increases in channel capacity as the anabranching channels are averaged together at the coarser resolution and represented as single effective width values in the 1D model structure. Additionally, the general drop in roughness coefficients from the 2D models to the 1D models reflects the effects of simplifying the multichannel network. The decrease in roughness with coarser model resolution is likely due to the spatial averaging of bathymetry across multiple channels, which reduces the overall channel capacity and requires a lower friction value to convey the same discharge dynamics along the study reach. As a result, large biases emerge in the models' temporal dynamics that indicate the 500 m model performances are no better (or even worse) than the mean of the observations in many locations and are likely to misrepresent hydraulics in multichannel rivers like the Tanana.

Various 1D solvers, like the one in this study, are the primary hydraulic routing methods currently used in regional to global scale models [*Yamazaki et al.*, 2011; *Schumann et al.*, 2014b, 2016; *Sampson et al.*, 2015]. The results of this study demonstrate the importance of channel bifurcations and convergences in accurately simulating WSE in multichannel systems, which are not accounted for in regional and global models. As a result, these 1D solvers can produce significant model errors in spatial and temporal WSE dynamics in multichannel rivers due to the neglect of anabranching channels. Large errors in WSE along river reaches can result in improper flood predictions and slope estimates that could lead to incorrect discharge estimates in data sparse regions [*Durand et al.*, 2008].

Future development of regional to global scale models requires better observational data of WSE and bathymetry to calibrate and validate channel hydraulics in multichannel river environments. The SWOT mission plans to substantially improve spatial coverage of river WSE

and slope observations at regular temporal intervals, which will help to improve models through data assimilation and improved boundary conditions [*Bates et al.*, 2014; *Biancamaria et al.*, 2016]. In the meantime, regional and global scale models of large multichannel rivers can be improved by using downscaling techniques or subgrid channel schemes that allow for better representation of anabranching channel networks, rather than lumping the channel conveyance into a single effective centerline [*Neal et al.*, 2012a; *Schumann et al.*, 2014b; *Sampson et al.*, 2015]. If results on the Tanana hold true for other rivers, then models such as the 100 m SGC model presented here would come close to matching the accuracy of 2D simulations without the required computational burden.

REFERENCES

Allen, G. H., and T. M. Pavelsky (2015), Patterns of river width and surface area newly revealed by the satellite-derived North American River Width (NARWidth) dataset, *Geophys. Res. Lett.,* 42(2), 395-402, doi:10.1002/2014GL062764.

Arcement, G. J., and V. R. Schneider (1989), Guide for Selecting Manning's Roughness Coefficients for Natural Channels and Flood Plains United States, *United States Geological Survey*, Water-Supply Paper 2339.

Bates, P. D., and A. P. J. De Roo (2000), A simple raster-based model for flood inundation simulation, *J. Hydrol.*, 236(1-2), 54–77, doi:10.1016/S0022-1694(00)00278-X.

Bates, P. D., M. S. Horritt, N. M. Hunter, D. Mason, and D. Cobby (2005), Numerical modelling of floodplain flow, John Wiley and Sons Ltd.: Chichester, UK, 271-304.

Bates, P. D., M. D. Wilson, M. S. Horritt, D. C. Mason, N. Holden, and A. Currie (2006), Reach scale floodplain inundation dynamics observed using airborne synthetic aperture radar imagery: Data analysis and modelling, *J. Hydrol.*, *328*(1), 306–318, doi:10.1016/j.jhydrol.2005.12.028.

Bates, P. D., M. S. Horritt, and T. J. Fewtrell (2010), A simple inertial formulation of the shallow water equations for efficient two-dimensional flood inundation modelling, *J. Hydrol.*, *387*(1), 33–45, doi:10.1016/j.jhydrol.2010.03.027.

Bates, P. D., F. Pappenberger, R. J. Romanowicz (2013), Uncertainty in Flood Inundation Modelling. Applied uncertainty analysis for flood risk management, K. Beven, J. Hall (eds). *Imperial College Press: Singapore*, 232–269.

Bates, P. D., J. C. Neal, D. Alsdorf, and G. J. P. Schumann (2014), Observing Global Surface Water Flood Dynamics, *Surv. Geophys.*, *35*(3), 839–852, doi:10.1007/s10712-013-9269-4.

Beighley, R. E., K. G. Eggert, T. Dunne, V. Gummadi, and K. L. Verdin (2009), Simulating hydrologic and hydraulic processes throughout the Amazon River Basin, *Hydrol. Process.*, 23(8), 1221–1235, doi:10.1002/hyp.

Biancamaria, S., M. Durand, K. M. Andreadis, P. D. Bates, A. Boone, N. M. Mognard, E. Rodríguez, D. E. Alsdorf, D. P. Lettenmaier, and E. A. Clark (2011), Assimilation of virtual wide swath altimetry to improve Arctic river modeling, *Remote Sens. Environ.*, *115*(2), 373–381, doi:10.1016/j.rse.2010.09.008.

Biancamaria, S., D. P. Lettenmaier, and T. M. Pavelsky (2016), The SWOT Mission and its capabilities for land hydrology, *Surv. Geophys.*, 37(2), 307-337, doi:10.1007/s10712-015-9346-y.

Bierkens, M. F. P., V. A. Bell, P. Burek, N. Chaney, L. E. Condon, C. H. David, A. P. J. De

Roo, P. Döll, N. Drost, J. S. Famiglietti, M. Flörke, D. J. Gochis, P. Houser, R. Hut, J. Keune, S. Kollet, R. M. Maxwell, J. T. Reager, L. Samaniego, E. Sudicky, E. H. Sutanudjaja, N. van de Giesen, H. Winsemius, and E. F. Wood (2015), Hyper-resolution global hydrological modelling: what is next?: "Everywhere and locally relevant.", *Hydrol. Process.*, *29*(2), 310–320, doi:10.1002/hyp.10391.

Brabets, T. P., B. Wang, and R. H. Meade (2000), Environmental and hydrologic overview of the Yukon River Basin , Alaska and Canada, *US Dep. Inter. US Geol. Surv.*

Bradbrook, K. F., S. N. Lane, S. G. Waller, and P. D. Bates (2004), Two dimensional diffusion wave modelling of flood inundation using a simplified channel representation, *Int. J. River Basin Manag.*, 2(3), 211–223, doi:10.1080/15715124.2004.9635233.

Bridge, J. S. (1993), The interaction between channel geometry, water flow, sediment transport and deposition in braided rivers, *Geol. Soc. London, Spec. Publ.*, *75*(1), 13–71, doi:10.1144/GSL.SP.1993.075.01.02.

Chow, V. T. (1959), Open-Channel Hydraulics, 680 pp., McGraw-Hill, N. Y.

Cloke, H. L., and F. Pappenberger (2009), Ensemble flood forecasting: A review, *J. Hydrol.*, *375*(3), 613–626, doi:10.1016/j.jhydrol.2009.06.005.

Courant, R., K. Friedrichs, and H. Lewy (1928), Partial differential equations of mathematical physics, Math. Ann., 100, 32–74.

Cunge, J. A., F. M. Holly, and A. Verwey (1980), Practical Aspects of Computational River Hydraulics, 420 pp., Pitman, London, U.K.

de Almeida, G. A. M., P. D. Bates, J. Freer, and M. Souvignet (2012), Improving the stability of a simple formulation of the shallow water equations for 2-D flood modeling, *Water Resour. Res.*, *48*(5), doi:10.1029/2011WR011570.

de Almeida, G. A. M., and P. D. Bates (2013), Applicability of the local inertial approximation of the shallow water equations to flood modeling, *Water Resour. Res.*, *49*(8), 4833–4844, doi:10.1002/wrcr.20366.

Di Baldassarre, G., and A. Montanari (2009), Uncertainty in river discharge observations: a quantitative analysis, *Hydrol. Earth Syst. Sci.*, *13(6)*, 193-921, doi:10.5194/hessd-6-39-2009.

Dornblaser, M. M., and R. G. Striegl (2009), Suspended sediment and carbonate transport in the Yukon River Basin, Alaska: Fluxes and potential future responses to climate change, *Water Resour. Res.*, *45*(6), doi:10.1029/2008WR007546.

Durand, M., K. M. Andreadis, D. E. Alsdorf, D. P. Lettenmaier, D. Moller, and M. Wilson (2008), Estimation of bathymetric depth and slope from data assimilation of swath altimetry

into a hydrodynamic model, *Geophys. Res. Lett.*, *35*(20), doi:10.1029/2008GL034150.

Goff, J. A., and S. Nordfjord (2004), Interpolation of fluvial morphology using channel-oriented coordinate transformation: a case study from the New Jersey Shelf, *Math. Geol.*, *36*(6), 643–658, doi:10.1023/B:MATG.0000039539.84158.cd.

Harmel, R. D., R. J. Cooper, R. M. Slade, R. L. Haney, and J. G. Arnold (2006), Cumulative uncertainty in measured streamflow and water quality data for small watersheds, *Transactions of the ASABE*, *49*(3), 689–701, doi: 10.13031/2013.20488.

Horritt, M. S., and P. D. Bates (2001), Effects of spatial resolution on a raster based model of flood flow, *J. Hydrol.*, *253*(1), 239–249, doi:10.1016/S0022-1694(01)00490-5.

Horritt, M. S., and P. D. Bates (2002), Evaluation of 1D and 2D numerical models for predicting river flood inundation, *J. Hydrol.*, *268*(1), 87–99, doi:10.1016/S0022-1694(02)00121-X.

Horritt, M. S., P. D. Bates, and M. J. Mattinson (2006), Effects of mesh resolution and topographic representation in 2D finite volume models of shallow water fluvial flow, *J. Hydrol.*, *329*(1), 306–314, doi:10.1016/j.jhydrol.2006.02.016.

Hunter, N. M., P. D. Bates, M. S. Horritt, and M. D. Wilson (2007), Simple spatially-distributed models for predicting flood inundation: A review, *Geomorphology*, *90*(3), 208–225, doi:10.1016/j.geomorph.2006.10.021.

Javernick, L., D. M. Hicks, R. Measures, B. Caruso, and J. Brasington (2016), Numerical Modelling of Braided Rivers with Structure-from-Motion-Derived Terrain Models, *River Res. Appl.*, *32*(5), 1071–1081, doi:10.1002/rra.2918.

Lane, S. N., and K. S. Richards (1998), High resolution , two-dimensional spatial modelling of flow processes in a multi-thread channel, *Hydrol. Process.*, 12(8), 1279-*1298*, doi: 10.1002/(SICI)1099-1085(19980630)12:8<1279::AID-HYP615>3.0.CO;2-E.

Lane, S. N., K. F. Bradbrook, K. S. Richards, P. S. Biron, and A. G. Roy (1999), The application of computational fluid dynamics to natural river channels : three-dimensional versus two-dimensional approaches, *Geomorphology*, *29(1)*, 1–20, doi: 10.1016/S0169-555X(99)00003-3

Latrubesse, E. M. (2008). Patterns of anabranching channels: The ultimate end-member adjustment of mega rivers. *Geomorphology*, *101*(1), 130-145. doi: 10.1016/j.geomorph.2008.05.035.

Legleiter, C. J., and P. C. Kyriakidis (2006), Forward and inverse transformations between Cartesian and channel-fitted coordinate systems for meandering rivers, *Math. Geol.*, *38*(8), 927–958, doi:10.1007/s11004-006-9056-6.

Legleiter, C. J., and P. C. Kyriakidis (2008), Spatial prediction of river channel topography by

kriging, *Earth Surf. Process. Landforms*, *33(6)*, 841–867, doi:10.1002/esp.

McCuen, R. H., Z. Knight, and A. G. Cutter (2006), Evaluation of the Nash–Sutcliffe efficiency index, *J. Hydrol. Eng.*, *11*(6), 597–602, doi:10.1061/(ASCE)1084-0699(2006)11:6(597).

McFeeters, S. K. (1996), The use of the Normalized Difference Water Index (NDWI) in the delineation of open water features, *Int. J. Remote Sens.*, *17*(7), 1425–1432, doi:10.1080/01431169608948714.

Merwade, V. M., D. R. Maidment, and B. R. Hodges (2005), Geospatial representation of river channels, *J. Hydrol. Eng.*, 10(3), 243–251, doi:10.1061/(ASCE)1084-0699(2005)10:3(243) CE.

Merwade, V. M., D. R. Maidment, and J. A. Goff (2006), Anisotropic considerations while interpolating river channel bathymetry, *J. Hydrol.*, *331*(3), 731–741, doi:10.1016/j.jhydrol.2006.06.018.

Merwade, V., A. Cook, and J. Coonrod (2008), GIS techniques for creating river terrain models for hydrodynamic modeling and flood inundation mapping, *Environ. Model. Softw.*, *23*(10), 1300–1311, doi:10.1016/j.envsoft.2008.03.005.

Merwade, V. (2009), Effect of spatial trends on interpolation of river bathymetry, *J. Hydrol.*, *371*(1), 169–181, doi:10.1016/j.jhydrol.2009.03.026.

Neal, J. C., P. D. Bates, T. J. Fewtrell, N. M. Hunter, M. D. Wilson, and M. S. Horritt (2009), Distributed whole city water level measurements from the Carlisle 2005 urban flood event and comparison with hydraulic model simulations, *J. Hydrol.*, *368*(1), 42–55, doi:10.1016/j.jhydrol.2009.01.026.

Neal, J., G. J. P. Schumann, and P. D. Bates (2012a), A subgrid channel model for simulating river hydraulics and floodplain inundation over large and data sparse areas, *Water Resour. Res.*, *48*(11), doi:10.1029/2012WR012514.

Neal, J., I. Villanueva, N. Wright, T. Willis, T. Fewtrell, and P. D. Bates (2012b), How much physical complexity is needed to model flood inundation?, *Hydrol. Process.*, *26*(15), 2264–2282, doi:10.1002/hyp.8339.

Nguyen, P., A. Thorstensen, S. Sorooshian, K. Hsu, A. AghaKouchak, B. Sanders, V. Koren, Z. Cui, and M. Smith (2015), A high resolution coupled hydrologic–hydraulic model (HiResFlood-UCI) for flash flood modeling, *J. Hydrol.*, doi:10.1016/j.jhydrol.2015.10.047.

Nicholas, A. P., and G. H. Sambrook Smith (1999), Numerical simulation of three-dimensional flow hydraulics in a braided channel, *Hydrol. Process.*, *13(6), 913-929*, doi: 10.1002/(SICI)1099-1085(19990430)13:6<913::AID-HYP764>3.0.CO;2-N

Nicholas, A. P., S. D. Sandbach, P. J. Ashworth, M. L. Amsler, J. L. Best, R. J. Hardy, S. N.

Lane, O. Orfeo, D. R. Parsons, A. J. H. Reesink, G. H. Sambrook Smith, and R. N. Szupiany (2012), Modelling hydrodynamics in the Rio Paraná, Argentina: An evaluation and inter-comparison of reduced-complexity and physics based models applied to a large sand-bed river, *Geomorphology*, *169*, 192–211, doi:10.1016/j.geomorph.2012.05.014.

Osting, T. D. (2004), An improved anisotropic scheme for interpolating scattered bathymetric data points in sinuous river channels. *Cent. Res. Water Resour., University of Austin*.

Paiva, R. C. D., W. Collischonn, and C. E. M. Tucci (2011), Large scale hydrologic and hydrodynamic modeling using limited data and a GIS based approach, *J. Hydrol.*, *406*(3), 170–181, doi:10.1016/j.jhydrol.2011.06.007.

Paiva, R. C. D., W. Collischonn, and D. C. Buarque (2013), Validation of a full hydrodynamic model for large-scale hydrologic modelling in the Amazon, *Hydrol. Process.*, *27*(3), 333–346, doi:10.1002/hyp.8425.

Pavelsky, T. M., and L. C. Smith (2008), RivWidth : A software tool for the calculation of river widths from remotely sensed imagery, *IEEE Geosci. Remote Sens. Lett.*, *5*(1), 70–73, doi: 10.1109/lgrs.2007.908305

Sampson, C. C., A. M. Smith, P. D. Bates, J. C. Neal, L. Alfieri, and J. E. Freer (2015), A high-resolution global flood hazard model, *Water Resour. Res.*, 51(9), 7358–7381, doi:10.1002/2015WR016954.Received.

Schubert, J. E., W. W. Monsen, and B. F. Sanders (2015), Metric-Resolution 2D River Modeling at the Macroscale: Computational Methods and Applications in a Braided River, *Front. Earth Sci.*, *3*, 74, doi:10.3389/feart.2015.00074.

Schumann, G. J. P., P. D. Bates, J. C. Neal, and K. M. Andreadis (2014a), Fight floods on a global scale, *Nature, 507(7491), 169-169.* doi:10.1038/507169e.

Schumann, G. J. P., K. M. Andreadis, and P. D. Bates (2014b), Downscaling coarse grid hydrodynamic model simulations over large domains, *J. Hydrol.*, *508*, 289–298, doi:10.1016/j.jhydrol.2013.08.051.

Schumann, G. J. P., D. Stampoulis, A. M. Smith, C. C. Sampson, K. M. Andreadis, J. C. Neal, & P. D. Bates (2016), Rethinking flood hazard at the global scale, *Geophy. Res. Lett.*, *43*(19), doi: 10.1002/2016GL070260.

Smith, J. D., and S. R. McLean (1984), A model for flow in meandering streams, *Water Resour. Res.*, *20*(9), 1301–1315, doi:10.1029/WR020i009p01301.

Surian, N. (2015), Fluvial Processes in Braided Rivers, in *Rivers-Physical, Fluvial and Environmental Processess*, 255–277. doi: 10.1007/978-3-319-17719-9_15.

Toniolo, H., P. Duvoy, S. Vanlesberg, and J. Johnson (2010), Modelling and field measurements

in support of the hydrokinetic resource assessment for the Tanana river at Nenana, Alaska, *Proc. Inst. Mech. Eng. Part A: J. Power Energy*, *224*(8), 1127–1139, doi:10.1243/09576509JPE1017.

Toniolo, H. (2013), Bedforms andsediment characteristics along the thalweg on the Tanana River near Nenana, Alaska, USA, *Nat. Resour.*, *04*(01), 20–30, doi:10.4236/nr.2013.41003.

Williams, R. D., J. Brasington, M. Hicks, R. Measures, C. D. Rennie, and D. Vericat (2013), Hydraulic validation of two-dimensional simulations of braided river flow with spatially continuous aDcp data, *Water Resour. Res.*, *49(9)*, 5183–5205, doi:10.1002/wrcr.20391.

Yamazaki, D., S. Kanae, H. Kim, and T. Oki (2011), A physically based description of floodplain inundation dynamics in a global river routing model, *Water Resour. Res.*, *47(4)*, doi:10.1029/2010WR009726.

Ziliani, L., N. Surian, T. J. Coulthard, and S. Tarantola (2013), Reduced-complexity modeling of braided rivers: Assessing model performance by sensitivity analysis, calibration, and validation, *J. Geophys. Res. Earth Surf.*, *118(4)*, 2243–2262, doi:10.1002/jgrf.20154.

CHAPTER 2: AIRSWOT MEASUREMENTS OF RIVER WATER SURFACE ELEVATION AND SLOPE: TANANA RIVER, AK[2]

2.1. Introduction

Rivers play a critical role in earth's water cycle by transporting surface runoff to the oceans. In doing so, they provide key ecological habitat, play an important part in nutrient cycling, act as navigation pathways for trade and recreation, and help sustain human life as sources of fresh water. Research over the past several decades reveals a growing urgency to monitor the globe's spatial and temporal surface water fluxes as they adjust to climate change [*Famiglietti and Rodell*, 2013; *Bates et al.*, 2014; *Clark et al.*, 2015; *Rodell et al.*, 2015]. However, existing *in situ* and remote sensing methods for measuring rivers and lakes have limitations that prevent a consistent and comprehensive view of global-scale surface water dynamics [*Alsdorf et al.*, 2007b; *Schumann et al.*, 2009; *Bates*, 2012].

Remote sensing technology provides intriguing new ways to address the limitations of *in situ* observations, which often fail during overbank flows and are unavailable in many parts of the globe [*Hannah et al.,* 2011; Di *Baldassarre and Uhlenbrook*, 2012]. Optical sensors such as Landsat and SPOT can accurately observe inundation extent, but they cannot measure WSEs and are limited by clouds and darkness [*Marcus and Fonstad*, 2008]. Several types of active radars

[2]This chapter previously appeared as an article in Geophysical Research Letters. The original citation is as follows: Altenau, E. H., T. M. Pavelsky, D. Moller, C. Lion, L. H. Pitcher, G. H. Allen, P. D. Bates, S. Calmant, M. Durand, and L. C. Smith (2017), AirSWOT measurements of river water surface elevation and slope: Tanana River, AK, *Geophys. Res. Lett*., 1–9, doi:10.1002/2016GL071577.

overcome the drawbacks of optical sensors, though all current systems also have limitations of their own [*Smith*, 1997; *Calmant et al.*, 2008; *Schumann et al.*, 2009]. Radar altimetry measurements from sensors such as Jason-2 and ENVISAT provide point-based measurements of river WSEs, which can be used to interpolate slopes and develop stage-discharge relationships [*O'Loughlin et al.*, 2013; *Paris et al.*, 2016]. However, altimeter observations have low spatial and temporal resolutions, with vertical errors of decimeters to meters [*Calmant et al.*, 2008; *Biancamaria et al.*, 2016a; *O'Loughlin et al.*, 2016]. Interferometric synthetic aperture radar (InSAR) images can recover WSE changes under inundated vegetation, but existing spaceborne InSARs cannot ordinarily retrieve WSEs over open water [*Alsdorf et al.*, 2007a]. Therefore, current remotely sensed measurements of WSEs and slopes are constrained by resolutions and accuracies that limit the visibility of surface waters at global scales [*Alsdorf et al.*, 2007b; *Bates*, 2012; *Garambois et al.*, 2016].

The Surface Water and Ocean Topography (SWOT) Mission aims to address the principal limitations of remote sensing for estimating surface water fluxes [*Biancamaria et al.*, 2016b]. SWOT is expected to provide simultaneous, 2D measurements of WSEs for many of the world's prominent rivers, lakes, and wetlands, with decimeter-level accuracy over 1 km^2 areas [*Pavelsky et al.,* 2014]. *Biancamaria et al.* [2016b] provides further information regarding the capabilities and limitations of SWOT to measure rivers and lakes. AirSWOT, an airborne instrument that produces radar measurements analogous to (but not identical to) SWOT, was designed to assess sensor capabilities, develop algorithms, and eventually validate SWOT measurements. Unlike SWOT, AirSWOT provides an opportunity to explore important questions regarding river hydraulics at spatial and temporal resolutions unattainable by satellites. To date, however, there has been no published evaluation of AirSWOT's ability to accurately

measure these important hydrologic variables or the spatial scales required for averaging the data in order to meet the proposed accuracies.

Here, we present analysis of new measurements of river WSE and slope acquired on June 9, 2015 during an AirSWOT campaign over the Tanana River, Alaska. The objectives of this study are to (1) determine the WSE and slope errors associated with AirSWOT measurements of rivers, (2) to evaluate AirSWOT's effectiveness as a validation instrument for the SWOT hydrology measurements, and (3) to explore whether AirSWOT's measurements are precise enough to capture centimeter-per-kilometer-scale variations in river slope, which are critical for characterizing reach-scale river hydraulics. More detailed measurements of WSE and slope are needed to understand the primary factors controlling slope variability along river systems, which are essential for predicting floods and for defining reaches used to estimate discharge from remotely sensed data [*Durand et al.,* 2016; *Garambois et al.*, 2016].

2.2. AirSWOT

The AirSWOT payload comprises a multi-baseline Ka-band InSAR, a state-of-the-art inertial measurement unit (Applianix 610), and a 3-band color infrared (CIR) camera [http://cirrus-designs.com/]. These sensors are operated from a NASA B200 aircraft typically at an altitude of 8,230 meters above sea level. AirSWOT's Ka-band InSAR has multiple temporal and cross-track baselines in order to characterize the scattering and statistics expected from the primary instrument on SWOT (the Ka-band Radar Interferometer, or KaRIN [*Enjolras and Rodriguez*, 2009; *Biancamaria et al.*, 2016b]), provide data for developing classification algorithms, and improve the understanding of the instrument performance and limitations over the large variety of landscape conditions that SWOT will observe (i.e. sea ice, water obscured by vegetation, frozen or partially frozen rivers, etc). AirSWOT is designed with high-accuracy

elevation mapping capabilities and a swath mode that enables mapping of entire river networks in a reasonable timeframe. Further description of system parameters and calibration/validation requirements of AirSWOT's InSAR are presented by *Moller et al.,* [2011].

It is important to note the difference between the two separate observation swaths collected by the AirSWOT Ka-band InSAR. The inner swath has incidence angles ranging from 0-6 degrees, which fully encompasses KaRIN incidence angles of 0.6-3.9 degrees [*Fjørtoft et al.*, 2014], while the outer swath has incidence angles ranging from 4-25 degrees. When data is collected from ~8,200 meters, the inner swath is approximately 800 m in width, while the outer swath covers ~4 km. In this paper, we exclusively assess data from the wider outer swath because robust methods have not yet been developed to process data from the inner swath. Differences in incidence angles and viewing geometry render AirSWOT's observations substantially different from anticipated SWOT observations. While the random elevation errors of AirSWOT's outer swath should be smaller than what could be achieved by SWOT [*Fu et al.*, 2012], the SWOT platform will have superior stability compared to AirSWOT and SWOT incidence angles will likely produce better signal-to-noise ratios compared to AirSWOT's outer swath. Nonetheless, because AirSWOT's outer swath is designed to produce highly accurate WSE measurements it is likely to be useful for validating SWOT WSE measurements.

In preparation for the SWOT mission, the scientific community has identified WSE and slope accuracies needed for executing robust science of global surface water dynamics, which we use as a baseline to assess AirSWOT's performance and suitability as a validation instrument and its capabilities to provide useful hydraulic measurements in its own right. These accuracies are ±10 cm or better for WSEs when averaged over 1 km^2 areas and ±1.7 cm/km for slopes after processing along a maximum of 10 km of flow distance [*Biancamaria et al.*, 2016b; *Rodriguez*,

2016]. Primary sources of error for AirSWOT likely include layover from high topography and vegetation, random noise, and elements of the processing methodology such as the estimation of ambiguity height in phase unwrapping [*Rosen et al.*, 2000].

2.3. Study Site

For this study, we chose a ~90 km reach of the Tanana River, Alaska, bounded by two USGS gauge stations in the towns of Fairbanks and Nenana (Figure 2.1). This site is ideal for assessment of AirSWOT's capabilities to measure WSEs and slopes over a highly-dynamic, multi-channel river. The shape of the annual hydrograph on the Tanana is dominated by melt of snowpack and glaciers during the spring and summer. Mean annual discharge for the open-water season (May to October) at the gauge at Nenana (station 15515500) from 1962 to 2015 is ~1299 m^3/s. The mean daily discharge on June 9, 2015 was 835 m^3/s, which is extremely low for that day of the year. For comparison, average discharge on June 9th from 1962 to 2015 is ~1220 m^3/s. The glacial origin of the Tanana River results in a high sediment load, which interacts with local topography to produce a complex morphology that ranges from highly braided to a single meandering channel [*Brabets et al.*, 2000]. This varied river morphology, in combination with ubiquitous sandbars and high bluffs (20-50 m high) along the study reach, makes this a challenging test site for AirSWOT's InSAR technology.

2.4. Methods

2.4.1. Field Methods

We conducted a six-week field campaign from May 15, 2015 to June 27, 2015 to measure key hydrologic variables using *in situ* and AirSWOT measurements along the Tanana River, AK (Figure 2.1). This paper's focus is on the June 9, 2015 AirSWOT data collection, which is currently the only date for which AirSWOT radar data has been fully processed, though

we also use optical data from June 17, 2015 due to thin clouds present during the June 9th data collection. To assess AirSWOT's ability to measure river slopes and WSEs, we produced a high-resolution profile of WSEs. We used a Trimble R9 survey-grade GPS system attached to the back of a 28-foot river boat to measure WSEs nearly continuously (0.5 second intervals; ~3 m spacing) along the main channel of the river on June 7, 2015 (Figure 2.1). In total, we collected 26,827 WSE measurements. *In situ* measurements were infeasible on June 9th due to logistical constraints, but hydraulic conditions were very similar between the two dates aside from a small decline in stage. Between June 7th and June 9th, stage dropped 12 cm at Fairbanks and 17 cm at Nenana, resulting in a 0.05 cm/km difference in average slope between the two dates (24.80 cm/km on June 7th vs. 24.85 cm/km on June 9th).

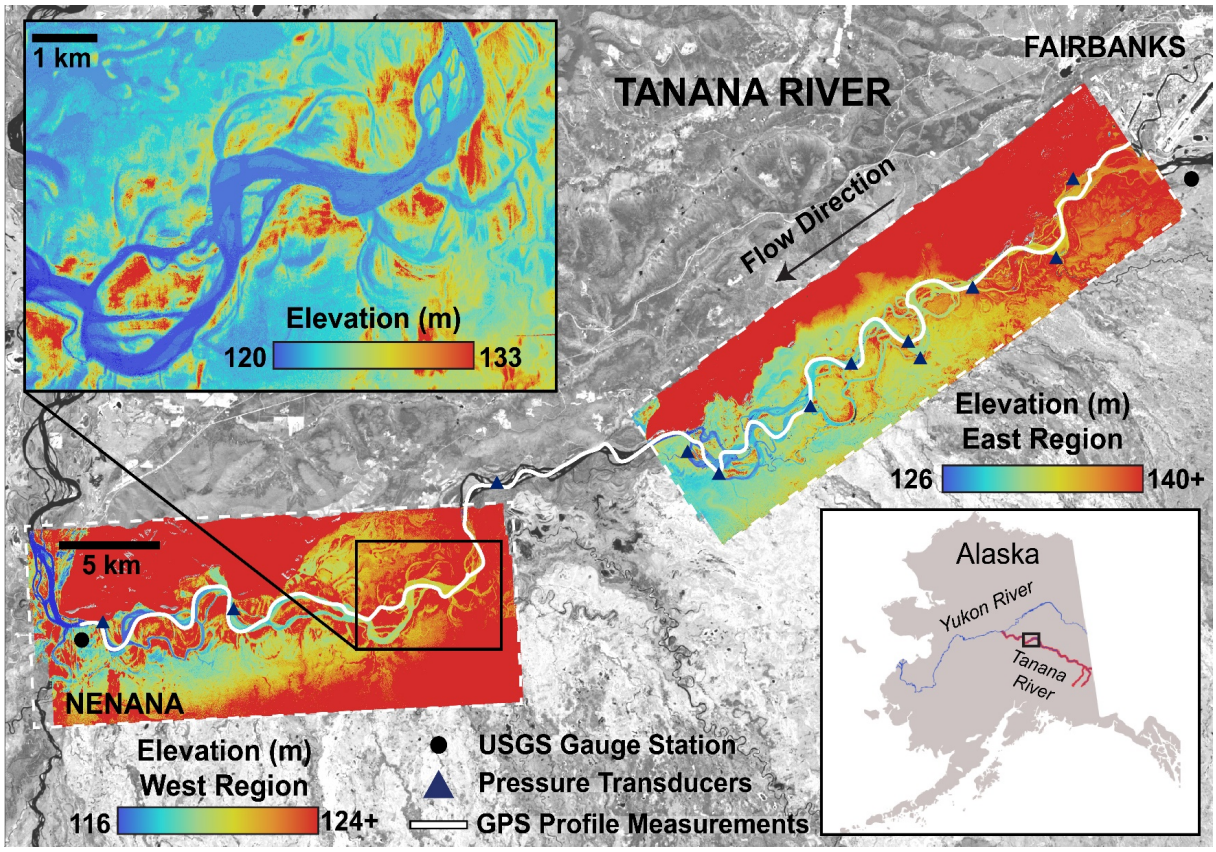

Figure 2.1: Location of the Tanana River study reach shown using a Landsat 8 near-infrared image acquired on 6/18/2013. AirSWOT elevation measurements and extent from June 9, 2015 are shown in the white dashed boxes.

In addition to the GPS profile measurements of WSE, we installed a network of 20 Solinst Levelogger pressure transducers throughout the study reach to record temporal variations in stage every two-minutes. Reported accuracy for the pressure transducers at a maximum depth of 10 m is ±1 cm [*http://www.solinst.com/products/dataloggers-and-telemetry/*]. Eight of the 20 transducers are not considered here due to the instruments shifting or being buried by mobile sediment or collapsed riverbanks. This left 12 transducers available for analysis (Figure 2.1). We used static GPS surveys to convert the transducer stage values to WSEs by measuring the height difference between the water surface and the GPS-surveyed benchmarks using an optical survey level. The pressure transducers recorded similar declines in stage between June 7th and

June 9th compared to the USGS gauge measurements. Of the 12 transducers with viable stage measurements, eight were located on the main channel where the GPS profile measurements were taken. Changes in stage at the transducers located on the same channel as the GPS profile ranged from -15 cm to -20 cm, with an average difference of -17.8 cm and an average slope difference of 0.02 cm/km (23.98 cm/km on June 7th vs. 24.00 cm/km on June 9th). Differences between slopes across the entire study reach calculated using the USGS gauge stations and transducer sites are quite small (< 0.05 cm/km) when compared to the reach average slope of ~24 cm/km. As a result, we subtracted the average stage difference calculated from the pressure transducers (-17.8 cm) from the June 7th profile observations to produce an estimated profile for June 9th that we compare to the AirSWOT measurements.

To achieve centimetric accuracies for the *in situ* WSE measurements, we used Natural Resources Canada's Canadian Geodetic Survey Precise Point Positioning tool (CSRS-PPP) for kinematic post-processing of the GPS profile measurements and static post-processing of GPS surveys conducted at the transducer sites [*http://www.nrcan.gc.ca/earth-sciences/geomatics/geodetic-reference-systems/*]. Vertical error estimates are not provided when processing kinematic measurements, so we estimated the random error for the profile elevations by applying a Gaussian filter to the profile and calculating the root mean squared error (RMSE) between the raw measurements and smoothed profile. We chose a window of 100 points, which produces a smoothed profile that preserves sub-kilometer scale features but eliminates noise. Larger smoothing windows result in convolution of signal (i.e. actual variations in WSE) with error and were thus avoided. RMSE between the smoothed profile and raw profile measurements is 2 cm, which is small compared to the anticipated AirSWOT measurement error. Elevation accuracies from the GPS surveys conducted at the transducer sites used to shift the

profile are ±3.6 to ±6.4 cm. Given the combined pressure transducer instrument and survey errors (±1.5 cm), total uncertainty for the GPS profile increases to ±9.9 cm.

The AirSWOT flight on June 9, 2015 began at 7:52 AM and ended at 10:30 AM. AirSWOT collected 21 swaths of elevation data; 9 swaths along a 43 km east region and 12 swaths along a 32 km west region of the study area (Figure 2.1). The CIR camera onboard the AirSWOT platform collected 1.16 m resolution optical photographs for each AirSWOT flight. Accurate location and orientation (latitude, longitude, altitude, roll, pitch, heading) of the CIR camera at the instant of each image acquisition were obtained using the AirSWOT platform Applanix GPS/IMU. Imagery was geo-rectified and processed into ortho-mosaics using Agisoft PhotoScan software [*http://www.agisoft.com/*].

2.4.2. Remote Sensing Methods

The AirSWOT team at the NASA Jet Propulsion Laboratory (JPL), which processes the AirSWOT radar data, provided several data products for each AirSWOT line, all stored in flat binary files on regular grids. Data products used in this study include elevation in meters above the WGS84 ellipsoid, magnitude of the relative backscatter received by the sensor measured in decibels (dB), and estimated elevation error. Elevation errors are estimated from the phase variance (Cramer-Rao bound) which depends on the coherence between the two interferometric images [*Rosen et al.*, 2000]. Spatial resolution is 3.6 m for all binary files.

To extract WSEs from the radar imagery, we create a water mask from AirSWOT optical imagery using a binary threshold of 0.30 in the Normalized Difference Water Index (NDWI) transformation [*McFeeters*, 1996] (Figure 2.2). Due to cloudy conditions on June 9th, we use optical imagery from June 17th to create the water mask. Water levels on June 17th were lower than those on June 9th (-22 cm), reducing the likelihood of land elevations being captured in the

water mask but potentially resulting in the exclusion of some area inundated on June 9th. We multiply the AirSWOT elevation images by the optical water mask, which removes land pixels from analysis (Figure 2.3). There is potential for the chosen binary threshold to misclassify some land pixels as water in the mask, which would introduce error into the AirSWOT WSE images. Errors resulting from misclassified water/land pixels are likely minimal since water levels were slightly lower on the date used to create the water mask, and visual inspection of the water mask shows good agreement of water/land boundaries.

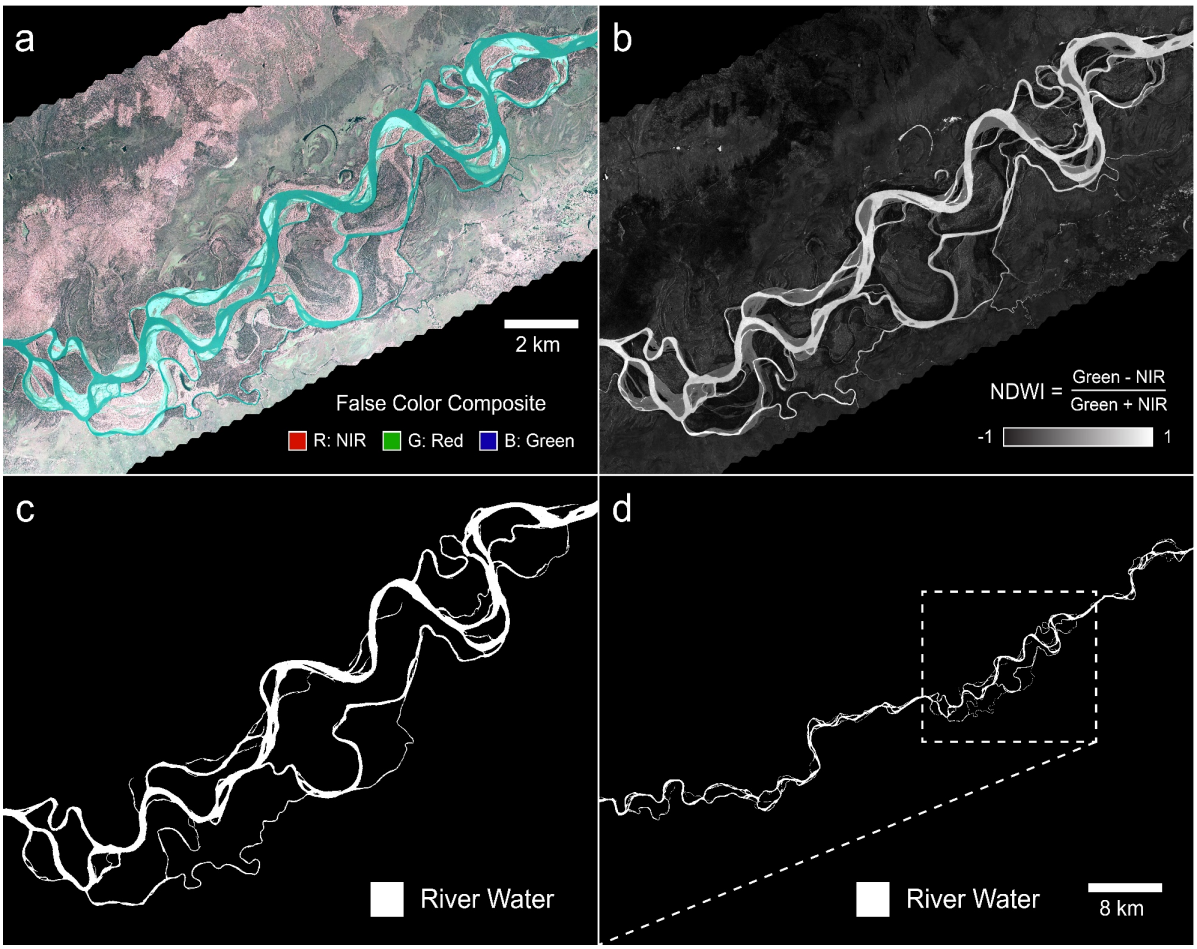

Figure 2.2: Derivation of the water mask used for the Tanana River study area. (a) False color composite of the color infrared (CIR) imagery acquired on 06/17/15. (b) Normalized Difference Water Index (NDWI) transformation of the CIR imagery. A threshold of 0.30 was used to differentiate water pixels from land pixels. (c) Binary water mask where water equals one (white area) and all land pixels equal zero (black area). (d) Final water mask across the entire Tanana River study reach.

We apply a two stage filtering process to refine the AirSWOT WSEs before comparing them to the field measurements (Figure 2.3). First, we use a ratio of magnitude divided by elevation error and exclude WSE pixels with ratios ≤5 dB of magnitude per meter of error. This threshold removes WSE pixels that are likely affected by layover and enforces stricter error limits on lower magnitude values. Since the magnitude decreases inside the swath, this method allows us to have a range-dependent threshold for the errors. Next, we use a moving 2 km^2 window to reduce remaining outliers by removing WSE pixels that are ±3 standard deviations

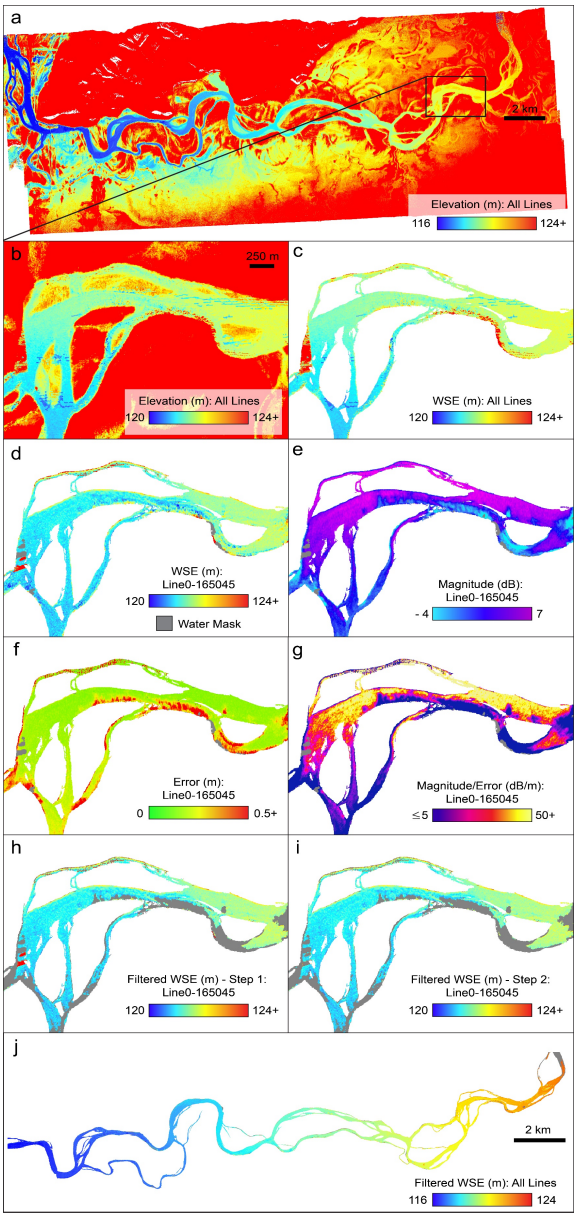

Figure 2.3: Methodology for filtering the AirSWOT elevations displayed using the west region. (a) Mosaic of all AirSWOT lines across the west region of the study area from 06/09/15. (b) Inset showing detailed AirSWOT elevations within the mosaic. (c) Before filtering the AirSWOT water surface elevations (WSEs), all flight lines are isolated using the water mask created using the CIR imagery acquired on 06/17/15 (Figure S1). (d) For each individual AirSWOT line, such as the example shown here, a ratio of (e) magnitude to (f) error is used to create a (g) fractional image, and (h) WSE pixels with fractions less than 5 dB/m are eliminated. This threshold removes WSE pixels that are likely affected by layover and enforces stricter error limits on lower magnitude values. Since the magnitude decreases inside the swath, this method allows us to have a range-dependent threshold for the errors. (i) Lastly, remaining outliers are removed by using a moving 2 km^2 window to identify pixels that are ±3 standard deviations away from the mean elevation within the window. (j) The filtered elevations for all lines are used to estimate AirSWOT WSE and slope errors.

away from the mean AirSWOT-derived elevation within the window. The remaining outliers are likely caused by misclassified water/land pixels from the water mask and poor ambiguity rejections at incidence angles <5 degrees [*Goldstein et al.*, 1988]. On average, the filters eliminate 65% of the original WSE pixels in the east region and 39% of the original WSE pixels in the west region. When compared to the observed water mask area, the filtered elevations retain 84% of the water surface area in the east region and 95% of the water surface area in the west region due to overlap of AirSWOT measurement swaths. The filters eliminate more water pixels and area in the east region due to higher error values and lower magnitudes likely resulting from a combination of high adjacent topography and more complex channel morphology.

To determine AirSWOT WSE and slope errors, we compare the filtered AirSWOT WSEs to the GPS profile measurements. First, we calculate a mean AirSWOT elevation along a transect orthogonal to the GPS profile (Figure 2.4). We interpolate a 1 km orthogonal vector (±500 m) at each GPS profile measurement, extract the WSEs from the filtered AirSWOT images along this orthogonal, and average them together. Next, we segment the water mask in the downstream direction into 1 km^2 bins and average the AirSWOT WSEs and GPS profile measurements within each bin (Figure 2.4). We subtract the average AirSWOT WSEs from the average profile measurements in each bin to estimate the AirSWOT WSE error over 1 km^2 areas. We focus primarily on 1 km^2 bins because the SWOT science requirements are defined against this area, but we also test bin sizes ranging from 100 m^2 to 10 km^2. Finally, we calculate slopes from AirSWOT and GPS profile data using a moving 10 km window that advances down the profile every 100 m. For each 10 km reach, we calculate slopes for both AirSWOT orthogonal mean values and the GPS profile measurements using linear regressions, then subtract the AirSWOT slopes from the GPS profile slopes. To assess AirSWOT's ability to capture slope

variability, we compute Nash-Sutcliffe Efficiency (NSE) values of the AirSWOT slopes relative to the GPS-derived slopes for the east and west regions [*McCuen et al.*, 2006]. NSE values range from $-\infty$ to 1, with an NSE of 1 indicating that the GPS and AirSWOT slopes are identical and an NSE less than zero indicating that the mean GPS profile slope better characterizes slope variability than do the AirSWOT measurements. We also assess AirSWOT slope measurement capabilities along reach lengths ranging from 1-20 km using both RMSE and NSE.

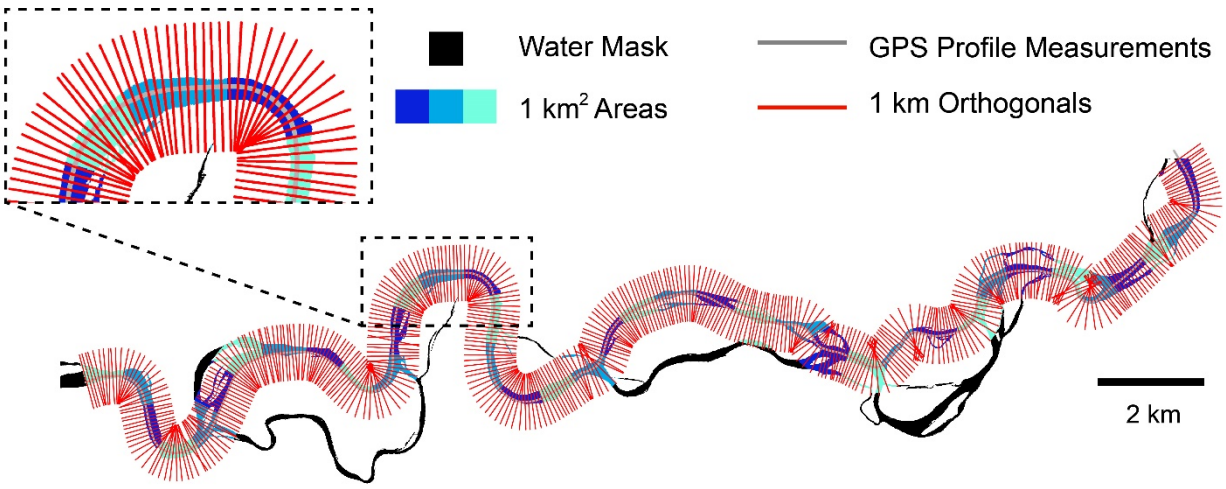

Figure 2.4: Methodology for averaging AirSWOT WSEs at the GPS profile measurements across orthogonal vectors and 1 km^2 areas. For visual clarity, one orthogonal vector is plotted for every 20 GPS transect points.

2.5. Results

Comparison of AirSWOT and *in situ* WSE profiles shows strong similarities between the measurements. Figure 2.5 shows the orthogonal means of AirSWOT WSEs and the GPS WSE profiles for the east (Figure 2.5a) and west (Figure 2.5b) regions. The majority (73%) of WSE errors within 1 km^2 regions fall below the science requirements defined by the SWOT mission of ±10 cm, with an RMSE of 9.0 cm and mean absolute error (MAE) of 7.1 cm (Figure 2.5c). Bias, at 0.65 cm, is a very small component of AirSWOT measurement error relative to *in situ* observations. The largest AirSWOT WSE deviations from the observations occur in the first 10

km of both the east and west regions. WSE errors vary with the size of the averaging bins, with higher errors at smaller bin sizes (Figure 2.6a). Given the uncertainty in the GPS profile measurements (±9.9 cm), observational uncertainty likely accounts for a substantial portion of the AirSWOT WSE errors.

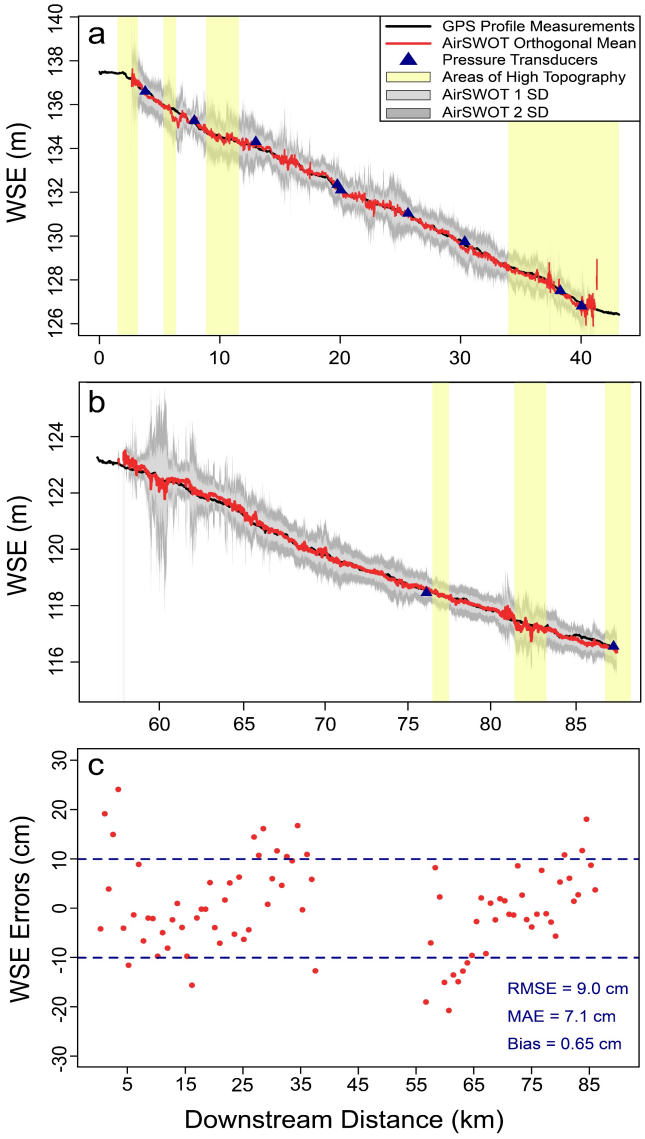

Figure 2.5: WSE profiles derived from GPS (black) and AirSWOT (red) for the (a) east and (b) west regions. Standard deviations (SD) are shown for the AirSWOT WSEs in the grey shaded areas. (c) Differences between GPS WSEs and AirSWOT WSEs averaged over 1 km^2 areas. Blue dashed lines mark the SWOT science requirement for WSE accuracies (±10 cm).

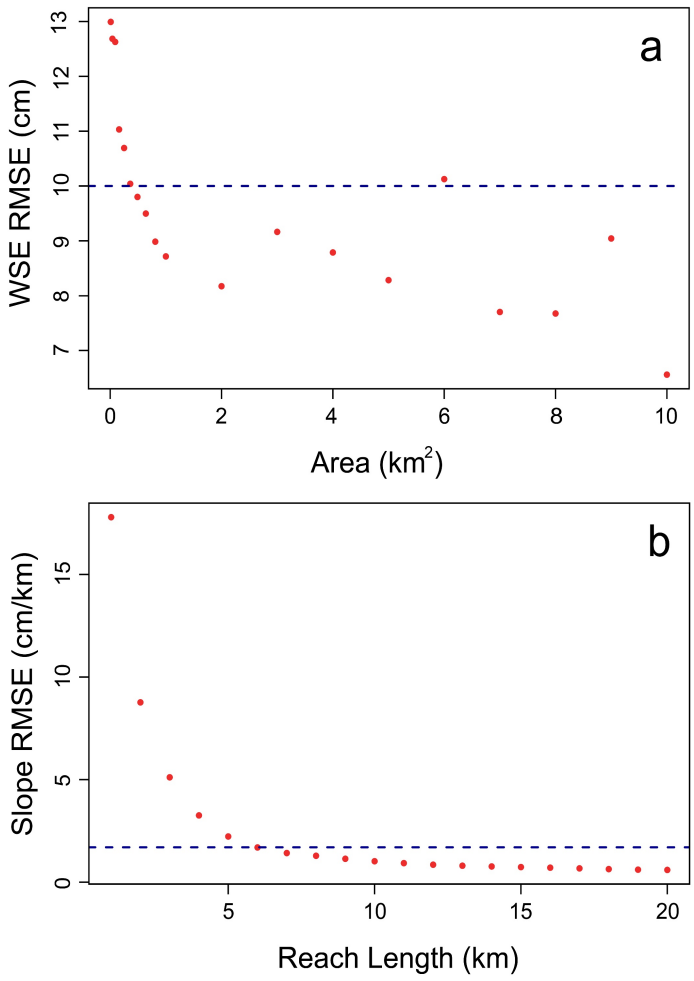

Figure 2.6: (a) Root mean squared error (RMSE) for AirSWOT WSEs versus the spatial area used to average the AirSWOT and *in situ* measurements. (b) RMSE for AirSWOT slopes versus the reach length used to calculate the AirSWOT and *in situ* slopes. Blue dashed lines indicate the SWOT science requirements of 10 cm of error across 1 km^2 areas for WSEs and 1.7 cm/km for slopes across 10 km reaches.

For 10 km reach lengths, AirSWOT is capable of accurately measuring slopes with an RMSE of 1.0 cm/km, as well as capturing detailed variations in slopes, with NSE values of 0.76 and 0.93 for the east and west regions, respectively. Figure 2.7 shows slopes along 10 km reaches for the east (Figure 2.7a) and west regions (Figure 2.7b). Out of 499 overlapping 10 km reaches (289 east and 210 west), 90% of slope errors are at or below the SWOT science requirements of ±1.7 cm/km (Figure 2.7c). Slope errors range from -2.4 cm/km to 2.2 cm/km,

with an RMSE of 1.0 cm/km and an MAE of 0.83 cm/km. Slope errors decline predictably with reach length, from 17.8 cm/km for 1 km reaches to 0.6 cm/km for 20 km reaches (Figure 2.6b). NSE values are generally lower for shorter reaches, though the increase is not monotonic with reach length (Figure 2.8). Slopes with errors greater than the SWOT science requirement are likely affected by topographic layover from high bluffs adjacent to the channel (Figure 2.5) and incorrect ambiguity heights. Ambiguity heights are used in InSAR processing to unwrap the interferometric phase, an important step in retrieving the elevations, and are sensitive to areas of high topography as well as aircraft pitch and roll [*Rosen et al.*, 2000]. Therefore, incorrect ambiguity heights may lead to large errors in elevation measurements. Additionally, some portion of the difference between the AirSWOT and GPS profile slopes could be attributable to slope changes that may have occurred between June 7th, when the *in situ* measurements were collected, and the June 9th AirSWOT flight.

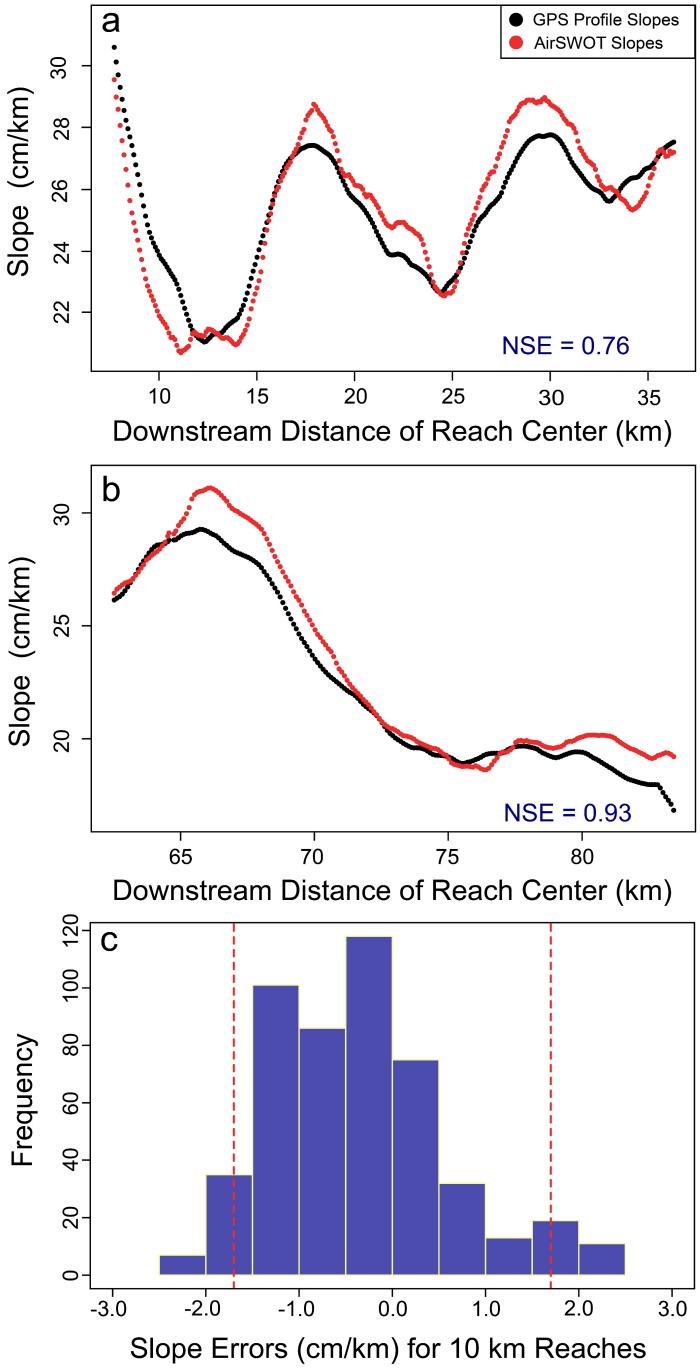

Figure 2.7: Slopes from GPS profile and AirSWOT for the 499 overlapping 10 km reaches within the (a) east and (b) west regions versus the center of each reach in order of downstream distance. Successive reach segments are shifted downstream by 100 m. c) Histogram of slope errors for AirSWOT slopes relative to GPS-derived measurements. Red dashed lines mark the SWOT science requirement for slope accuracies (±1.7 cm/km).

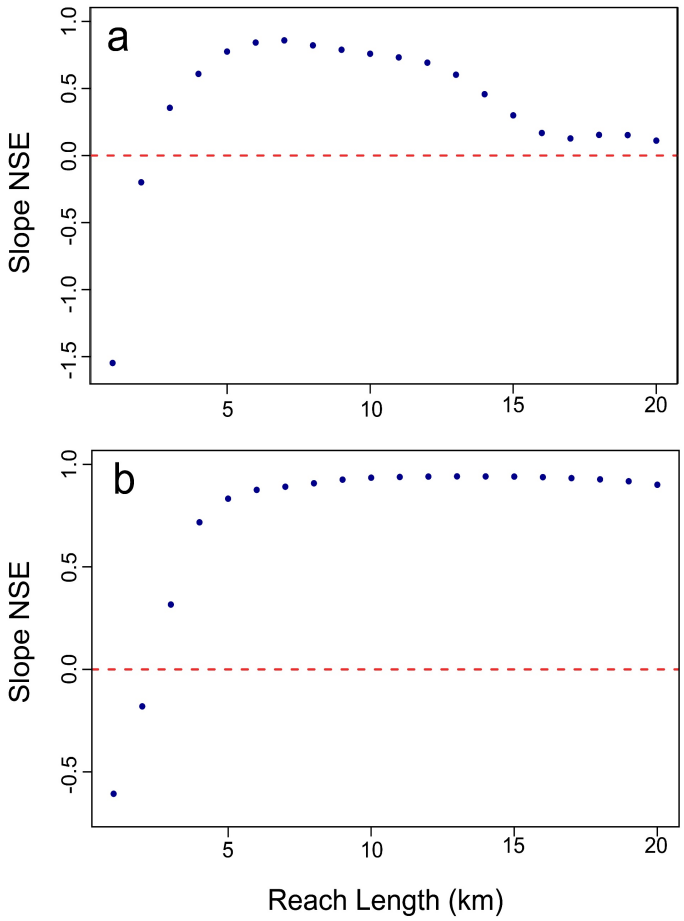

Figure 2.8: Nash-Sutcliffe Efficiency (NSE) values versus reach length used to calculate the AirSWOT and *in situ* measurement slopes for the (a) east and (b) west regions. NSE values above the red dashed lines indicate AirSWOT measurements are more capable of predicting slope variability than the mean slope of the *in situ* measurements.

2.6. Discussion

AirSWOT provides a new, robust method for measuring WSEs and slopes over considerable reach lengths without the need for *in situ* data. Results indicate that AirSWOT accuracies are high enough to capture decimeter-level variations in WSEs with estimated errors at or below 10 cm when averaged over areas ≥700 m^2 (Figures 2.5, 2.6a). We observe a mean bias in averaged AirSWOT WSEs of <1 cm without any intercalibration between *in situ* and

AirSWOT measurements. Furthermore, AirSWOT measurements are capable of capturing centimeter-per-kilometer level variations in slopes with an RMSE of 1.0 cm/km for 10 km reaches (Figure 2.7) and an RMSE as low 0.6 cm/km for 20 km reaches (Figure 2.6b). There are no previous airborne or satellite missions that, like AirSWOT, use short (Ka-band) wavelength radar measurements acquired at low incidence angles to measure rivers. As a result, while AirSWOT processing is similar to other InSAR methodologies, new procedures for handling the complexities arising during calibration remain under development and may account for some of the observed error. Despite current processing limitations, AirSWOT provides unprecedented remotely-sensed measurements of river WSE and slope even in a challenging river environment like the Tanana.

The impressive details observed by AirSWOT offer new opportunities to explore surface water hydrology. Future studies can use AirSWOT to characterize spatial controls on regional stream hydraulics at comparatively fine spatial and temporal resolutions. SWOT is expressly designed to observe surface water dynamics, but it will have significant gaps in spatial coverage, with 2-10 revisits per 21 day orbit cycle and will only observe rivers wider than 50-100 m [*Biancamaria et al.*, 2016b]. These characteristics limit SWOT observations of surface water fluxes to weekly and monthly timescales, which can miss the peaks and troughs of rapid hydrologic events. In contrast, AirSWOT can be tasked to take repeat measurements across hundreds of kilometers of river reaches at hourly or daily timescales. These measurements can be used to observe detailed passages of flood waves and provide estimates of WSE and slope variability between existing *in situ* gauges or altimeter measurements to help understand spatial controls on river hydraulics [*Garambois et al.*, 2016]. Additionally, AirSWOT's fine spatial resolution (<4 m) allows for better visibility in small river systems that play a non-negligible role

in the water and carbon cycles and are poorly gauged or not observable by satellites [*Raymond et al.,* 2013; *Biancamaria et al.,* 2016a]. AirSWOT measurements can be spatially averaged to get WSE and slope estimates in rivers with widths <50 m. AirSWOT measurements are also valuable for distributed hydrological analysis in highly multi-dimensional systems, such as braided rivers and deltas, where spatially-distributed *in situ* observations are difficult to attain and tidal effects require fine temporal resolution measurements [*Wolski et al.*, 2006; *Schubert et al.*, 2015].

AirSWOT measurements can be a powerful tool to enhance flood models. Hydrodynamic models suffer from a lack of spatially distributed calibration and validation data and are often constrained by point measurements of WSE from ground campaigns, altimeters, or gauge stations. These data constraints limit the capabilities of models by admitting many "optimal" parameter combinations during calibration [*Pappenberger et al.*, 2005; *Hunter et al.*, 2007; *Bates et al.*, 2013]. Scientists can use AirSWOT measurements to constrain model parameters over long reach distances and to improve understanding of the physical processes controlling the spatial distribution of model parameters [*Hall et al*., 2005; *Warmink et al.*, 2013]. AirSWOT measurements can also be used to validate models' abilities to reproduce spatial variations in slope across hundreds of kilometers and can be assimilated to improve model accuracies. Additionally, AirSWOT is capable of acquiring measurements in cloudy conditions and can be assigned to take measurements during critical hydraulic events (e. g. after a storm) to capture flood peaks and maximum inundation extents that are often missed by existing satellite sensors [*Biancamaria et al.*, 2016a]. These measurements can enable better model calibration and validation, allowing improved prediction of areas vulnerable to flooding.

Finally, these results support the use of AirSWOT as a future validation instrument for SWOT. The results of this study show that AirSWOT is capable of producing SWOT-quality or better measurements of river WSEs and slopes. Considering lower errors are expected at lower incidence angles, these errors are likely to decrease as processing methods advance and AirSWOT data at SWOT-like incidence angles can be included. In addition to SWOT validation, other ongoing projects are using AirSWOT data to help determine the effects on radar returns of specular water surfaces associated with low wind speeds, better quantify the frequency and extent of topographic layover effects, and assess returns from inundated vegetation [*Biancamaria et al.*, 2016b]. The results of this study present the first published demonstration of AirSWOT's ability to accurately measure WSEs and slopes and its promise as a future validation instrument for the SWOT mission. Future work should seek to validate AirSWOT's ability to measure 2D slopes in floodplain environments, to characterize AirSWOT's accuracy across a variety of river sizes and morphologies, and to understand AirSWOT's abilities to measure WSEs in lakes and wetlands.

REFERENCES

Alsdorf, D., P. Bates, J. Melack, M. Wilson, and T. Dunne (2007a), Spatial and temporal complexity of the Amazon flood measured from space, *Geophys. Res. Lett.*, *34*(8), L08402, doi:10.1029/2007GL029447.

Alsdorf, D. E., E. Rodríguez, and D. P. Lettenmaier (2007b), Measuring surface water from space, *Rev. Geophys.*, *45*(2), RG2002, doi:10.1029/2006RG000197.

Bates, P. D. (2012), Integrating remote sensing data with flood inundation models: how far have we got?, *Hydrol. Process.*, *26*(16), 2515–2521, doi:10.1002/hyp.9374.

Bates, P. D., F. Pappenberger, R. J. Romanowicz (2013), Uncertainty in Flood Inundation Modelling. Applied uncertainty analysis for flood risk management, K. Beven, J. Hall (eds). *Imperial College Press: Singapore*, 232–269.

Bates, P. D., J. C. Neal, D. Alsdorf, and G. J. P. Schumann (2014), Observing Global Surface Water Flood Dynamics, *Surv. Geophys.*, *35*(3), 839–852, doi:10.1007/s10712-013-9269-4.

Biancamaria, S., F. Frappart, A. S. Leleu, V. Marieu, D. Blumstein, J. D. Desjonquères, F. Boy, A. Sottolichio, and A. Valle-Levinson (2016a), Satellite radar altimetry water elevations performance over a 200m wide river: Evaluation over the Garonne River, *Adv. Sp. Res.*, doi:10.1016/j.asr.2016.10.008.

Biancamaria, S., D. P. Lettenmaier, and T. M. Pavelsky (2016b), The SWOT mission and its capabilities for land hydrology, *Surv. Geophys.*, *37*(2), 307–337, doi:10.1007/s10712-015-9346-y.

Brabets, T. P., B. Wang, and R. H. Meade (2000), Environmental and hydrologic overview of the Yukon River Basin, Alaska and Canada, *US Dep. Inter. US Geol. Surv.*

Calmant, S., F. Seyler, and J. F. Cretaux (2008), Monitoring continental surface waters by satellite altimetry, *Surv. Geophys.*, *29*(4-5), 247–269, doi:10.1007/s10712-008-9051-1.

Clark, E. A., J. Sheffield, M. T. H. van Vliet, B. Nijssen, and D. P. Lettenmaier (2015), Continental runoff into the oceans (1950–2008), *J. Hydrometeorol.*, *16*(4), 1502–1520, doi:10.1175/JHM-D-14-0183.1.

Di Baldassarre, G., and S. Uhlenbrook (2012), Is the current flood of data enough? A treatise on research needs for the improvement of flood modelling, *Hydrol. Process.*, *26*(1), 153–158, doi:10.1002/hyp.8226.

Durand, M., C. J. Gleason, P. A. Garambois, D. Bjerklie, L. C. Smith, H. Roux, E. Rodriguez, P. D. Bates, T. M. Pavelsky, J. Monnier, X. Chen, G. Di Baldassarre, J. M. Fiset, N. Flipo, R. P. D. M. Frasson, J. Fulton, N. Goutal, F. Hossain, E. Humphries, J. T. Minear, M. M. Mukolwe, J. C. Neal, S. Ricci, B. F. Sanders, and G. J. P. Schumann (2016). An

intercomparison of remote sensing river discharge estimation algorithms from measurements of river height, width, and slope. *Water Resour. Res.*, doi:10.1002/2015WR018434.

Enjolras, V. M., and E. Rodriguez (2009). An assessment of a Ka-band radar interferometer mission accuracy over Eurasian Rivers. *IEEE Transactions on Geoscience and Remote Sensing*, *47*(6), 1752-1765, doi:10.1109/TGRS.2008.2006370.

Famiglietti, J. S., and M. Rodell (2013), Water in the balance, *Science*, 340(6138), 1300–1301, doi:10.1126/science.1236460.

Fjørtoft, R., J. M. Gaudin, N. Pourthié, J. C. Lalaurie, A. Mallet, J. F. Nouvel, J. Martinot-Lagarde, H. Oriot, P. Borderies, C. Ruiz, and S. Daniel (2014), KaRIn on SWOT: characteristics of near-nadir Ka-band interferometric SAR imagery, *IEEE Trans. Geosci. Remote Sens.*, *52*(4), 2172–2185, doi:10.1109/TGRS.2013.2258402.

Fu L. L., D. E. Alsdorf, R. Morrow, E. Rodriguez, N. M. Mognard (2012) SWOT: the Surface Water and Ocean Topography mission. *JPL Publication 12 05*, http://swot.jpl.nasa.gov/files/swot/SWOT_MSD_1202012.pdf.

Garambois, P. A., S. Calmant, H. Roux, A. Paris, J. Monnier, P. Finaud-Guyot, A. Montazem, J. Santos da Silva (2016), Hydraulic visibility : using satellite altimetry to parameterize a hydraulic model of an ungauged reach of a braided river, *Hydrol. Process.*, 1–20, doi:10.1002/hyp.11033.

Goldstein, R. M., H. A. Zebker, and C. L. Werner (1988), Satellite radar interferometry: Two-dimensional phase unwrapping, *Radio Sci.*, *23*(4), 713–720, doi:10.1029/RS023i004p00713.

Hall, J. W., S. Tarantola, P. D. Bates, and M. S. Horritt, (2005). Distributed sensitivity analysis of flood inundation model calibration. *Journal of Hydraulic Engineering*, *131*(2), 117-126, doi: 10.1061/(ASCE)0733-9429(2005)131:2(117), 117-126.

Hannah, D. M., S. Demuth, H. A. J. van Lanen, U. Looser, C. Prudhomme, G. Rees, K. Stahl, and L. M. Tallaksen (2011), Large-scale river flow archives: importance, current status and future needs, *Hydrol. Process.*, *25*(7), 1191–1200, doi:10.1002/hyp.7794.

Hunter, N. M., P. D. Bates, M. S. Horritt, and M. D. Wilson (2007), Simple spatially-distributed models for predicting flood inundation: a review, *Geomorphology*, *90*(3-4), 208–225, doi:10.1016/j.geomorph.2006.10.021.

Marcus, W. A., and M. A. Fonstad (2008), Optical remote mapping of rivers at sub-meter resolutions and watershed extents, *Earth Surf. Process. Landforms*, 33(1), 4–24, doi:10.1002/esp.

McCuen, R. H., Z. Knight, and A. G. Cutter (2006), Evaluation of the Nash–Sutcliffe efficiency

Index, *J. Hydrol. Eng.*, *11*(6), 597–602, doi:10.1061/(ASCE)1084-0699(2006)11:6(597).

McFeeters, S. K. (1996), The use of the Normalized Difference Water Index (NDWI) in the delineation of open water features, *Int. J. Remote Sens.*, *17*(7), 1425–1432, doi:10.1080/01431169608948714.

Moller, D., E. Rodriguez, J. Carswell, and D. Esteban-Fernandez (2011). AirSWOT-A calibration/validation platform for the SWOT mission, *Proc. Interntational Geoscience and Remote Sensing Symposium, Vancouver, Canada.*

O'Loughlin, F., M. A. Trigg, G. J. P. Schumann, and P. D. Bates (2013), Hydraulic characterization of the middle reach of the Congo River, *Water Resour. Res.*, *49*(8), 5059–5070, doi:10.1002/wrcr.20398.

O'Loughlin, F. E., J. Neal, D. Yamazaki, and P. D. Bates (2016), ICESat-derived inland water surface spot heights, *Water Resour. Res.*, 52(4), 3276-3284, doi:10.1002/2014WR015716.

Pappenberger, F., K. Beven, M. Horritt, and S. Blazkova (2005), Uncertainty in the calibration of effective roughness parameters in HEC-RAS using inundation and downstream level observations, *J. Hydrol.*, *302*(1-4), 46–69, doi:10.1016/j.jhydrol.2004.06.036.

Paris, A., R. C. Paiva, J. S. Silva, D. M. Moreira, S. Calmant, P. A. Garambois, W. Collischonn, M. P. Bonnet, and F. Seyler (2016), Stage-discharge rating curves based on satellite altimetry and modeled discharge in the Amazon basin, *Water Resour. Res.*, doi:10.1002/2014WR015716.

Pavelsky, T. M., M. T. Durand, K. M. Andreadis, R. E. Beighley, R. C. Paiva, G. H. Allen, and Z. F. Miller (2014), Assessing the potential global extent of SWOT river discharge observations, *J. Hydrol.*, *519*, 1516–1525, doi:10.1016/j.jhydrol.2014.08.044.

Raymond, P. A., J. Hartmann, R. Lauerwald, S. Sobek, C. McDonald, M. Hoover, D. Butman, R. Striegl, E. Mayorga, C. Humborg, P. Kortelainen, H. Dürr, M. Meybeck, P. Ciais, and P. Guth (2013). Global carbon dioxide emissions from inland waters. *Nature*, *503*(7476), 355-359, doi:10.1038/nature12760.

Rodell, M., H. K. Beaudoing, T. S. L'Ecuyer, W. S. Olson, J. S. Famiglietti, P. R. Houser, R. Adler, M. G. Bosilovich, C. A. Clayson, D. Chambers, E. Clark, E. J. Fetzer, X. Gao, G. Gu, K. Hilburn, G. J. Huffman, D. P. Lettenmaier, W. T. Liu, F. R. Robertson, C. A. Schlosser, J. Sheffield, and E. F. Wood (2015), The observed state of the water cycle in the early twenty-first century, *J. Clim.*, *28*(21), 8289–8318, doi:10.1175/JCLI-D-14-00555.1.

Rodriguez, E. (2016), Surface Water and Ocean Topography Mission (SWOT). *Science requirements Document V1*, 1.

Rosen, P. A., S. Hensley, I. R. Joughin, F. K. Li, S. N. Madsen, E. Rodriguez, and R. M.

Goldstein (2000), Synthetic aperture radar interferometry, *Proc. IEEE*, *88*(3), 333–382, doi:10.1088/0266-5611/14/4/001.

Schubert, J. E., W. W. Monsen, and B. F. Sanders (2015), Metric-Resolution 2D River Modeling at the Macroscale: Computational Methods and Applications in a Braided River, *Front. Earth Sci.*, 3, 74, doi:10.3389/feart.2015.00074.

Schumann, G. J. P., P. D. Bates, M. S. Horritt, P. Matgen, and F. Pappenberger (2009), Progress in integration of remote sensing - derived flood extent and stage data and hydraulic models, *Rev. Geophys.*, 47(4), doi:10.1029/2008RG000274.

Smith, L. C. (1997), Satellite remote sensing of river inundation area, stage, and discharge: A review, *Hydrol. Process.*, 11(10), 1427–1439, doi: 10.1002/(SICI)1099-1085(199708)11:10<1427::AID-HYP473>3.3.CO;2-J.

Warmink, J. J., M. J. Booij, H. Van der Klis, and S. J. M. H. Hulscher (2013), Quantification of uncertainty in design water levels due to uncertain bed form roughness in the Dutch river Waal, *Hydrol. Process.*, *27*(11), 1646–1663, doi:10.1002/hyp.9319.

Wolski, P., H. H. G. Savenije, M. Murray-Hudson, and T. Gumbricht (2006), Modelling of the flooding in the Okavango Delta, Botswana, using a hybrid reservoir-GIS model, *J. Hydrol.*, *331*(1), 58–72, doi:10.1016/j.jhydrol.2006.04.040.

CHAPTER 3: HIGH-PRECISION RIVER HEIGHT AND SLOPE CHANGES CAPTURED BY AIRSWOT

3.1 Introduction

The recent, rapid expansion of remote sensing technology provides exciting opportunities to address global-scale questions regarding river processes, especially in areas where *in situ* stream gauges are declining or do not exist [*Hannah et al.*, 2011; *Pavelsky et al.*, 2014]. Currently, the most robust method for remotely observing river heights and slopes is satellite altimetry [*Calmant et al.*, 2008; *Bates et al.*, 2014; *Tourian et al.*, 2016]. There have been many studies using available altimeters to measure surface water heights with accuracies ranging from 10 cm (ICESat, SARAL/Altika) to several decimeters (TOPEX/Poseidon, Jason-2, Envisat) [*Calmant et al.*, 2008; *O'Loughlin et al.*, 2016]. These altimeter measurements have been used to validate flood models, create time series of water level changes, estimate discharge, and quantify river height and slope variability in hard-to-reach river basins [*Kouraev et al.*, 2004; *Papa et al.*, 2010; *Domeneghetti*, 2016; *Garambois et al.*, 2016; *Paris et al.*, 2016; *Tourian et al.*, 2016]. However, altimeter missions and their processing chains were primarily developed to view ocean processes. As a result, altimeter observations have low temporal (10-35 days) and spatial (70-600 m) resolutions, as well as complex error characteristics due to variable waveforms, height changes along rivers and lakes, surrounding land elevations, and specular reflections [*Alsdorf et al.*, 2007; *Calmant et al.*, 2008]. These characteristics limit the hydraulic visibility of altimeters to the world's largest river systems [*Smith*, 1997; *Alsdorf et al.*, 2007; *Calmant et al.*, 2008; *Maillard et al.*, 2015; *Garambois et al.*, 2016].

The upcoming Surface Water and Ocean Topography (SWOT) mission plans to vastly increase global observations of rivers ≥100 m wide by providing simultaneous, 2D measurements of surface water elevations from ~78°N to ~78°S [*Fjørtoft et al.*, 2014; *Biancamaria et al.*, 2016]. SWOT's goal is to measure river heights and slopes with accuracies of 10 cm when averaged over 1 km^2 areas and 1.7 cm/km along 10 km reaches [*Rodriguez*, 2016]. As part of the SWOT mission, NASA has developed AirSWOT, an airborne analogue to SWOT [*Fu et al.*, 2015; *Biancamaria et al.*, 2016; *Altenau et al.*, 2017a]. AirSWOT is designed to measure high-accuracy elevations in a ~5 km wide swath that enables mapping of hundreds of kilometers of river reaches in a reasonable timeframe, and at substantially higher resolution than what SWOT will provide. There are significant differences between AirSWOT's incidence angles and viewing geometry and those of the anticipated SWOT observations. However, AirSWOT provides comparable measurements to SWOT by recording elevations at the same radar wavelength (Ka-Band) and at narrower incidence angles (0.5-30°) than existing sensors. More detailed summaries of the differences between AirSWOT and SWOT, along with AirSWOT's capabilities, are presented by *Moller et al.* [2011] and *Altenau et al.* [2017a].

Previous work has shown, that for a single day, AirSWOT can capture detailed spatial variations in river profiles and slopes with accuracies of 9.0 cm over 1 km^2 areas and 1.0 cm/km over 10 km reaches [*Altenau et al.*, 2017a]. These results demonstrate AirSWOT is capable of measuring SWOT hydrology variables within the mission error requirements, and is useful for understanding river hydraulics at scales that will be unobservable by SWOT [*Altenau et al.*, 2017a]. To date, however, the ability of AirSWOT to accurately measure multi-temporal variations in river heights and slopes remains uncertain.

For the first time, we present analysis demonstrating the ability of AirSWOT to record river height and slope changes between six different AirSWOT collections acquired over the course of three weeks. Furthermore, we investigate the potential of AirSWOT measurements for deducing other hydraulic quantities by comparing discharge estimates calculated from AirSWOT heights and slopes to discharge estimates from *in situ* observations. Changes in river heights and slope are imperative for characterizing hydraulic controls, which are important for monitoring changes in freshwater resources, flood risk, and ecological health [*Puckridge et al.*, 1998; *Schumm*, 2007].

3.2. Methods

3.2.1 Field Measurements

To validate AirSWOT measurements of river height and slope, we conducted a six-week field campaign from May 15, 2015 to June 27, 2015 along a ~90 km reach of the Tanana River, AK (Figure 3.1a). We chose this study reach due to its complex morphology, high surrounding topography, and boreal location, which are all challenging factors to test the capabilities of AirSWOT [*Altenau et al.,* 2017a]. We installed a network of 20 Solinst M5 Levelogger Edge pressure transducers (PTs) throughout the study reach to record high-resolution, *in situ* measurements of changes in river height as well as two Solinst Barologgers to compensate for atmospheric pressure fluctuations [*https://www.solinst.com/products/data/3001.pdf*]. Eight of the 20 pressure transducers are not used in this study because they were buried by mobile sediment or riverbanks after installation as a result of fluvial geomorphological processes. This left us with 12 viable pressure transducers to calculate river height and slope changes (Figure 3.1a). The distance between pressure transducers ranges from 0.29-23 km, with the majority of the pressure transducers spaced 4-8 km apart. We set the pressure transducers to record at 2 min intervals.

Reported accuracy for the Leveloggers is ±0.3 cm and Barologgers is ±0.05 kPa (0.5 cm), resulting in a combined instrument accuracy for water level measurements of ±0.8 cm [*https://www.solinst.com/products/data/3001.pdf*].

To convert the water level measurements to river heights, we used an optical survey level to measure the height difference between the water surface and GPS benchmark sites located at each pressure transducer location. We used Natural Resources Canada's Canadian Geodetic Survey Precise Point Positioning tool for static post processing of the GPS surveys, providing us centimeter-level accuracies on the absolute heights at each pressure transducer site [*http://www.nrcan.gc.ca/earth-sciences/geomatics/geodetic-reference-systems/*]. The accuracy of the GPS surveys ranges from ±3.6-6.3 cm, while our optical survey accuracy is ±0.2 cm, bringing the total uncertainty for the pressure transducers to ±4.6-7.3 cm. It is also possible that the pressure transducers experienced some shifting or sinking due to the high mobility of the Tanana River bed [*Brabets et al.*, 2000]. Any potential movements would add to the uncertainty in the pressure transducer heights. However, we did not have robust methods for measuring these effects, therefore they are not accounted for in our uncertainty calculations.

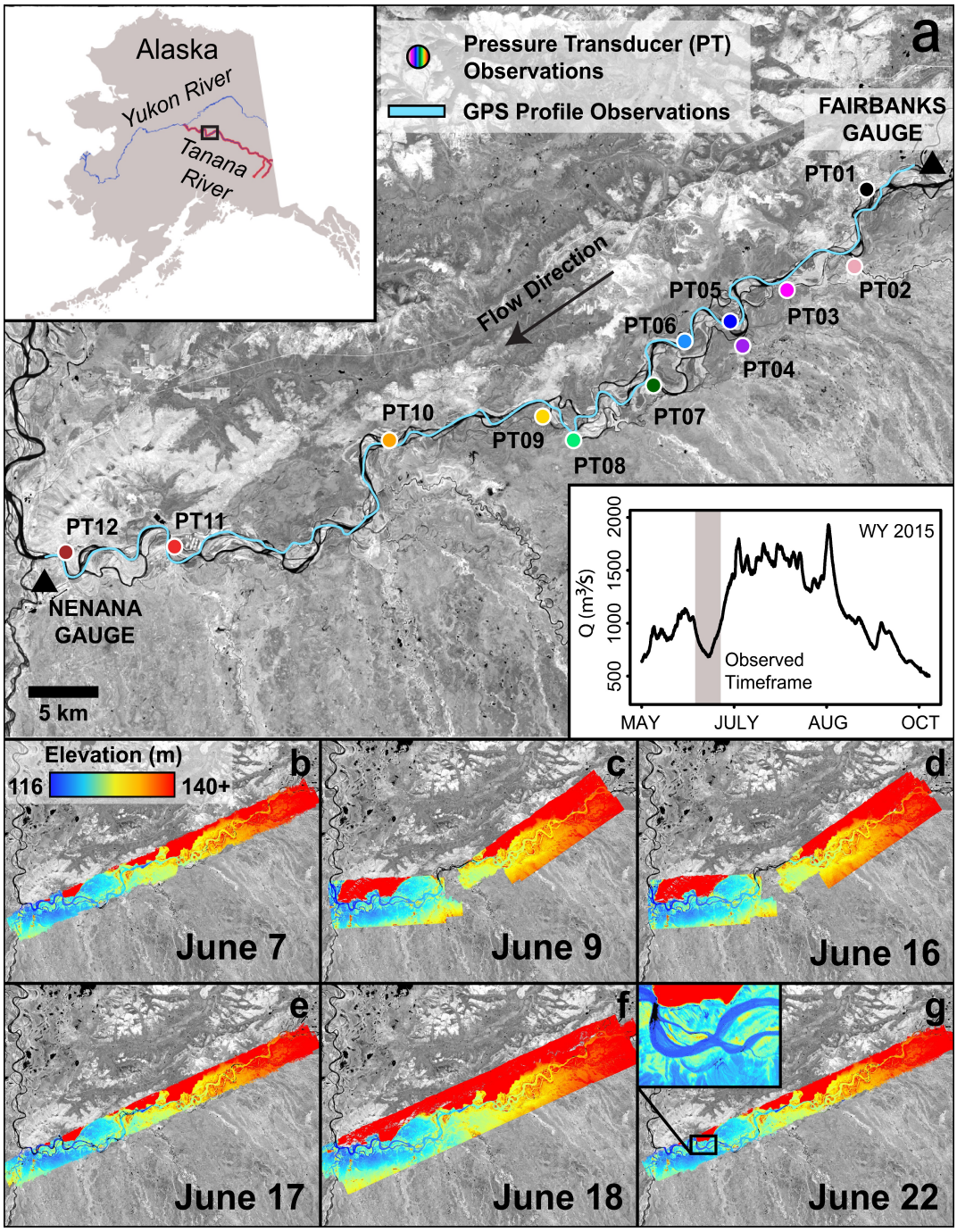

Figure 3.1: a) Tanana River study reach depicted with a Landsat 8 near-infrared image acquired on June 15, 2015. Pressure transducer (PT) locations are indicated by the different colored circles and GPS profile measurements are indicated by the light blue line. Upper left inset displays the study reach location within the state of Alaska. Lower right inset displays the Nenana gauge hydrograph during the open water season for the 2015 water year (WY). The grey shaded area within the hydrograph shows the timeframe of the field campaign. b-g) AirSWOT extent and height mosaics for the six different flights.

In addition to the pressure transducers, we collected a high-resolution GPS profile along the main channel of the study reach on June 7, 2015 (Figure 3.1a). We collected the profile using a Trimble R9 survey-grade GPS system attached to the back of an 8.5 m river boat. The profile measurements provide nearly continuous observations of river heights with ~3 m spacing between points and an uncertainty of ±0.02 m [*Altenau et al.,* 2017a]. Along with the river heights, we collected depths at each GPS profile point using a single-beam SonarMite Echo Sounder v.3.0. Instrument accuracy for the echo sounder is ±0.025 m [*http://www.ohmex.com/sonarmite.html*].

3.2.2 AirSWOT Measurements

AirSWOT collected measurements on six different days (June 7, June 9, June 16, June 17, June 18, and June 22, 2015) during the field campaign to capture multi-temporal fluctuations in river height and slope. Each AirSWOT mission consists of 4-24 overlapping flight lines per day resulting in a total of 66 individual lines of AirSWOT height measurements. The June 9th and June 16th collections contain 24 flight lines that cover a 43 km east region and 32 km west region of the study reach, while the remaining days contain 4-6 flight lines of data covering the entire 90 km study reach (Figure 3.1b-g). The AirSWOT team at NASA's Jet Prolusion Laboratory processes the AirSWOT data using custom software. Each AirSWOT flight line consists of 4 products with the primary product being the AirSWOT heights measured in meters above the WGS84 ellipsoid. Other products provided with the heights are relative radar backscatter (dB), incidence angle (°) and estimated height errors (m). Estimated height errors are calculated from the phase variance (Cramer-Rao bound) which is based on the correlation between the two interferometric images and depends on the sensor incidence angles, radar wavelength, and underlying surface type (high topography, vegetation type, soil moisture, etc.)

[*Rosen et al.*, 2000; *Altenau et al.*, 2017a]. All AirSWOT products are in a raster format and have a pixel resolution of 3.6 m with a UTM 6N projection.

In this paper, we focus on the ability of AirSWOT to record changes in river heights and slopes. To do so, we filter the AirSWOT data before comparing it to the *in situ* pressure transducer measurements. For each AirSWOT line, we use a binary river mask created from a three-band color infrared (CIR) camera [*http://cirrus-designs.com/*] on board the AirSWOT platform to isolate the river pixels from surrounding land pixels. Regrettably, the majority of CIR images collected during the AirSWOT flights were cloudy or covered by high cirrus clouds that did not substantially impact the visible bands but affected the near-infrared band. These clouds prevent us from using automatic methods to create an independent river mask for each date. The imagery was clear for the June 17th flight, however, so we use this imagery to create the river mask and filter out the land pixels in each AirSWOT line. We produce the river mask using a normalized difference water index (NDWI) transformation with a threshold of 0.3 to identify water pixels [*McFeeters*, 1996]. All pixels greater than the threshold are assigned a value of one for water and any pixels less than the threshold are assigned a value of zero. The river on June 17th was at lower stage than the majority of the data collections with the exception of June 16th, which had a stage about 5 cm lower than June 17th. As a result, the river extent observed in the river mask should be comparable to June 16th, but is likely to exclude some inundated pixels on the other collection days. Once the river heights are isolated, we use a 2 km^2 moving window to remove extreme outliers by erasing pixels ±3 standard deviations away from the mean river height in the window [*Altenau et al.,* 2017a]. This filter helps eliminate pixels affected by layover from adjacent high topography and vegetation, as well as misclassified water/land pixels from the water mask.

When using near-nadir geometry, layover tends to occur in environments with moderate-to-high topography, and the ambiguity height parameter that is used to calculate the water heights has a faster range variation [*Neeck et al.*, 2012]. As a result, calculating ambiguity heights can be more difficult, especially in the near-swath and in areas adjacent to higher topography. Incorrect ambiguity heights often lead to high vertical errors and geolocation errors [*Biancamaria et al.*, 2016]. Ambiguity height errors are prominent in 9 of the 66 AirSWOT lines. These large areas of incorrect pixels are not removed during our filtering process because they significantly affect the statistics within the 2 km^2 window we use to eliminate the outliers. Therefore, we manually remove the incorrect pixels in these areas (Figure 3.2).

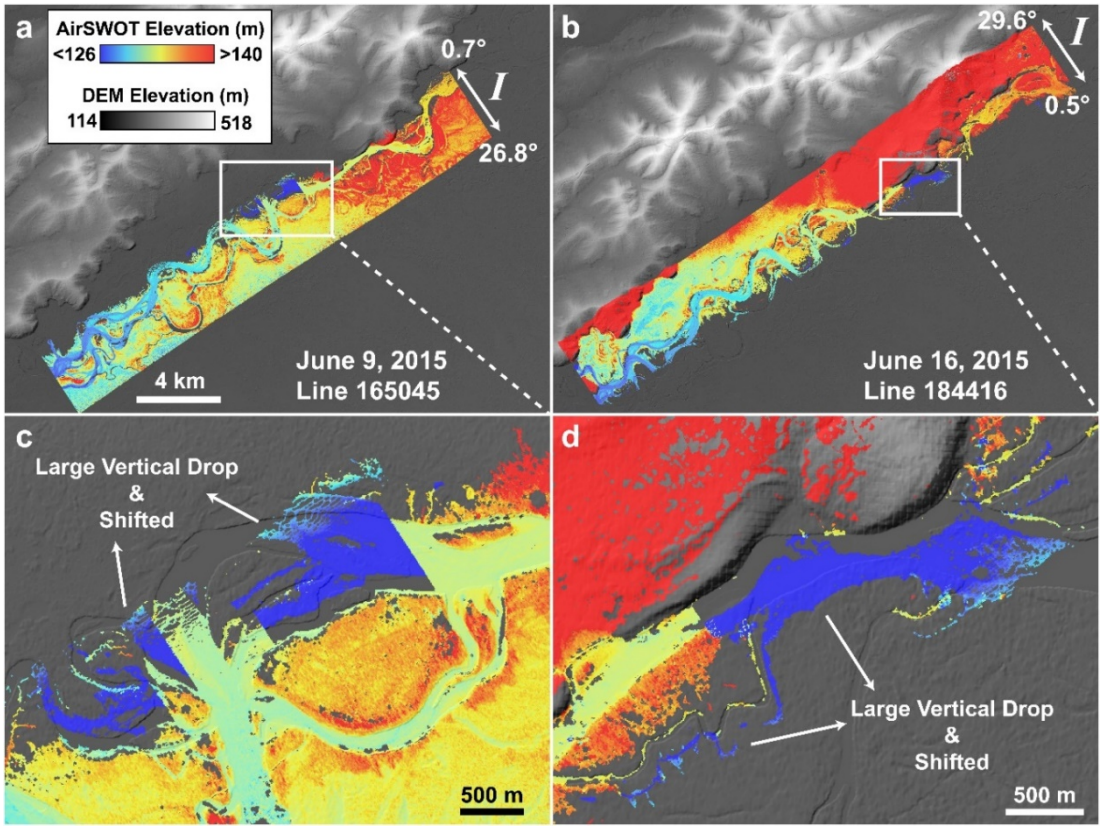

Figure 3.2: Examples of ambiguity height errors in two AirSWOT lines from June 9, 2015 and June 16, 2015. The areas of dark blue pixels, which designate significant vertical drops and geolocation errors, are manually removed.

3.2.3 Height Validation

The SWOT baseline mission error requirement for river heights of 10 cm is based on averaging pixels within 1 km^2 areas, a threshold the SWOT Science Team has determined will allow significant advances in fluvial hydrology [*Rodriguez*, 2016]. Therefore, we use this area requirement as a baseline for assessing AirSWOT's capabilities for measuring same-day river heights as well as capturing river height changes over time [*Altenau et al.,* 2017a]. To quantify height differences between AirSWOT and the *in situ* measurements for each flight date, we calculate a weighted average of the filtered AirSWOT heights within 1 km^2 areas around each pressure transducer using the following equation:

$$\bar{x} = \frac{\sum_{i=1}^{n} x_i w_i}{\sum_{i=1}^{n} w_i} \tag{3.1}$$

where $\bar{x}$ is the weighted average of the AirSWOT heights at a single pressure transducer location, x_i is the AirSWOT height for each pixel (i), and w_i is the weight associated with each pixel and is determined by the estimated height error (e_i):

$$w_i = \frac{1}{{e_i}^2} \tag{3.2}$$

Despite filtering of the AirSWOT heights described in section 3.2.2, some remaining erroneous pixels affected by ambiguity height errors are still present in the data. These pixels tend to have large height offsets compared to field observations but low e_i values, resulting in comparatively high errors in the weighted average calculation. To reduce the effects of these pixels, we calculate the median for each 1 km^2 area and retain 70% of the AirSWOT heights that surround the median value. We also eliminate pixels that have estimated errors of < 0.1 m because we find these particularly low error estimates often correspond with pixels that are

affected by ambiguity height errors. Pixels with estimated errors < 0.1 m make up less than 1% of the data, therefore this second filter preserves about 70% of the data while reducing the errors in the weighted average that are caused by the incorrect pixels.

It is difficult to calculate uncertainties for the averaged heights using the AirSWOT data alone. We can calculate the random error component of the uncertainty for the averaged AirSWOT heights based on the weights (w_i):

$$uncertainty = \frac{\sqrt{F}}{\sqrt{\sum_{i=1}^{n} w_i}} \tag{3.3}$$

where F is a factor that accounts for the oversampling of pixels within the gridded UTM product relative to the sampling assumed when estimating the height errors and depends on the incidence angle (I):

$$F = \frac{0.52}{\sin(I)} \tag{3.4}$$

The constant 0.52 comes from the ratio (1.87 m)/(3.6 m) where 1.87 m is the effective resolution for 80 MHz bandwidth and 3.6 m is the UTM posting. Equation 3.3 accounts for the random error component (noise on the interferometric phase) in the AirSWOT measurement uncertainty, but does not include systematic errors that are due to variations in antenna pointing and knowledge of the airborne platform location such as attitude errors, baseline errors, and position errors [*Rodriguez and Martin*, 1992; *Rosen et al.*, 2000]. As a result, the uncertainties calculated using equation 3.3 are unrealistically low, ranging from 0.1 – 2.0 cm. Systematic errors in the AirSWOT data affect the accuracy of the heights, and likely add to the random error uncertainty, but cannot be quantified from the data itself or from ancillary information available to us. Rather than present misleading uncertainty values, we elect not to designate uncertainties for the

averaged AirSWOT heights and focus on reporting the differences between the AirSWOT and *in situ* measurements.

Once the averaged AirSWOT heights are determined, we calculate the same-day height differences and associated root mean square errors (RMSEs) between the AirSWOT and pressure transducer heights. Although *Altenau et al.* [2017a] report no bias in the June 9th AirSWOT measurements, we observe a spatially consistent negative bias across the AirSWOT heights that ranges from -18 cm to -24 cm depending on the collection day. The AirSWOT data we present in this paper is processed using different methods from the data presented in *Altenau et al.* [2017a] and we have not determined the source of the bias in the current data at this time. Possible explanations for the bias include improper common range calibrations, differences in how solid earth tide corrections are incorporated, erroneous GPS solutions, and problems with the troposphere correction. As a result, we subtract the mean bias on each day from the AirSWOT heights and recalculate the differences and RMSEs between the same-day AirSWOT and pressure transducer heights (Table 3.1).

In addition to the same-day heights, we calculate height change values for the pressure transducers and AirSWOT between the first AirSWOT date (June 7th) and all subsequent dates (n = 58), as well as height changes between all possible AirSWOT date combinations (n = 161). We estimate uncertainties for the *in situ* height changes by taking the root sum of squares of the uncertainties in the daily pressure transducer heights. Finally, we calculate height change differences and RMSEs between the AirSWOT and pressure transducer observations for the height changes between June 7th and all subsequent dates as well as height changes between all possible date combinations.

Date	Height RMSE (cm)	Mean Height Bias (cm)	Height RMSE, Bias removed (cm)	Slope RMSE (cm/km)
June 7	27.4	-24.0	13.2	1.4
June 9	23.9	-18.0	14.9	1.8
June 16	27.1	-24.0	10.6	1.8
June 17	20.1	-17.6	9.7	1.6
June 18	27.2	-24.0	12.7	1.7
June 22	23.8	-17.6	14.3	1.2
All Days	25.0	-20.9	12.7	1.6

Table 3.1: Same-day AirSWOT height and slope RMSEs.

3.2.4 Slope Validation

Using pairs of the 12 pressure transducer locations, we identify a total of 63 combinations for calculating slopes with reach lengths ≥5 km. We calculate slopes across varying reach lengths ranging from 5.1 to 83.6 km. AirSWOT slopes for reach lengths <5 km start to be severely affected by noise in the AirSWOT data. Before we calculate AirSWOT slopes, we create high-resolution AirSWOT profiles using the GPS profile collected in the field (Figure 3.1a). At each GPS profile point, we calculate a 1 km orthogonal vector across the Tanana River and use equation 3.1 to calculate a weighted mean of the AirSWOT heights along the orthogonal vector. After weighted averaging, we create the final AirSWOT profiles by applying a running median filter with a window of 500 pixels (~1600 m) to eliminate large peaks in the initial profiles (Figure 3.3). The running median filter reduces high frequency variability, which is unrealistic for a large river like the Tanana. While a window size of 500 pixels works well for the Tanana River profile, optimal window size likely varies between river environments depending on geology, morphology, size and other factors.

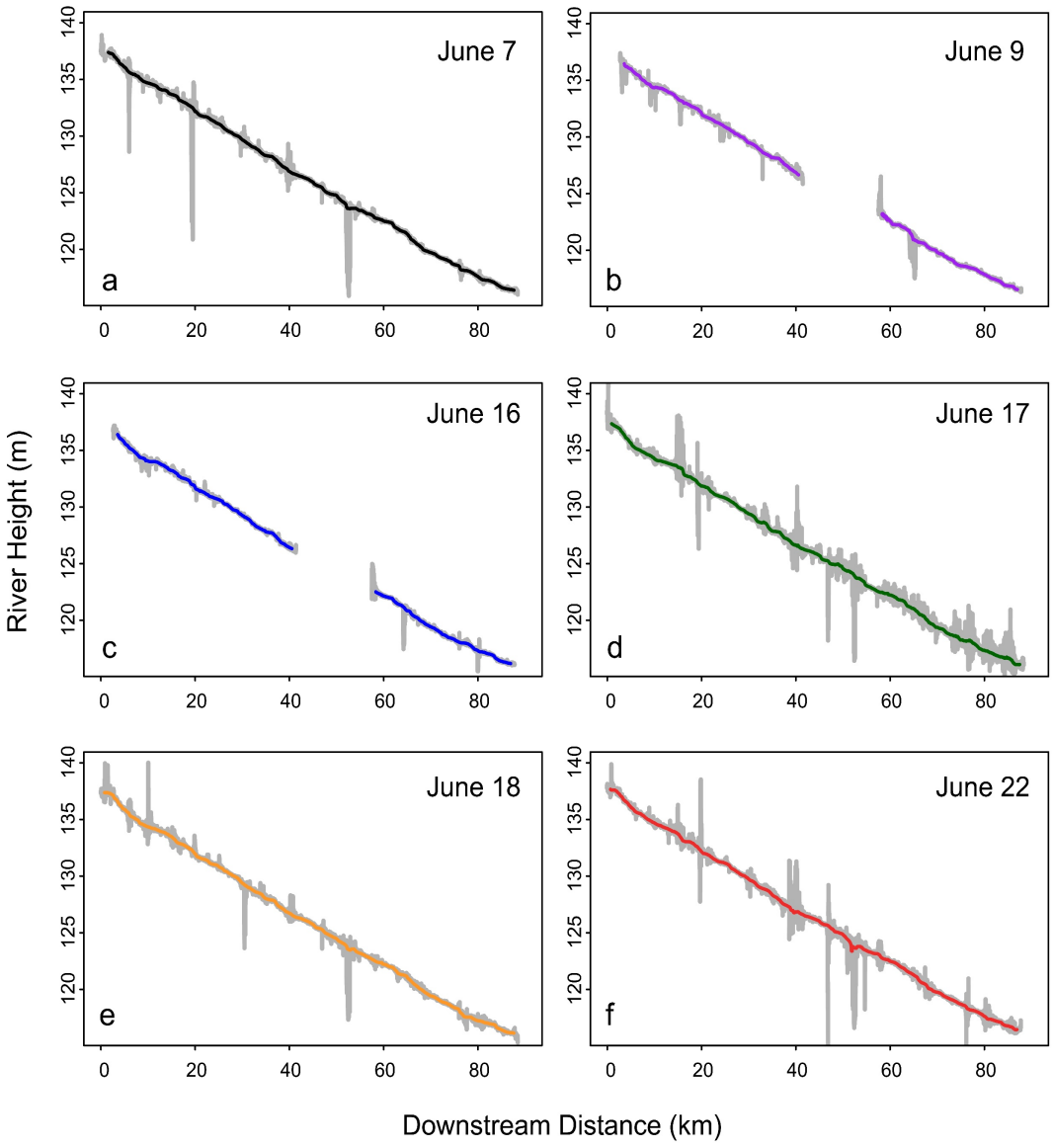

Figure 3.3: AirSWOT river height profiles. River heights are measured in meters above the WGS84 ellipsoid. We remove severe peaks in the initial profiles (grey) by using a running median filter with a window size of 500 points (~1600 m) resulting in the final profiles (colors). We use the final profiles to calculate slopes and slope changes.

We use ordinary least squares linear regressions to calculate same-day slopes along the AirSWOT profiles between each pressure transducer pair. For each pressure transducer combination, we estimate the *in situ* slopes using the elevations at each pressure transducer point and reach length between the points. We estimate AirSWOT slope uncertainties using the linear

regressions, and the pressure transducer slope uncertainties by calculating the difference between the maximum and minimum slopes for each pressure transducer pair, which are based on the pressure transducer height uncertainties. To validate AirSWOT slope measurements, we calculate same-day slope differences and RMSEs between the AirSWOT and pressure transducer slopes.

Next, we calculate the slope changes between the first AirSWOT date (June 7th) and all subsequent dates (n = 297), as well as all possible AirSWOT date combinations (n = 766). We estimate uncertainties for the slope changes by taking the root sum of squares of the uncertainties in the same-day pressure transducer and AirSWOT slopes. We then calculate slope change differences and RMSEs between the AirSWOT and pressure transducer slope changes between June 7th and all subsequent dates, and slope changes between all possible date combinations. Finally, we perform a Welch two-sample t-test to determine whether the slope change distributions observed by AirSWOT and the pressure transducers are significantly different.

3.2.5 Discharge Estimation

In addition to validating AirSWOT's ability to capture multi-temporal fluctuations in river height and slope, we assess how well AirSWOT observations compare to the pressure transducer observations when estimating discharge using Manning's equation [*Manning et al.,* 1890]. To calculate discharge, we need to approximate the roughness (Manning's n), slope, depth, and width of the Tanana River at each pressure transducer cross section. First, we use the depth measurements collected with the GPS profile to calculate an average bed slope and bathymetric elevation at each pressure transducer location. Then, we calculate average depths at each of the pressure transducer sites by subtracting the bathymetric elevations from the pressure transducer and AirSWOT river heights [*Altenau et al.*, 2017b] . Next, we determine slopes at

each cross section by locating the closest upstream and downstream pressure transducers to the current pressure transducer location and calculate the slope between the two bounding sites. The two exceptions are pressure transducer locations #1 (PT01) and #12 (PT12) for which we use the closest downstream and upstream location only to calculate the slopes. For example, we determine the slope for PT05 by calculating the slope between PT04 and PT06, and we determine PT01's slope by calculating the slope between PT01 and PT02. For cross sectional widths, we use the CIR imagery collected during each AirSWOT flight to manually measure the river widths at the various pressure transducer sites, since the clouds in the imagery inhibit us from using automatic width detection methods. We exclude two pressure transducer sites from our discharge estimates due to a lack of width measurements from dense cloud cover (PT07) and fewer AirSWOT observations (PT10), leaving us ten locations to estimate discharge. Finally, we calibrate n at each location using the discharge at the Nenana USGS gauge station (15515500) (Figure 3.1a, Table 3.2). To estimate *in situ* discharge uncertainties, we calculate maximum and minimum discharge values based on the pressure transducer height and slope uncertainties. We compare the AirSWOT and pressure transducer discharge estimates by calculating daily RMSE values.

We perform a sensitivity analysis for 4 different cross sectional shapes (rectangle, parabola, triangle, and trapezoid) and find a negligible (0.2%) effect on mean discharge differences. As a result, we use a simple rectangular geometry when estimating discharge values. Our goal in this discharge analysis is to assess how using AirSWOT heights and slopes change discharge estimates compared to *in situ* measurements. Given the simplifications to channel geometry compared to the complexity of the Tanana River, as well as the uncertainties in the

Manning's equation parameters, we do not attempt to compare either the *in situ* or AirSWOT results against gauge measurements.

Pressure Transducer	Average Width (m)	Number of Channels in Cross Section	Manning's n
1	553	5	0.07
2	434	4	0.065
3	323	1	0.05
4	541	6	0.07
5	519	6	0.06
6	403	4	0.05
8	282	2	0.04
9	229	2	0.03
11	339	2	0.045
12	269	1	0.04

Table 3.2: Manning's equation parameters for each pressure transducer cross section.

3.3. Results

RMSEs for the same-day AirSWOT heights range from 9.7 cm to 14.9 cm with an overall RMSE of 12.7 cm (Figure 3.4a,c; Table 3.1). The patterns in height differences between the same-day AirSWOT and pressure transducer heights are similar across all days (Figure 3.4c), which indicates the different AirSWOT flights are affected by comparable error sources (likely layover). In addition to the same-day height measurements, AirSWOT is able to reproduce patterns in multi-temporal height changes between June 7th and all subsequent dates as well as height changes between all possible date combinations with RMSEs of 10.3 cm and 10.4 cm (Figure 3.5). AirSWOT height change differences shift from underestimations upstream to overestimations downstream (Figure 3.5d). The variations in height change differences between the pressure transducer sites are likely due to the different environmental conditions at each location are how they affect the radar returns. Additionally, PT10 displays a much larger range in height change errors. PT10 is directly adjacent to an area of high topography making it susceptible to layover errors and is not covered by the June 9th and June 16th AirSWOT

collections, giving it less data to average out individual pixel errors (Figure 3.1).

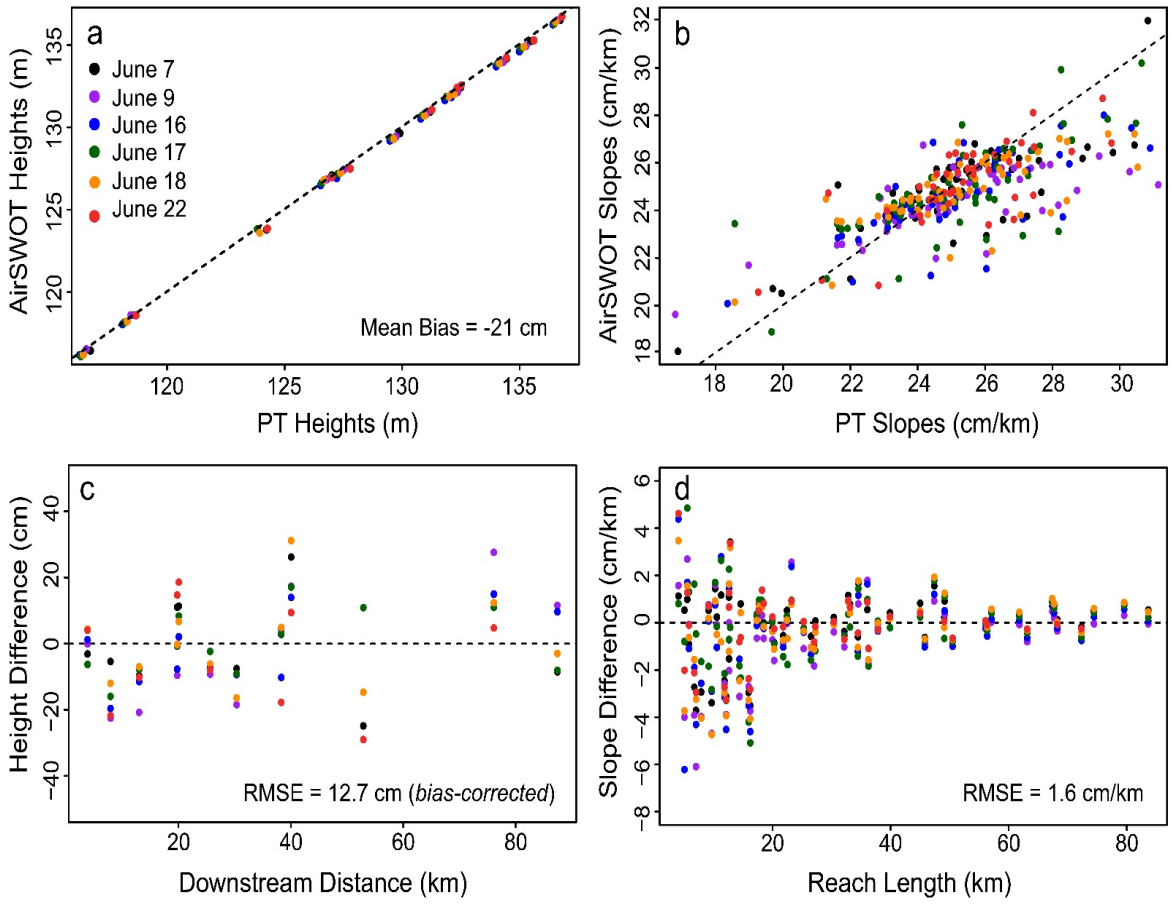

Figure 3.4: AirSWOT vs. pressure transducer (PT) heights (a) and slopes (b). Dashed diagonal lines indicate the 1:1 lines. AirSWOT height (c) and slope (d) differences compared to the pressure transducers for the various AirSWOT collections. Height differences are shown with the daily mean biases removed. Dashed horizontal lines indicate zero height and slope differences.

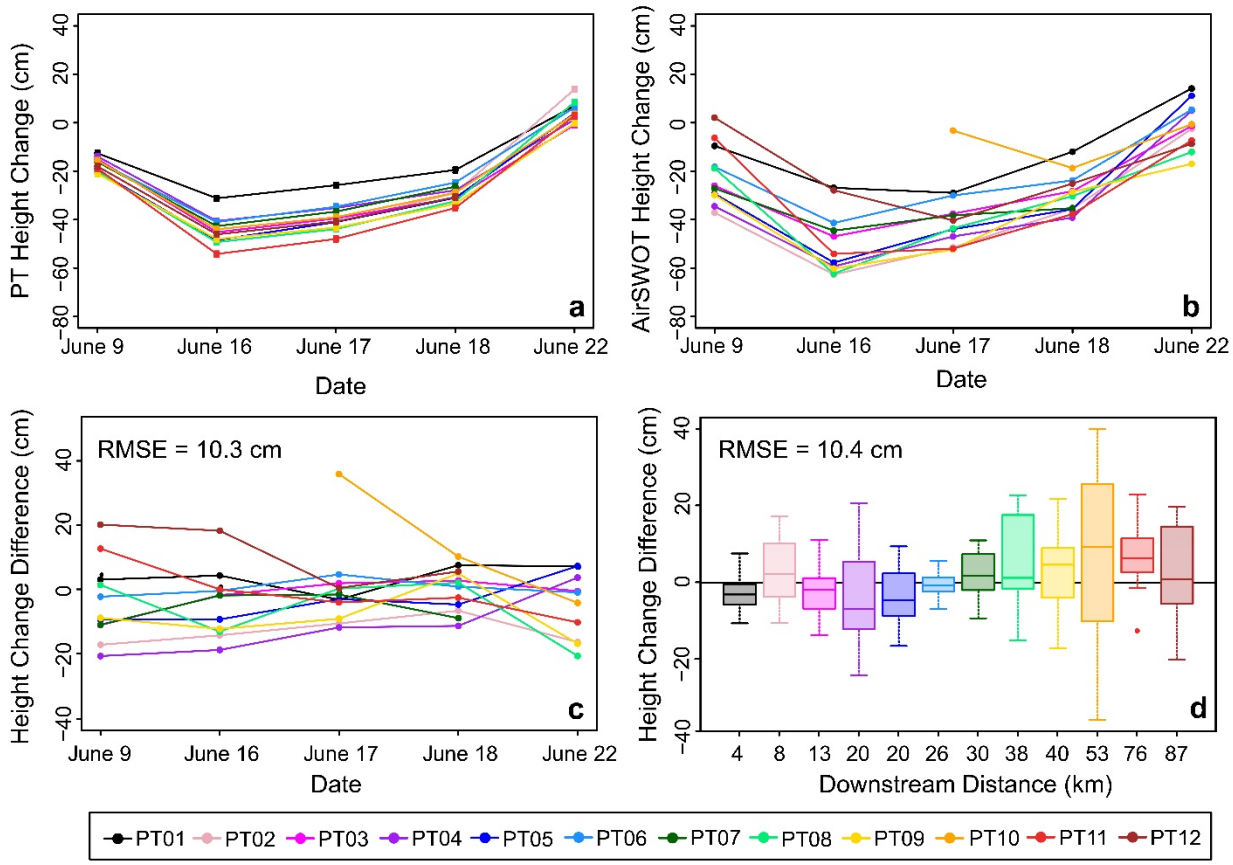

Figure 3.5: Pressure transducer (PT) (a) and AirSWOT (b) height changes between June 7th and all subsequent dates (n = 58). c) AirSWOT height change differences between June 7th and all subsequent dates. d) AirSWOT height change differences at each pressure transducer location for all possible date combinations (n = 161). Different colors represent the various PT locations. Pressure transducer uncertainty bars are too small to see.

AirSWOT is able to precisely observe slopes with centimeter-per-kilometer-level accuracies. Same-day slope differences increase as reach length decreases, with an RMSE of 1.6 cm/km and 98% of slope differences below 3.0 cm/km for reach lengths ≥5 km (Table 3.1, Figure 3.4d). Tanana River slopes do not change much over the six AirSWOT collection days, though slight increases in slope are observed by the pressure transducers as stage decreases (Figure 3.6a). Mean slope changes observed by pairs of pressure transducers from June 7th to all subsequent dates ranged from 0.07 cm/km to 0.17 cm/km, while mean AirSWOT slope changes ranged from -0.35 cm/km to 0.26 cm/km. For the slope changes between June 7th and all

subsequent days, only the AirSWOT slope change distribution between June 7th and June 9th is determined statistically different from the pressure transducers at the 95% confidence level and a p-value of 0.006. All other AirSWOT slope change distributions from June 7th to all subsequent dates cannot be determined significantly different from the pressure transducers with p-values ranging from 0.106 to 0.612. While the June 7th to June 9th AirSWOT slope changes are considered significantly different from the pressure transducer slope changes, the AirSWOT slope change distribution for all possible date combinations cannot determined significantly different from the pressure transducers with a p-value of 0.075. This indicates that, overall, AirSWOT measurements of slope changes cannot be distinguished from the pressure transducer slope change observations. Even with the slight variations in slope throughout the field campaign, AirSWOT is able to capture the general pattern in slope changes with an RMSE of 1.0 cm/km (Figure 3.6a,b). Additionally, AirSWOT displays lower uncertainties compared to the pressure transducers with uncertainties decreasing exponentially as reach length increases (Figure 3.6b).

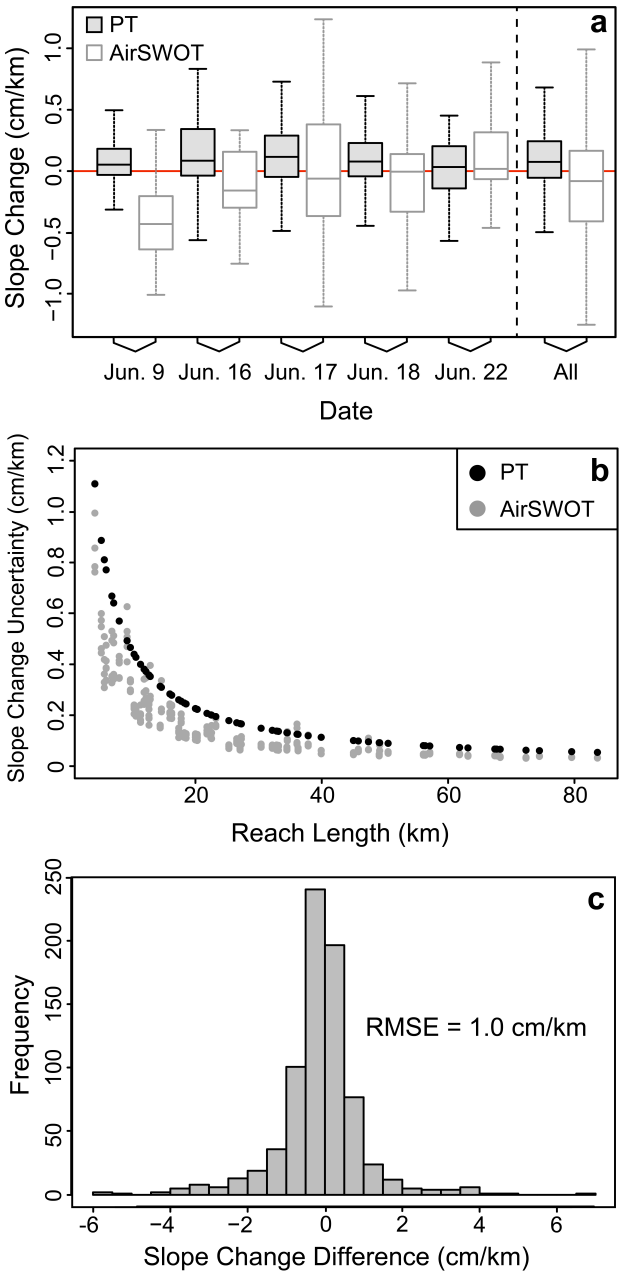

Figure 3.6: a) Boxplots of observed slope changes by the pressure transducers (grey) and AirSWOT (white) between June 7th and all subsequent dates (n = 297), as well as all possible date combinations (All) (n = 766). Outliers make up 15% of the data points and are not shown in the boxplots of slope change distributions. The red horizontal line designates zero slope change, while the black vertical dashed line separates the consecutive height change distributions from the distributions for all possible date combinations. b) AirSWOT and pressure transducer (PT) slope change uncertainties versus reach length. c) AirSWOT slope change differences for all possible date combinations.

Both the pressure transducer and AirSWOT discharge estimates are able to capture the general hydrograph pattern observed during the field campaign (Figure 3.1a) with discharge decreasing until June 16th and increasing thereafter (Figure 3.7). AirSWOT discharge estimates display a 15.3% difference, on average, compared to the pressure transducer estimates with RMSEs ranging from 11.8% to 18.3% between dates (Table 3.3). Additionally, 42% of the AirSWOT discharge estimates fall within the pressure transducer uncertainty bounds for discharge estimates. Discharge differences are predominately related to the AirSWOT height differences. A linear regression between discharge differences and height differences (R^2=0.95) shows a 1.2% increase in discharge difference with every centimeter of height difference (Figure 3.8a). Conversely, there is no relationship between AirSWOT slope differences and discharge differences, with an R^2 of 0.03 (Figure 3.8b). The variations in discharge patterns observed between pressure transducer sites are likely explained by our lack of temporal variation in Manning's n, bathymetric slope assumptions, and not accounting for variations in cross-sectional shape across the locations.

Date	RMSE (m^3/s)	RMSE (%)
June 7	147.0	13.1
June 9	160.6	18.3
June 16	88.4	15.0
June 17	74.1	11.8
June 18	111.8	14.8
June 22	171.0	14.2
All Days	130.7	15.3

Table 3.3: RMSEs between AirSWOT and pressure transducer discharge estimates. We estimate discharge using Manning's equation.

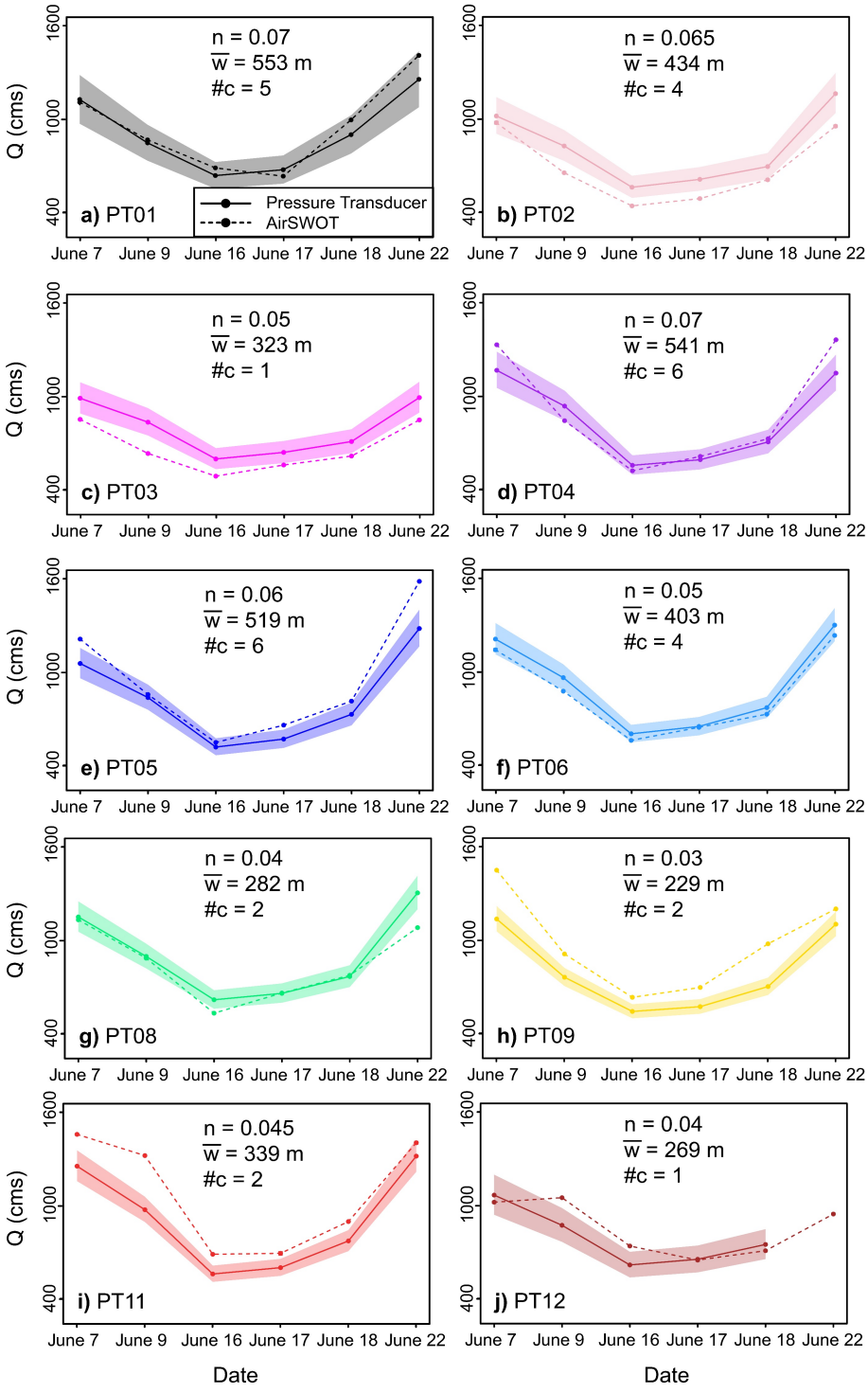

Figure 3.7: Estimated discharge using Manning's equation. Solid colored lines display discharge estimates using the pressure transducer (PT) heights and slopes, while dashed colored lines display discharge estimates using AirSWOT heights and slopes. Shaded areas indicate the pressure transducer discharge uncertainties. Manning's n (n), average width ($\overline{w}$), and number of channels in the cross section (#c) are shown.

3.4. Discussion and Conclusion

In this study, we present a first analysis of AirSWOT's ability to collect high-precision, multi-temporal measurements of river heights and slopes over variable reach lengths and flexible timescales. *Altenau et al.* [2017a] document AirSWOT's ability to record accurate river heights and slopes for one collection date, while here we analyze the consistency of AirSWOT measurements over the course of three weeks and six different AirSWOT flights. Comparisons with *in situ* observations illustrate that AirSWOT is able to accurately measure surface water fluctuations along a complex, anabranching river system, with an RMSE of 12.7 cm for same-day river heights averaged across 1 km^2 areas and 1.6 cm/km for same-day slopes with reach lengths ≥5 km (Table 3.2). It is not always straightforward for AirSWOT to measure same-day river heights due to errors and biases that are likely related to the movement of the aircraft and difficulties in phase unwrapping at narrower incidence angles (<5°). AirSWOT heights for the six independent collection days are affected by the same types of errors and produce similar spatial patterns in the same-day height and slope differences when compared to *in situ* heights (Figure 3.4c,d, Table 3.1). Despite these errors, AirSWOT is able to capture decimeter-level height changes and centimeter-per-kilometer-level slope changes between collection days (Figure 3.5d, Figure 3.6c). RMSEs for AirSWOT height and slope change measurements between all possible AirSWOT date combinations are 10.4 cm when averaged over 1 km^2 areas and 1.0 cm/km for reach lengths ≥5 km, respectively.

Despite the challenges inherent in making precise measurements of surface water heights when using an airborne radar, AirSWOT provides a compelling alternative to *in situ* observations for measuring river dynamics, thereby opening up exciting new avenues for local and regional scale hydrologic studies. AirSWOT's slope measurements are particularly revolutionary due to

their high accuracy and spatial density compared to available satellite sensors and *in situ* measurements. *In situ* gauge stations provide extremely accurate river height measurements, but are not ideal for estimating slope variability due to their poor spatial coverage. Additionally, studies have used nadir altimeter data to estimate river slopes, however, altimeter measurements suffer from poor spatial resolutions and large height uncertainties resulting in slopes that are less precise compared to AirSWOT [*O'Loughlin et al.*, 2013; *Garambois et al.*, 2016]. Especially when combined with existing ground measurements, AirSWOT observations can enhance our representation of hydraulic behaviors and knowledge of streamflow regimes along entire river networks [*Domeneghetti et al.*, 2014; *Altenau et al.*, 2017a]. Multi-temporal AirSWOT measurements can be used to quantify water partitioning and hydraulics in complex environments, such as deltas and braided rivers, which are often difficult to access and onerous to install *in situ* instrument networks [*Bridge*, 1993; *Pavelsky et al.*, 2014]. Furthermore, AirSWOT observations can be combined with optical sensors to analyze how spatiotemporal variability in water heights and slopes relate to sediment and nutrient delivery along entire river reaches [*Pavelsky and Smith*, 2009; *Long and Pavelsky*, 2013; *Tejedor et al.*, 2017; *Wollheim et al.*, 2017]. Finally, measurements of river heights and slopes from AirSWOT can be used for calibration, validation, and assimilation into local and regional-scale flood models to improve their performance by providing similar, and often superior, accuracies and better spatiotemporal coverage than existing airborne and satellite sensors [*Domeneghetti et al.*, 2014].

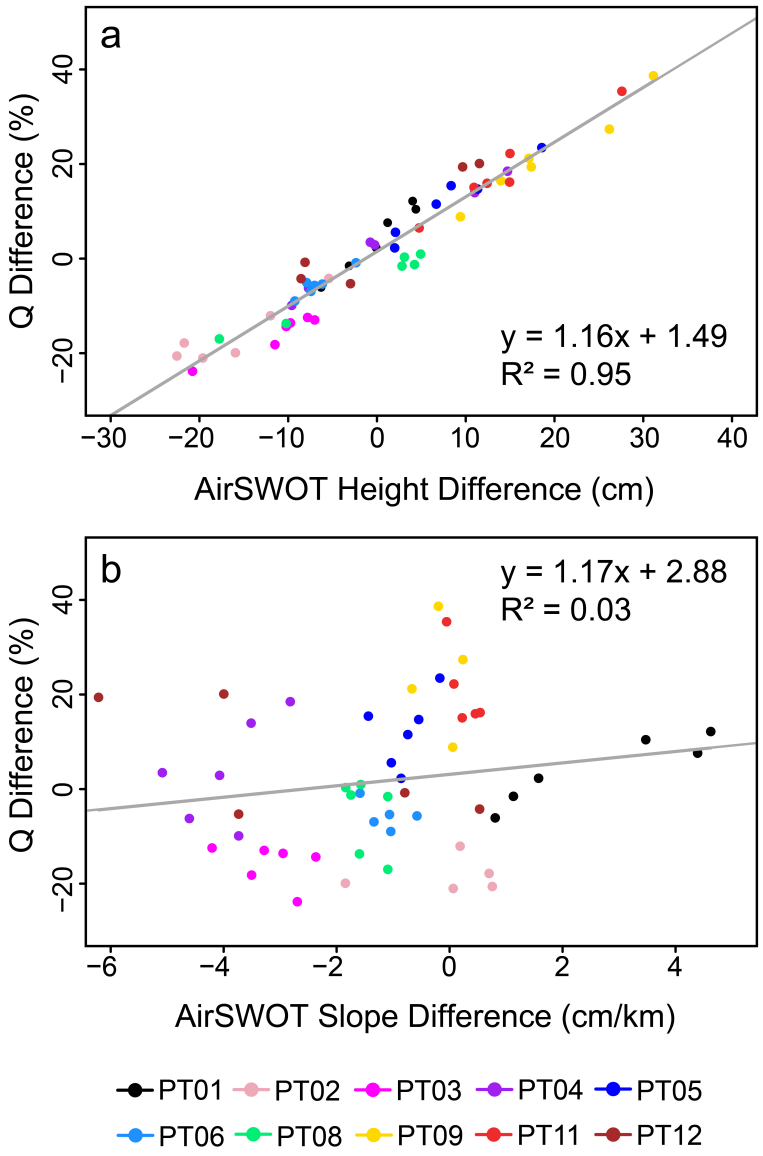

Figure 3.8: AirSWOT height (a) and slope (b) differences versus discharge difference. Colored dots represent different pressure transducer (PT) locations.

In addition to validating AirSWOT's direct measurements of height and slope, we test the effectiveness of AirSWOT observations for approximating discharge. To do so, we use Manning's equation to calculate and compare discharge estimates using both the pressure transducer and AirSWOT measurements of river height and slope. Our analysis demonstrates AirSWOT measurements contribute marginal differences when estimating discharge compared

to *in situ* measurements. On average, AirSWOT discharge estimates are within 15.3% of the estimates attained using the pressure transducers and 42% of the time AirSWOT discharge measurements fall within the pressure transducer discharge uncertainty (Table 3.3). For the Tanana River, AirSWOT height differences dominate the observed discharge differences, with slope differences showing little effect (Figure 3.8). This result is likely due, in part, to the limited slope variations occurring throughout the Tanana River during our field campaign. More work analyzing how AirSWOT slope errors affect discharge estimates is needed during more extreme hydrologic events and along rivers with more slope variability over time. Because development of AirSWOT processing methods is ongoing, AirSWOT height errors and biases are likely to decrease in the future, along with a corresponding decrease in discharge errors. When combined with sophisticated algorithms, and appropriate parameters, AirSWOT measurements can be used to estimate discharge fluctuations along inaccessible and unmonitored river networks that are smaller than what current and future satellite missions can observe [*King et al.*, 2018].

REFERENCES

Alsdorf, D. E., E. Rodríguez, and D. P. Lettenmaier (2007), Measuring surface water from space, *Rev. Geophys.*, *45*(2), RG2002, doi:10.1029/2006RG000197.

Altenau, E. H., T. M. Pavelsky, D. Moller, C. Lion, L. H. Pitcher, G. H. Allen, P. D. Bates, S. Calmant, M. Durand, and L. C. Smith (2017a), AirSWOT measurements of river water surface elevation and slope: Tanana River, AK, *Geophys. Res. Lett.*, 1–9, doi:10.1002/2016GL071577.

Altenau, E. H., T. M. Pavelsky, P. D. Bates, and J. C. Neal (2017b), The effects of spatial resolution and dimensionality on modeling regional-scale hydraulics in a multichannel river, *Water Resour. Res.*, *53*(2), 1683–1701, doi:10.1002/2016WR019396.

Bates, P. D., J. C. Neal, D. Alsdorf, and G. J.-P. Schumann (2014), Observing Global Surface Water Flood Dynamics, *Surv. Geophys.*, *35*(3), 839–852, doi:10.1007/s10712-013-9269-4.

Biancamaria, S., D. P. Lettenmaier, and T. M. Pavelsky (2016), The SWOT Mission and Its Capabilities for Land Hydrology, *Surv. Geophys.*, *37*(2), 307–337, doi:10.1007/s10712-015-9346-y.

Brabets, T. P., B. Wang, and R. H. Meade (2000), Environmental and Hydrologic Overview of the Yukon River Basin , Alaska and Canada, *US Dep. Inter. US Geol. Surv.*

Bridge, J. S. (1993), The interaction between channel geometry, water flow, sediment transport and deposition in braided rivers, *Geol. Soc. London, Spec. Publ.*, *75*(1), 13–71, doi:10.1144/GSL.SP.1993.075.01.02.

Calmant, S., F. Seyler, and J. F. Cretaux (2008), Monitoring continental surface waters by satellite altimetry, *Surv. Geophys.*, *29*(4-5), 247–269, doi:10.1007/s10712-008-9051-1.

Domeneghetti, A. (2016), On the use of SRTM and altimetry data for flood modeling in data-sparse regions, *Water Resour. Res.*, 1–20, doi:10.1002/2014WR015716.

Domeneghetti, A., A. Tarpanelli, L. Brocca, S. Barbetta, T. Moramarco, A. Castellarin, and A. Brath (2014), The use of remote sensing-derived water surface data for hydraulic model calibration, *Remote Sens. Environ.*, *149*, 130–141, doi:10.1016/j.rse.2014.04.007.

Fjørtoft, R. et al. (2014), KaRIn on SWOT: Characteristics of near-nadir Ka-band interferometric SAR imagery, *IEEE Trans. Geosci. Remote Sens.*, *52*(4), 2172–2185, doi:10.1109/TGRS.2013.2258402.

Fu, L.-L., D. Alsdorf, R. Morrow, and E. Rodriguez (2015), SWOT: The Surface Water and Ocean Topography Mission, *SWOT NASA/JPL Proj.*, doi:10.1017/CBO9781107415324.004.

Garambois, P., S. Calmant, H. Roux, A. Paris, P. Finaud-guyot, A. Montazem, J. Santos, O. Spatiales, U. M. R. Cnes, and C. Ird (2016), Hydraulic visibility : using satellite altimetry to parameterize a hydraulic model of an ungauged reach of a braided river, *Hydrol. Process.*, 1–20, doi:10.1002/hyp.11033.

Hannah, D. M., S. Demuth, H. A. J. van Lanen, U. Looser, C. Prudhomme, G. Rees, K. Stahl, and L. M. Tallaksen (2011), Large-scale river flow archives: Importance, current status and future needs, *Hydrol. Process.*, *25*(7), 1191–1200, doi:10.1002/hyp.7794.

King, T. V., B. T. Neilson, and M. T. Rasmussen (2018), Estimating Discharge in Low-Order Rivers with High-Resolution Aerial Imagery, *Water Resour. Res.*, 1–16, doi:10.1002/2017WR021868.

Kouraev, A. V., E. A. Zakharova, O. Samain, N. M. Mognard, and A. Cazenave (2004), Ob' river discharge from TOPEX/Poseidon satellite altimetry (1992-2002), *Remote Sens. Environ.*, *93*(1-2), 238–245, doi:10.1016/j.rse.2004.07.007.

Long, C. M., and T. M. Pavelsky (2013), Remote sensing of suspended sediment concentration and hydrologic connectivity in a complex wetland environment, *Remote Sens. Environ.*, *129*, 197–209, doi:10.1016/j.rse.2012.10.019.

Maillard, P., N. Bercher, and S. Calmant (2015), New processing approaches on the retrieval of water levels in Envisat and SARAL radar altimetry over rivers: A case study of the São Francisco River, Brazil, *Remote Sens. Environ.*, *156*, 226–241, doi:10.1016/j.rse.2014.09.027.

Manning, R., Griffith, J. P., Pigot, T. F., & Vernon-Harcourt, L. F. (1890). On the flow of water in open channels and pipes. *Transactions of the Institution of Civil Engineers of Ireland*.

McFeeters, S. K. (1996), The use of the Normalized Difference Water Index (NDWI) in the delineation of open water features, *Int. J. Remote Sens.*, *17*(7), 1425–1432, doi:10.1080/01431169608948714.

Moller, D., E. Rodríguez, J. Carswell, and D. Esteban-Fernadez (2011), A calibration/validation platform for the SWOT mission, in *Proc. International Geoscience and Remote Sensing Symposium*, Vancouver, Canada.

Neeck, S. P., E. J. Lindstrom, P. V. Vaze, and L.-L. Fu (2012), Surface Water and Ocean Topography (SWOT) mission, *Proc. SPIE 8533, Sensors, Syst. Next-Generation Satell. XVI*, *8533G*, doi:10.1117/12.981151.

O'Loughlin, F., M. A. Trigg, G. J. P. Schumann, and P. D. Bates (2013), Hydraulic characterization of the middle reach of the Congo River, *Water Resour. Res.*, *49*(8), 5059–5070, doi:10.1002/wrcr.20398.

O'Loughlin, F. E., J. Neal, D. Yamazaki, and P. D. Bates (2016), ICESat-derived inland water

surface spot heights, *Water Resour. Res.*, 1–20, doi:10.1002/2014WR015716.

Papa, F., F. Durand, W. B. Rossow, A. Rahman, and S. K. Bala (2010), Satellite altimeter-derived monthly discharge of the Ganga-Brahmaputra River and its seasonal to interannual variations from 1993 to 2008, *J. Geophys. Res. Ocean.*, *115*(12), 1–19, doi:10.1029/2009JC006075.

Paris, A., R. C. D. Paiva, J. S. Silva, D. M. Moreira, S. Calmant, P.-A. Garambois, W. Collischonn, M. P. Bonnet, and F. Seyler (2016), Stage-discharge rating curves based on satellite altimetry and modeled discharge in the Amazon basin, *Water Resour. Res.*, 1–20, doi:10.1002/2014WR015716.

Pavelsky, T. M., and L. C. Smith (2009), Remote sensing of suspended sediment concentration, flow velocity, and lake recharge in the Peace-Athabasca Delta, Canada, *Water Resour. Res.*, *45*(11), n/a–n/a, doi:10.1029/2008WR007424.

Pavelsky, T. M., M. T. Durand, K. M. Andreadis, R. E. Beighley, R. C. D. Paiva, G. H. Allen, and Z. F. Miller (2014), Assessing the potential global extent of SWOT river discharge observations, *J. Hydrol.*, *519*, 1516–1525, doi:10.1016/j.jhydrol.2014.08.044.

Puckridge, J. T., F. Sheldon, K. F. Walker, and A. J. Boulton (1998), Flow variability and the ecology of large rivers, *Mar. Freshw. Res.*, *49*, 55–72, doi:10.1071/MF94161.

Rodriguez, E. (2016), *Surface Water and Ocean Topography Mission (SWOT) Project - Science Requirements Documents*.

Rodriguez, E., and J. M. Martin (1992), Theory and design of interferometric synthetic aperture radars, *IEE Proc. F Radar Signal Process.*, *139*(2), 147, doi:10.1049/ip-f-2.1992.0018.

Rosen, P. A., S. Hensley, I. R. Joughin, F. K. Li, S. N. Madsen, E. Rodriguez, and R. M. Goldstein (2000), Synthetic aperture radar interferometry Synthetic aperture radar interferometry, *Proc. IEEE*, *88*(3), 333–382, doi:10.1088/0266-5611/14/4/001.

Schumm, S. A. (2007), *River variability and complexity*, Cambridge University Press.

Smith, L. C. (1997), SATELLITE REMOTE SENSING OF RIVER INUNDATION AREA , STAGE , AND DISCHARGE : A REVIEW, *Hydrol. Process.*, *11*(April 1996), 1427–1439.

Tejedor, A., A. Longjas, D. A. Edmonds, I. Zaliapin, T. T. Georgiou, A. Rinaldo, and E. Foufoula-Georgiou (2017), Entropy and optimality in river deltas, *Proc. Natl. Acad. Sci.*, *114*(44), 201708404, doi:10.1073/pnas.1708404114.

Tourian, M. J., A. Tarpanelli, O. Elmi, T. Qin, L. Brocca, T. Moramarco, and N. Sneeuw (2016), Spatiotemporal densification of river water level time series by multimission satellite altimetry, *Water Resour. Res.*, *52*(2), 1140–1159, doi:10.1002/2015WR017654.

Wollheim, W. M., G. K. Mulukutla, C. Cook, and R. O. Carey (2017), Aquatic Nitrate Retention at River Network Scales Across Flow Conditions Determined Using Nested In Situ Sensors, *Water Resour. Res.*, *53*(11), 9740–9756, doi:10.1002/2017WR020644.